National Library
of Canada

Acquisitions and
Bibliographic Services Branch

395 Wellington Street
Ottawa, Ontario
K1A 0N4

Bibliothèque nationale
du Canada

Direction des acquisitions et
des services bibliographiques

395, rue Wellington
Ottawa (Ontario)
K1A 0N4

NOTICE

The quality of this microform is heavily dependent upon the quality of the original thesis submitted for microfilming. Every effort has been made to ensure the highest quality of reproduction possible.

If pages are missing, contact the university which granted the degree.

Some pages may have indistinct print especially if the original pages were typed with a poor typewriter ribbon or if the university sent us an inferior photocopy.

Reproduction in full or in part of this microform is governed by the Canadian Copyright Act, R.S.C. 1970, c. C-30, and subsequent amendments.

AVIS

La qualité de cette microforme dépend grandement de la qualité de la thèse soumise au microfilmage. Nous avons tout fait pour assurer une qualité supérieure de reproduction.

S'il manque des pages, veuillez communiquer avec l'université qui a conféré le grade.

La qualité d'impression de certaines pages peut laisser à désirer, surtout si les pages originales ont été dactylographiées à l'aide d'un ruban usé ou si l'université nous a fait parvenir une photocopie de qualité inférieure.

La reproduction, même partielle, de cette microforme est soumise à la Loi canadienne sur le droit d'auteur, SRC 1970, c. C-30, et ses amendements subséquents.

Canada

Manganese-Bismuth Prepared by Rapid Solidification

by

Xiaoming Guo

Department of Physics, McGill University

Montréal, Québec

Canada

August, 1992

A Thesis submitted to the

Faculty of Graduate Studies and Research

in partial fulfillment of the requirements for the degree of

Doctor of Philosophy

National Library of Canada
Acquisitions and Bibliographic Services Branch
395 Wellington Street
Ottawa, Ontario
K1A 0N4

Bibliothèque nationale du Canada
Direction des acquisitions et des services bibliographiques
395, rue Wellington
Ottawa (Ontario)
K1A 0N4

Your file   Votre référence

Our file   Notre référence

ISBN 0-315-87738-3

Canada

Abstract

The low temperature phase (LTP) of MnBi, an interesting material with large magnetic anisotropy, has been obtained for the first time in bulk quantities in almost single-phase form ($> 95^{wt}\%$) by melt-spinning, followed by annealing.

X-ray, electron microscope and differential scanning calorimetry (DSC) studies indicate that the melt-spun MnBi is amorphous, and may be phase separated. A mechanism is suggested for the glass formation in MnBi. Upon heating, amorphous MnBi first crystallizes around 440 K, then forms LTP around 540 K. DSC and thermomagnetometry studies show that the LTP transforms to high temperature phase around 630 K through two separate processes: a composition transition and a magneto-structural transition.

The anisotropy field, H_a of LTP, is measured from 147 to 586 K by a pulsed magnet combined with the singular point detection technique (SPD). H_a increases with temperature, and reaches a maximum value of 9 T at 530 K. The critical field for spin reversal of a ferrimagnetic phase of MnBi is also detected by SPD from 80 to 200 K, reaching a maximum value of 8 T at 120 K. The coercivity of LTP is successfully described by a model of domain wall pinning which predicts, at 300 K, a domain wall energy of 15.7 erg/cm^2 and a wall thickness of 70 Å.

Résumé

La phase basse température de BiMn, un matériel possédant une forte anisotropie magnétique, a été élaborée pour la première fois en grande quantité sous forme presque entièrement mono-phase ($> 95^{wt}\%$) par trempe ultra rapide, suivie d'un recuit.

Des études par diffraction des rayons-X, par microscopie électronique et par calorimétrie différentielle à balayage (CDB) indiquent que le BiMn ainsi fabriqué est amorphe et peut se séparer en plus d'une phase. Un mécanisme est suggéré pour expliquer la formation du réseau amorphe dans BiMn. En augmentant la température, le BiMn amorphe se cristallizent à environ 440 K, puis forme la phase basse température autour de 540 K. Des études calorimétriques (CDB) et thermomagnétiques montrent que la phase basse température se transforme en phase haute température aux environs de 630 K en passant par deux processus distincts: un changement de composition et une transition magnéto-structurale.

Le champ d'anisotropie, H_a de la phase basse température, est mesuré de 147 K à 586 K à l'aide d'un électro-aimant pulsé, combiné avec une technique de détection par point singulier (DPS). H_a augmente avec la température et atteint un maximum de 9 T à 530 K. Le champ critique nécessaire au renversement du spin de la phase ferrimagnétique de BiMn est également déterminé par DPS entre 80 et 200 K, et atteint une valeur maximale de 8 T à 120 K.

La coercivité de la phase basse température est décrite avec succès par un modèle de fixation des murs entre domaines qui prédit, à 300 K , une énergie du mur entre les domaines de 15.7 erg/cm^2 et une épaisseur du mur de 70 Å.

摘要

MnBi 低温相 (LTP) 以其磁晶各向异性高而引人注目。此研究成功地用旋淬凝固法配以退火处理，首次得到了大量的单相 (> 95 wt%) MnBi。X-光、电镜及差分扫描热量计 (DSC) 的研究表明，旋淬所得到的带状 MnBi 处于非晶态，并有相分离的迹象。本文提出了解释 MnBi形成非晶态的一种机制。非晶态 MnBi 在温度 440 K 附近晶化，然后在 540 K 左右形成 LTP. DSC 和热磁计的研究发现，LTP 经由成份转变和结构-磁性转变两个可分离的过程，在 630 K 附近相变到高温相。此研究还用脉冲磁场结合奇点测量法 (SPD)，测量了从 147 K 到 586 K 范围内 LTP 的磁晶各向异性场。此各向异性场随温度升高而增强，到 530 K 达到极大值 9 T。从 80 到 200 K，MnBi 的一个亚铁磁相的自旋反转场也被测到，其及大值在 120 K 为 8 T。一个混合的畴壁钉扎模型成功地解释了 LTP 的矫顽力，并给出 了 LTP 在 300 K 的畴壁能为 15.7 尔格每平方厘米，及畴壁厚度 70 埃。

Acknowledgments

I am grateful to my thesis supervisors and many individuals and organizations who have helped me to prepare this thesis.

John O. Ström-Olsen, one of my supervisors, has given me the feasible suggestions and constructive criticisms that shaped the present research. I enjoy his patience that allowed my interest to have a free space in the research work, as well his hard push that stimulated my intellectual power. Discussions with Zaven Altounian, my other supervisor, produced most of the experimental ideas used in the research. I appreciate my supervisors for their helping me in my English and in my using the facilities and resources in the physics department at McGill university.

Mark Sutton gave me a lot of good advise in building the high temperature x-ray furnace, helped me in computer programming and in using his software. I got also help from discussions with Dominic Ryan on instrumental electronics.

Guoha Tu taught me most of the experiment methods in the laboratory and introduced me to the subject of MnBi. I benefited a lot from discussions with Xinhe Chen, and from his collaboration in the improvement of the pulsed magnet. Alicja Zaluska carried out the electron microscopy that was used in this thesis.

Loki Jorgenson and Martin Lacasse helped me in using the computers effectively. Eric Dufresne and Louis Taillefer translated the abstract to French. Diane Koziol and Paula Domingues helped me in going through the administrative details. Frank van Gils, John Egyed, and Michel Champagne gave me the technical support on building and repairing instruments.

By sharing the same laboratory, office, and computer system, I got help and pleasure from the discussions and collaborations with Lexiang Liao, Yan Xu, Ming Mao,

Yushan Shi, Xiaoping Bian, Steve Brauer, Andrew Dawson, Abdelhadi Sahnoune, Ralf Bruning, Yi Zhao, Zhida Yan, Tao Sun, and those who helped me and escaped from my careless memory.

Without the financial support from the government of Guangdong Province, I had not been able to travel to North America for the study. The research was supported by grants from the Natural Sciences and Engineering Research Council of Canada, Fonds pour la Formation de Chercheurs et l'aide à la Recherche, Quebec, Dow Hickson Scholarship, and the Faculty of Gradute Studies and Research of McGill University.

To My Parents

Contents

List of Figures

List of Tables

Chapter 1

Introduction

This thesis is a study of the equiatomic compound of manganese bismuth, MnBi, prepared by rapid solidification. The work comprises two parts. The first part is the formation of bulk single phase MnBi, which involves the preparation of amorphous MnBi, followed by its phase transformations upon heating. The second part is the measurement and analysis of its magnetic properties.

MnBi is an interesting material. It is ferromagnetic and exhibits a first order structural phase transformation between temperatures of 613 and 628 K. The equilibrium phase below the transition is called the low temperature phase (LTP) and that above the high temperature phase (HTP).

Since Guillaud discovered in 1943 that the LTP was magnetic (Guillaud, 1943), MnBi has been an active subject of research. The LTP has an extraordinarily high crystalline anisotropy; that is, the material has a large difference in energy when the direction of the magnetization changes with respect to the crystal axes. This is an essential property for a material to become a permanent magnet. The anisotropy was also found (Guillaud, 1951a) to increase with temperature, in contrast to most other magnetic materials. Adams (1953) prepared a hard magnet from MnBi which gave an energy product of 42 kJ/m^3. The energy product is a measure of how much magnetic energy can be stored in a unit volume of the material (See Chapter6). Adams concluded that these magnets exhibited a coercive force exceeded by no other known practical magnets, and that they could be used for practically all applications utilizing permanent magnets at that time and particularly where a high resistance to demagnetization is important. Even comparing with recently developed Nd-Fe-B magnets, MnBi has a much higher magnetic anisotropy at high temperatures. For this reason, MnBi has a promising potential as a permanent magnet material at high temperatures.

Observing the magnetic domain pattern, Roberts and Bean (1954) found that MnBi has a large magneto-optic effect, which makes MnBi a potential storage material in the magneto-optic recording technique. The magneto-optic recording technique combines the wearlessness and high density ($> 10^8 bits/cm^2$) of optical recording with the rewritability of magnetic recording. Williams and his colleagues (1957) studied the optical read-out of magnetically stored information on MnBi thin films, using the Faraday effect (the change in the polarization direction of linearly polarized light upon transmission through a magnetized substance). In 1964, Chen and Gondo examined the temperature dependence of the Kerr effect (the change in the polarization direction of linearly polarized light upon reflection from the surface of a magnetized substance), and found that the LTP of MnBi has a Kerr rotation of 0.9 degree at room temperature. In 1968, Chen, Ready and Bernal theoretically analyzed and experimentally tested the thermomagnetic writing and magneto-optical reading on MnBi thin film. They concluded that MnBi was particularly suitable for optical mass memory applications.

However, a few problems have prevented MnBi from finding immediate application. For the memory application, the main drawback is that the LTP transforms to the HTP before it reaches its Curie point, and the resultant phase after thermomagnetic writing is the so called quenched high temperature phase (QHTP), which has a Curie point of 450 K. The lower Curie point is better for storage application, but the drawback of QHTP is its instability: it transforms back to LTP above the Curie point. A further problem is that the MnBi thin films are susceptible to moisture and oxygen contamination (Chen, 1971).

For application as a permanent magnet, there are also problems. The yield of producing MnBi single phase is extremely low by conventional metallurgical techniques, and MnBi deteriorates under a normal atmosphere. Both of these make the processing of MnBi costly.

It is therefore of great interest to understand and to enhance the formation of MnBi, to study the LTP-HTP transformation and the mechanism of magnetic hardening.

The present work began from preparing MnBi by rapid solidification. The melt-spinning technique was used, which allows the quenching of the alloy from the melt to room temperature at a rate about 10^6 Ks^{-1}. This technique has been widely used to produce amorphous or glassy metals. The initial motivation, for using rapid quenching, was to produce fine grains of MnBi in order to increase the coercivity by reducing the grain size to single magnetic domain. After careful study, however, it was found that the as-spun MnBi was amorphous, and this triggered the research that comprises this thesis.

Most metallic alloys form glasses easily around a deep eutectic composition in the phase diagram (Takayama, 1976). However, the phase diagram of MnBi does not show any deep eutectic. Therefore, the first question is why MnBi can form a glass. This question will be discussed in Chapter 4.

A second interesting point is the discovery that upon heating the amorphous MnBi to 570 K an almost single phase LTP of MnBi is formed. This solved the long standing problem of how to produce single phase MnBi in bulk. The question here is why a method widely used to prepare metastable phases can result in producing a high yield of a stable phase. This question will be analyzed in Chapter 5. Also, the LTP-HTP transformation was examined by a variety of experiments and deeper understanding of the transition was obtained.

Once the basic process of preparing MnBi is established, additions of other elements to the Mn-Bi system were tried to enhance its properties, specifically (a) increasing the resistance to deterioration, (b) increasing the coercivity, and (c) forming a phase that is stable and has a low Curie point, as required for magneto-optic storage applications.

In Part 2, the magnetic properties of LTP are analysed. The technique of a pulsed magnetic field has been successfully combined with the so called Singular Point Detection technique that enables the direct measurement of the anisotropy field at different temperatures. This direct measurement of the anisotropy field of MnBi is made for the first time, and the temperature dependence of coercivity is found to be well described by a hybrid domain wall model.

Part I

The formation of bulk single phase MnBi

Chapter 2

The Mn-Bi system

2.1 Formation of MnBi and the Mn-Bi phase diagram

Mn and Bi are difficult to alloy because of the large difference in their melting points. The Mn-Bi equilibrium phase diagram, Fig. 2.1, shows that the melting point difference is about 1000 K. Within the 1000 K for MnBi composition, there is about a 700 K span of temperature (the region between the liquidus and the peritectic melting temperature at 719 K), where Mn is segregated from the liquid. The segregated Mn undergoes a series of polymorphous transformations from δ-Mn to γ-Mn, to β-Mn, and finally to α-Mn at 1416, 1352, and 983 K respectively. Two other unknown phase transformations at 1316 and 870 K had also been detected from cooling curves (Siebe, 1919). The five transformations fill in the region with a sequence of horizontal lines. Only cooling below this coexistence region of Mn_{solid} and liquid, can the MnBi high temperature phase (HTP) be formed, at 719 K, by the peritectic reaction:

$$Liquid + Mn_{solid} \rightarrow MnBi(HTP)_{solid}$$

The HTP transforms, upon further cooling, to MnBi low temperature phase (LTP) at 613 K. However, the peritectic reaction is difficult to complete. Having a lower density, the segregated Mn floats, above 719 K, to the top of the liquid if the cooling

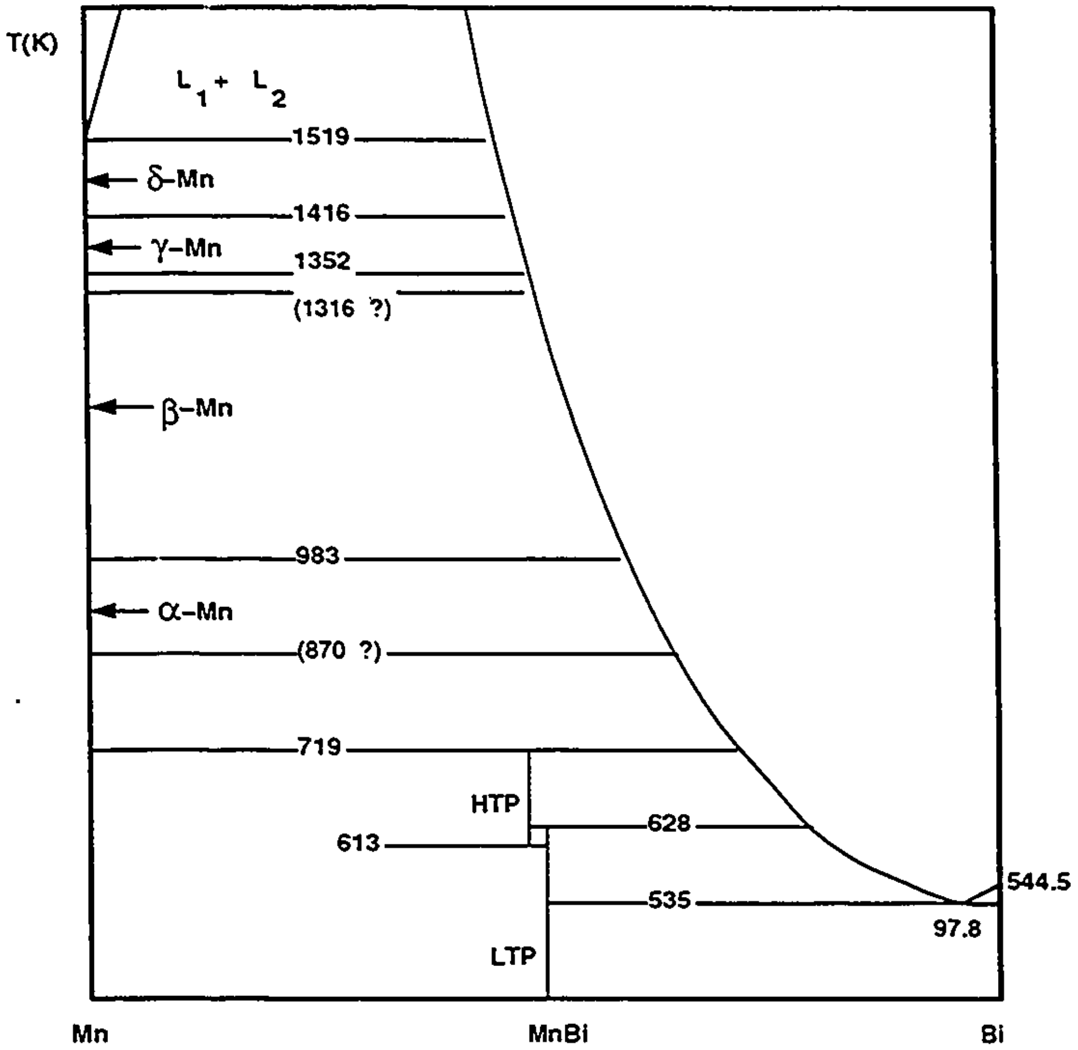

Figure 2.1: Mn-Bi phase diagram.(Hansen, 1958; Chen, 1974)

rate is slow, so that Mn will already be inhomogeneously distributed when the liquid is cooled to 719 K. This will cause some diffusion problems for the peritectic reaction. In addition, the diffusion of the Mn and Bi through MnBi is found to be extremely slow (Andresen *et al.*, 1967; Roberts, 1956; Seybolt *et al.*, 1956), so that the formation of MnBi at the interface actually impedes any further reaction. As a result, pure Mn and Bi remain after the system is solidified.

In order to get rid of the unreacted Mn and Bi from magnetic LTP, it is a usual practice to break up the resultant mass into fine powder in a ball mill and then to separate the magnetic particles by a magnetic separator. Nevertheless, many methods have been employed to avoid the segregation problem by synthesising MnBi below 719 K. T. Chen and Stutius (1974) pulled single crystals of LTP and quenched high temperature phase (QHTP) from a molten solution of the binary alloy maintained about 628 K and 700 K respectively by adding excess Bi. LTP and a high coercivity phase (HC) MnBi were made from Mn-Bi eutectic melt just above 535 K by Noothoven (1968) using the Czochralski technique and by Pirich (1980) using Bridgman-Stockbarger method. The result was 3.2 volume percent (Pirich, 1980) of MnBi embedded in bismuth single crystals. Andresen (1967) made LTP by sintering Mn and Bi powders at 708 K for 20–30 days. Chen, Ready and Bernal (1968) prepared MnBi thin films on mica substrate by vacuum depositing first a layer of Bi then a layer of Mn, and annealed to get epitaxial growth.

Another completely different approach to avoiding Mn segregation from Mn-Bi liquid is rapid solidification. The idea is to cool the melt through the temperature region 1370 to 719 K in the shortest possible time to prevent large segregation. Xu, Lakshmi and Smith (1989) used melt spinning, although they succeeded only in producing a sample with a small fraction of LTP.

2.2 Crystalline structures of MnBi phases

As a non-equilibrium processing method, melt-spinning, combined with different heat treatments, produces other metastable phases of Mn-Bi as well as LTP and HTP. Table 2.1 gives their structure and some magnetic properties. The only phase found in the composition range covered by the miscibility gap in the liquid state (see Fig. 2.1) is Mn_3Bi. This compound is metastable. All other phases, stable or metastable, have similar structures but different magnetic properties. LTP has the NiAs structure. As shown in Fig. 2.2, the structure is hexagonal with Mn atoms forming a simple hexagonal sublattice and Bi atoms forming a close packed hexagonal sublattice. There are two large interstitial sites in one cell. When LTP transforms to HTP at 628 K, some Mn atoms jump to the interstitial sites so that the HTP has the composition of $Mn_{1.08}Bi$ (Chen and Stutius, 1974; Andresen, Engebretsen and Refsnes, 1972). Quenching the HTP to room temperature, one obtains, (a) QHTP whose structure is distorted by the interstitials (Andresen, Engebretsen and Refsnes, 1972); and (b) a new phase (NP) (Guillaud, 1951b) that has the same crystal structure as LTP but with slightly different lattice parameters. A high coercivity phase (HC) of MnBi was also reported in the form of precipited needles in Bi single crystal. HC has a structure very close to NP, but HC is ferrimagnetic while NP is non-magnetic. Both HC and NP are metastable.

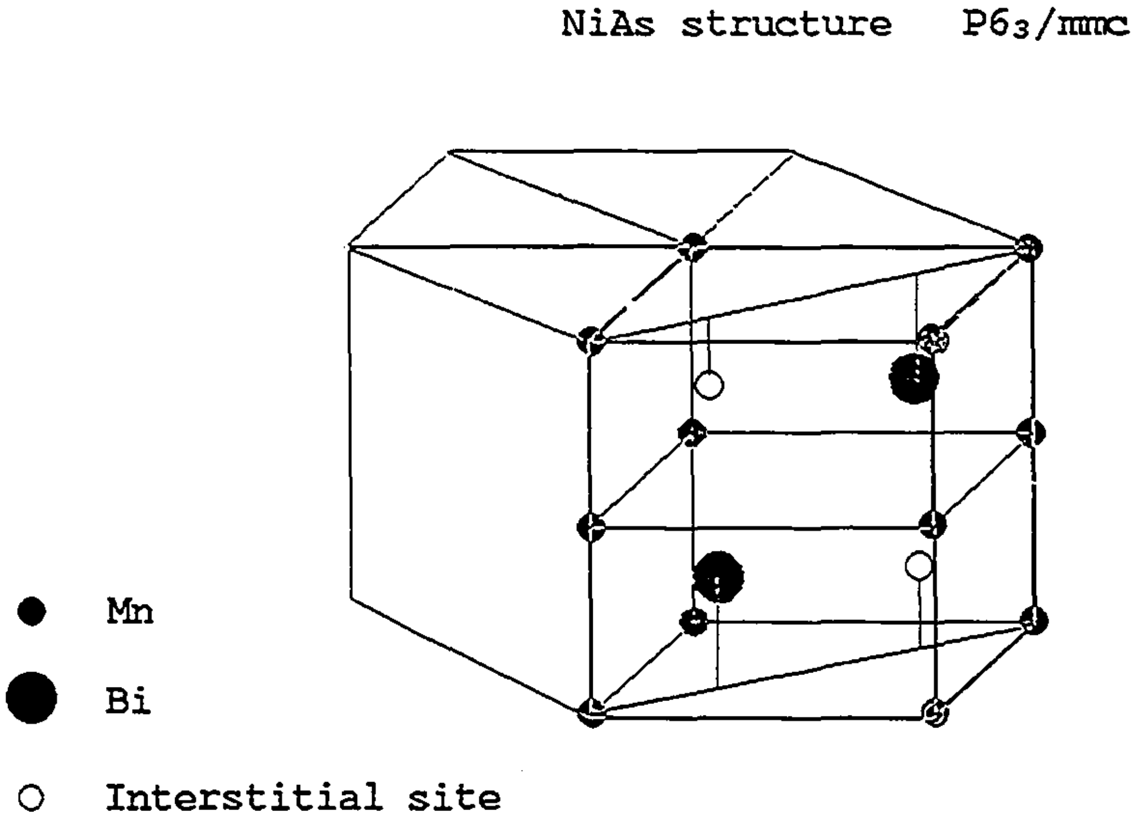

Figure 2.2: Diagram of MnBi structure of different phases: LTP has the interstitial sites empty, HC, NP, HTP and QHTP may have different populations of interstitial Mn. The hexagonal symmetry is distorted for QHTP.

		Cell parameters(nm)				K_a	References
Phase	structure	a	b	c	$T_c(K)$	$(10^5 J/m^3)$	
MnBi (LTP)	Hex. $P6_3/mmc$	0.429		0.6126	628^a ferromag.	22 at 490 K	(Roberts, 1956) (Andresen *et al.*, 1967)
MnBi (HTP)	Hex. $P6_3/mmc$	0.438		0.600	paramag.		(Chen and Stutius, 1974)
MnBi (QHTP)	Orth. $P222_1$	0.4344	0.7505	0.5959	440 ferromag.	42.5 at 4 K	(Andresen, Engebretsen and Refsnes, 1972)
	or deformed $P6_3/mmc$	0.434		0.597			(Yoshida, Yamada and Furukawa, 1968)
MnBi (HC) (NP)	Hex. $P6_3/mmc$	0.432		0.583	240 ferrimag. paramag.	12 at 77 K	(Guillaud, 1951b)(Noothoven Van Goor and Zijlstra, 1968)
Mn_3Bi	Rhom. $R\bar{3}m$ (Hex. index)	0.449		1.997			(Yoshida, Yamada and Furukawa, 1968)
Bi_2Mn	Tetr.	0.5845		0.5361			(Furst and Halla, 1938)
Bi_3Mn_2	Orth.	0.4317	0.5255	0.6321			(Andresen, Engebretsen and Refsnes, 1972)

^{a} Transformation temperature to HTP.

Table 2.1: The crystalline phases of Mn-Bi system

Chapter 3

Experimental techniques

Four types of experimental methods are used in this thesis: metallurgical methods to prepare the samples, x-ray diffraction and electron microscopy to characterize their structures, thermal analysis to characterize their phase transformations, and magnetic measurements to characterize magnetic properties. For most of the methods, only a brief description will be given to explain the principles of the techniques and the significance of the data they produced. More detailed discussions are given on the high temperature x-ray furnace built by the author. The pulse magnet, which the author improved to measure hysteresis loops and anisotropy fields, will be discussed in Part 2 of the thesis.

3.1 Sample preparation

In the last three decades, many techniques have been developed to form amorphous alloys (Takayama, 1976). The most widely used is rapid quenching at cooling rates of 10^6 K/sec. This cooling rate is sufficient to suppress the nucleation and growth of crystals during the solidification for a wide range of metallic alloys. One of the rapid quenching methods, melt-spinning, is used to prepare MnBi alloys in the present work.

There are two steps in preparing samples. The first step is to make an ingot of

MnBi, and the second step is remelting followed by rapid solidification.

The ingots of MnBi alloy are prepared by induction melting: A water cooled copper tube about 1 cm in diameter is horizontally placed in a quartz tube of 2.54 cm in diameter, filled with titanium gettered argon atmosphere at a pressure of 33 kPa. On the surface of the copper tube, there are some dimples to hold appropriate amounts of Bi of 99.999% purity and Mn of 99.99% purity. Outside the quartz tube, a radio frequency current passing through a water cooled coil, melts the samples by induction. The induction melting ensures minimal loss of either component during alloying and produces homogeneous ingots. The rapid solidification is carried out by melt spinning. Fig. 3.1 is a schematic diagram of the apparatus used. About 1 gram of MnBi is put in a vertical quartz tube about 1 cm in diameter. The bottom of the tube has a nozzle of diameter 0.25 mm, and the top is connected through an electric-magnetic valve to argon gas of pressure about 160 kPa. Below the tube is a rotating copper wheel 2 cm thick and 10 cm in diameter. The rotation axis is horizontally placed so the curved surface of the wheel, with tangential speed of S = 50 ± 5m/s, is 3 mm beneath the nozzle of the tube. After the ingot is melted by an induction coil of radio frequency outside the tube, the high argon pressure is applied so that the melt is ejected on the cooling wheel. The liquid alloy sticks to the wheel and solidifies. Cooling to low temperature, the solidified ribbons shrink and peel off the wheel, and are thrown into the collection tube. A suitable speed of the wheel and nozzle diameter of the tube are important parameters to ensure a high quench rate, which is achieved by the thinnest layer of the melt ejected that can sustain a good thermal contact with the wheel.

The following is a rough estimate of the cooling rate. From the geometrical position of the collection tube, it is estimated that the molten alloy travels $d = 3\ cm$ before separating from the wheel. The separation from the wheel suggests that the alloy ribbons are cooled enough to shrink and peel off. The temperature is then assumed to be close to room temperature. So the cooling time of the sample is

$$t = d/S = 6 \times 10^{-4}\ \ sec.$$

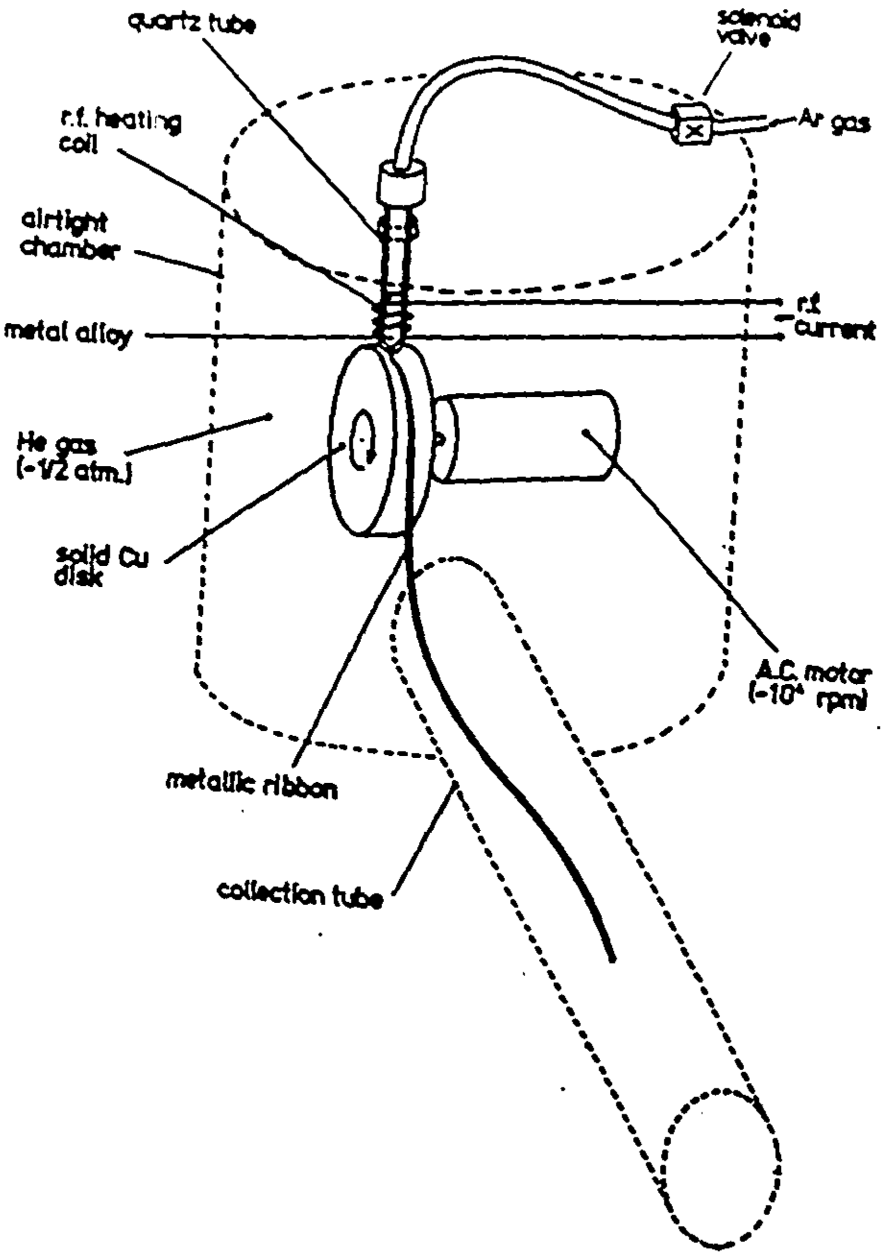

Figure 3.1: A schematic diagram of the melt-spinning apparatus. Diagram from (From, 1989).

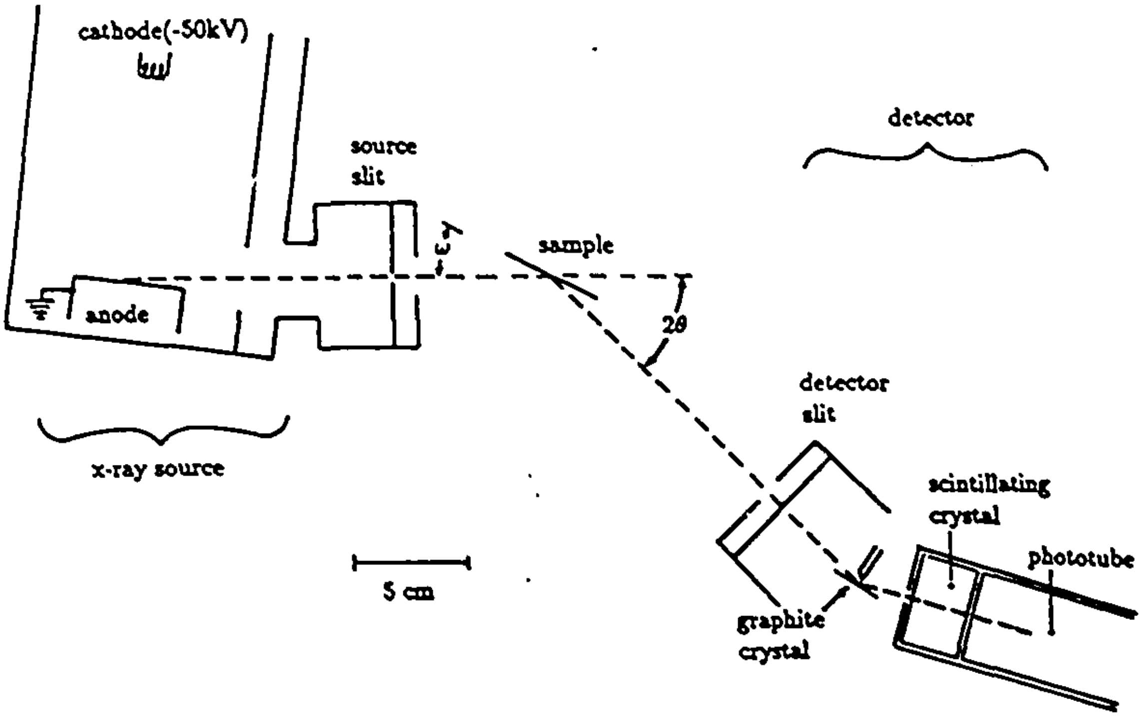

Figure 3.2: A schematic diagram of the x-ray diffractometer. Diagram from (From, 1989).

Suppose the initial temperature of MnBi liquid is 1370 K, the temperature of the liquidus, and if the final temperature is 400 K, so the temperature difference ΔT is $\sim 1000K$. The cooling rate is therefore $\Delta T/t \sim 1.6 \times 10^6$ K/sec.

3.2 X-ray diffraction

The microstructure of different MnBi phases are mainly determined by x-ray powder diffraction experiments (Guinier, 1963; Warren, 1969). A schematic diagram of the apparatus (model STADI 2/PL, Nicolet XRD Co. Fremont, California, U.S.A.) is shown in Fig. 3.2. The setup is as follows: An incident beam of Ni filtered Cu- K_α

x-rays (0.15418 nm) fall on the powdered sample that is mounted on a glass plate, and a detector scans the diffraction angles θ to record the intensity $I(\theta)$ of the x-rays scattered by the sample.

$I(\theta)$ contains the information about the structure of the sample. Having a wavelength λ comparable to the interatomic spacing, the x-rays scattered by different atoms of the sample interfere with each other to form an angular dependent distribution of the intensity, $I(\theta)$. θ relates to the momentum change q of a photon by

$$q = 4\pi sin\theta/\lambda \ . \tag{3.1}$$

Thus the atomic distribution in real space is mapped onto an intensity distribution of the scattered x-rays in q-space (momentum or reciprocal space). Fig. 3.3 illustrates how x-ray diffraction distinguishes structures of different states of matter: $I(\theta)$ from a gas of disordered atoms gives a flat background, that from a crystal of long range ordered atoms gives discrete sharp peaks, that from a liquid or an amorphous solid of short range ordered atoms gives broad peaks. For a known crystalline structure, the peak positions θ are determined by Bragg law, the condition for constructive interference,

$$\lambda = 2d_{hkl} sin\theta, \tag{3.2}$$

where λ is the wavelength of x-ray and d_{hkl} is the spacing of a group of parallel atomic planes indexed by three indices h, k and l. The angular width at half intensity $\Delta(2\theta)$ of a peak is related to the size L of the crystal by the Scherrer formula

$$\Delta(2\theta) = \frac{\lambda}{Lcos\theta_0} , \tag{3.3}$$

where θ_0 is the position of the peak. Eqns. 3.2 and 3.3 reflect two reciprocal relations between the real space and q-space: a larger q of a peak position corresponds to a smaller atomic spacing, and a broader size of a peak width corresponds to order on a shorter range.

Different crystalline materials have different positions and intensities for the $I(\theta)$ peaks. This serves as a signature to identify the phases of a material. The relative

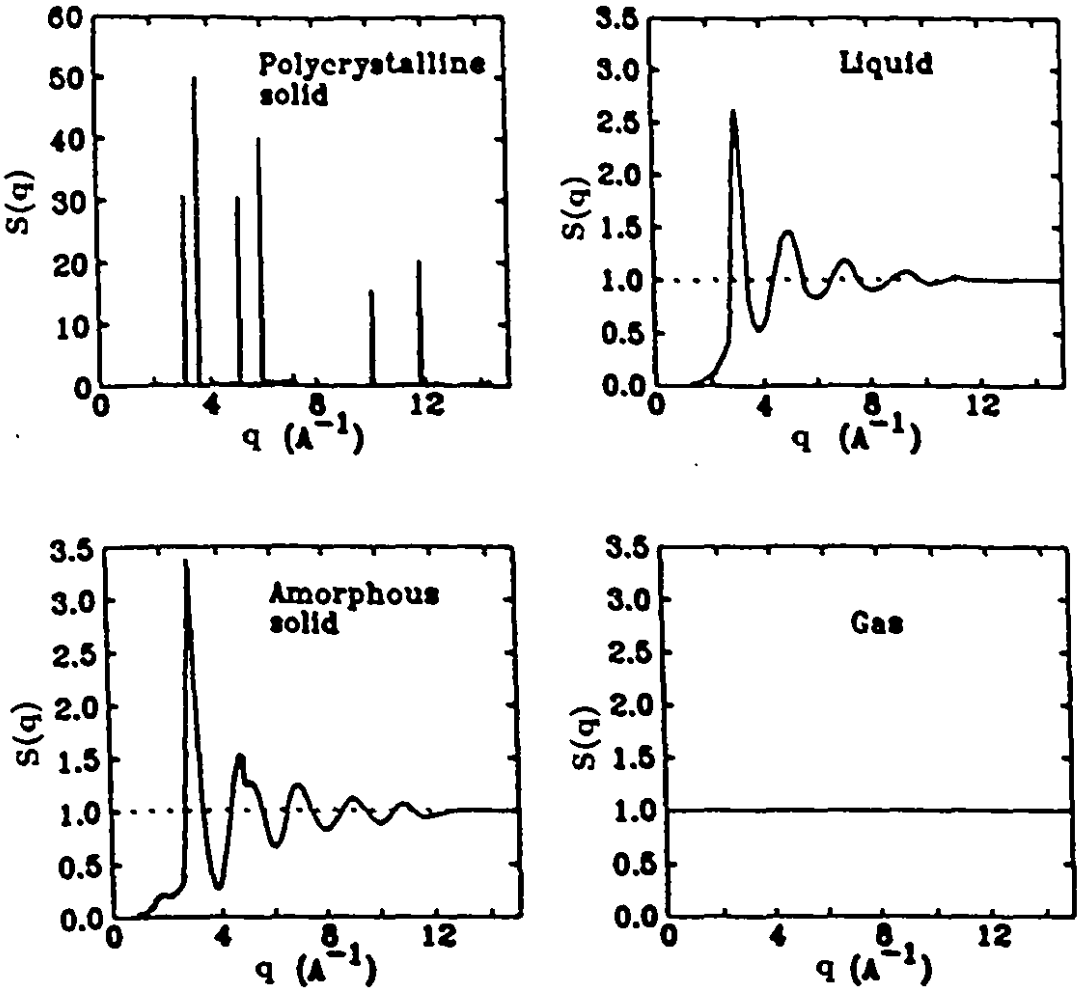

Figure 3.3: The diffraction patterns of four states of matter. The coherently scattered x-ray intensity I is proportional to $f^2(q)S(q)$, where f is atomic scattering factor. Diagram from (From, 1989).

	2θ		relative intensity	
hkl	Theory	Experiment	Theory	Experiment
102	27.186	27.2	100	100
014	37.985	38.0	37	31
110	39.651	39.6	18	32
105,006	44.590,45.899	45.1	7	9
113	46.058	46.0	1	10
002	48.740	48.7	20	23

Table 3.1: X-ray diffraction data of Bi. Theoretical calculation compared with experimental data from 3.4.

intensity of a peak can be calculated by

$$I_{hkl} = \frac{1 + cos^2 2\theta}{sin\theta sin 2\theta} n F_{hkl}^2 D, \tag{3.4}$$

where:

n is the multiplicity factor which comes from the statistics of the symmetry of lattice planes;

$D = exp(-\frac{16\pi^2 sin^2\theta}{\lambda^2}\frac{\Delta X^2}{3})$ is the Debye-Waller temperature factor, and ΔX is the average displacement of atoms around their lattice points;

$F_{hkl} = \sum f_i exp[-2\pi i(hx_i + ky_i + lz_i)]$ is the structure factor. The structure factor is a sum over atoms at position (x_i, y_i, z_i) in the unit cell, and f_i are atomic scattering factor. The f_i is proportional to the number of electrons in the ith atom, and its angular dependence, $f_i(q)$, is determined by the electron distribution inside the atom.

Table 3.1 compares the diffraction data of Bi from experiment and that calculated from Eqn. 3.4. Fig. 3.4 shows the diffraction pattern of Bi using Cu-K_α x-ray of wavelength $\lambda = 0.15418nm$. The results from Eqn. 3.4 are satisfactory to identify a possible phase of known structure.

For a phase such as Mn_3Bi whose powder diffraction data is not available , intensity calculations are essential for the characterization of the phase.

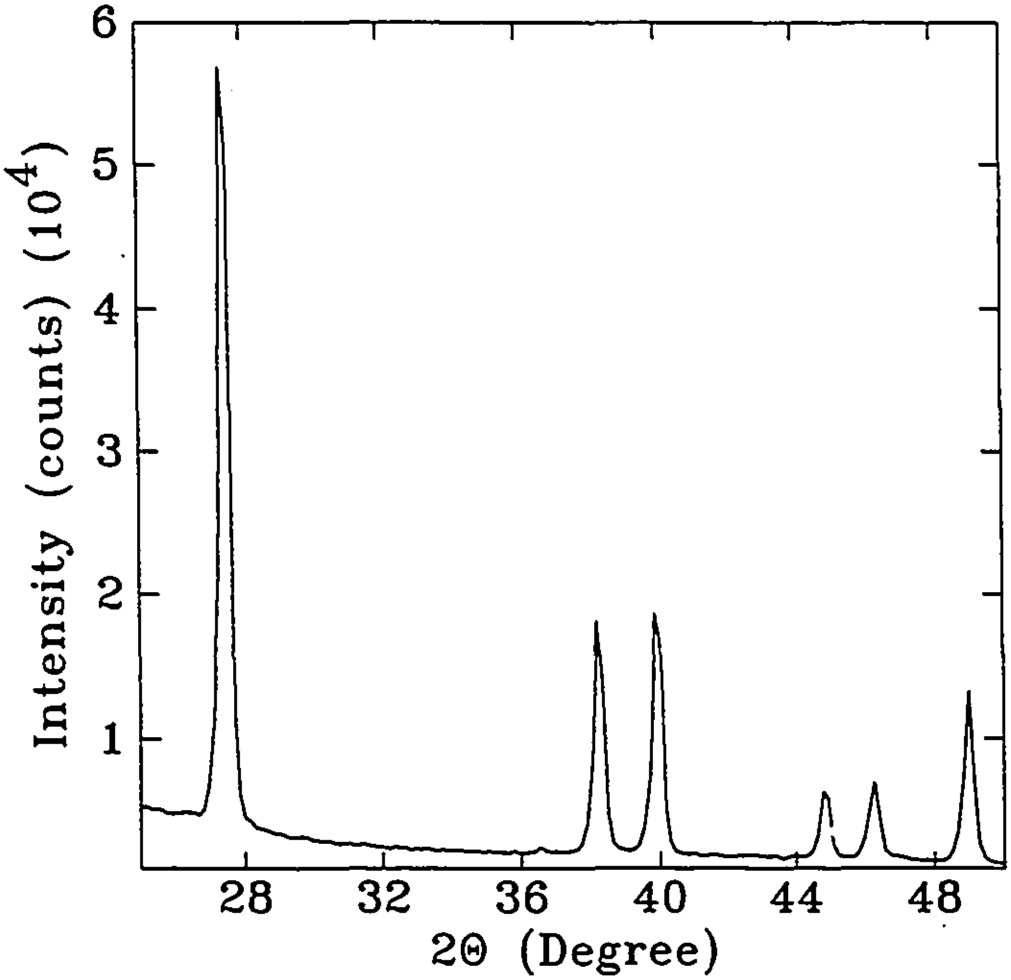

Figure 3.4: The x-ray diffraction pattern of Bi

3.3 High temperature x-ray furnace

High temperature x-ray diffraction is important in research that involves high temperature phases and phase transformations. Not all high temperature phases can be successfully quenched to room temperature with the structures unchanged. It is necessary, therefore, to characterize a structure at a temperature where it is in equilibrium. Furthermore, a direct way to identify phase transformations is to observe the structural changes while controlling the temperature.

High temperature x-ray diffraction requires a furnace to control the sample temperature. The furnace must be transparent to x-rays and must provide a homogeneous temperature over the region of the sample. Fig. 3.5 is a schematic diagram of the high temperature x-ray furnace built for this purpose. To reduce x-ray absorption, the light elements Be and C (graphite) are used for the window and heater respectively. (The absorption coefficients in cm^2/g for Cu-k$_\alpha$ wavelength are 1.5 for Be and 4.6 for C, as compared to 48.6 for Al and 308 for Fe). The core of the furnace is a hollow graphite cylinder 3 cm long and 2 cm in diameter. It serves as both the heater and a part of the sample holder. The heater is in the form of a cylinder so as to get a homogeneous temperature range over the length of the sample. The wall of the cylinder is 0.5 mm thick. A slot vertically bisects the cylinder in the sample plane so that the electric current goes up through one side of the cylinder and down through the other. Compared with no-slot cylinder, this design saves the connection space and doubles the resistance of the heater. The slot is so positioned that the x-rays do not pass through it, so the absorption due to the graphite does not alter the relative intensity of the diffracted rays at different directions. The graphite is supported by a stainless steel stand whose thermal conductivity is about one fifth of that of graphite, which reduces the heat loss and so increases the temperature homogeneity. The chamber is pumped to a vacuum of 10^{-5} torr to protect the sample from oxidation at high temperature and to minimize the heating of the Be window. A stainless steel radiation shield is also put between the heater and the shell. At

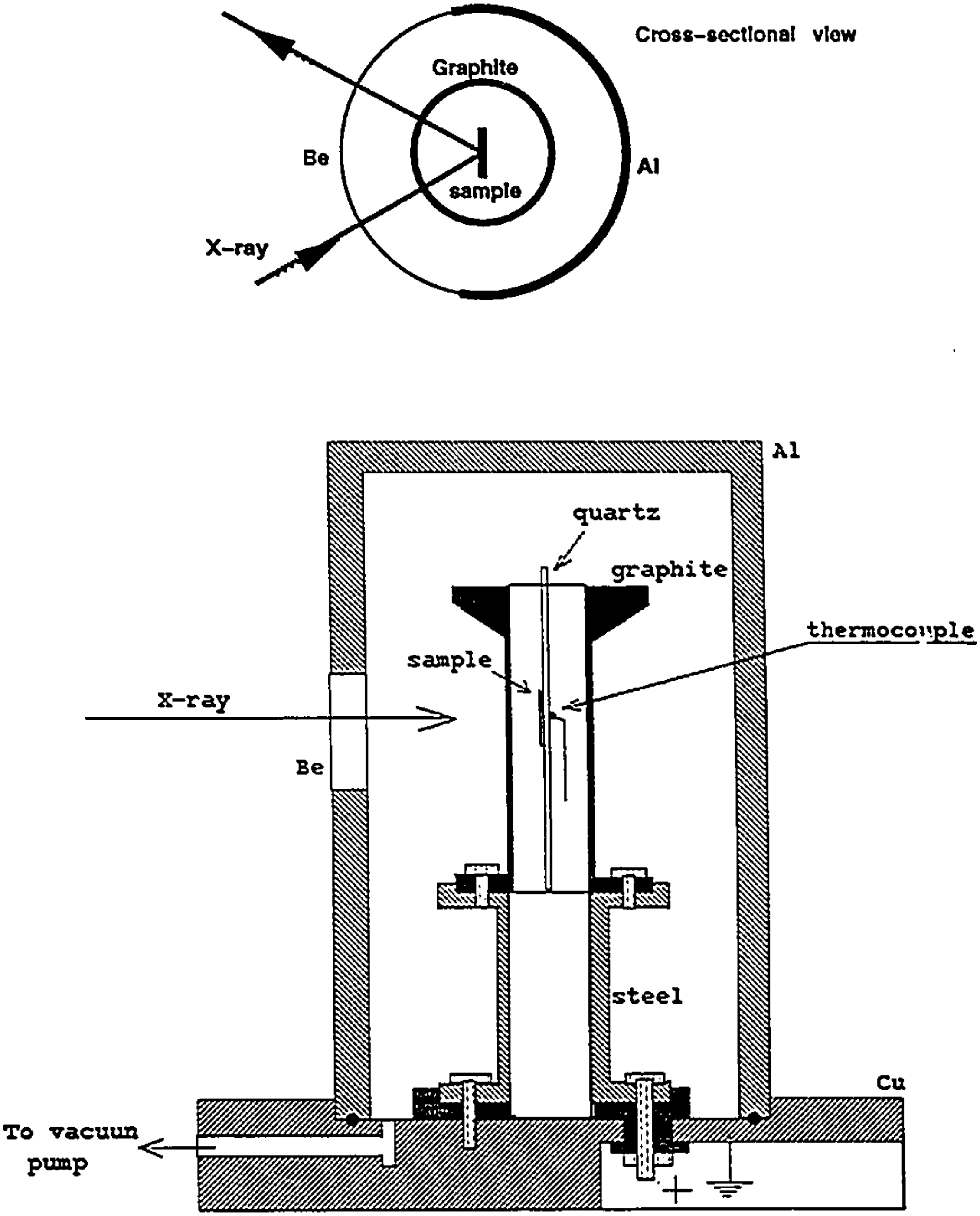

Figure 3.5: A schematic diagram of the high temperature x-ray furnace

the centre of the cylinder, the sample powders are pressed on the grooved slide of a quartz glass 1 mm thick, which produces no crystalline peaks in the x-ray diffraction pattern. A thermo-couple is placed in contact with the quartz slide behind the sample to measure the sample temperature; another thermo-couple is placed in contact with the graphite to get feedback for good temperature control. The shell of the furnace is water cooled to protect the vacuum seals and the diffractometer.

The temperature distribution was calculated in order to design the optimum geometry of the furnace. The calculation proceeded as follow:

Because of the cylindrical symmetry, the calculation can be reduced into a one dimensional heat conduction problem. Let the top of the graphite be the origin of the coordinates, and take the direction of the x-axis to be towards the bottom of the furnace. In a 10^{-5} torr vacuum, convection can be neglected, so that in the steady state, the joule heat produced by the heater is equal to the sum of the heat flowing out through the stainless steel stand and the heat of thermal radiation:

$$-K_gA_g\frac{d^2T(x)}{dx^2} = \frac{2I^2\rho}{A_g} - a\sigma 2\pi r T^4(x) \tag{3.5}$$

$$\tag{3.6}$$

with the boundary conditions

$$\begin{aligned} -K_gA_g\frac{dT(0)}{dx} &= -F_{rad} \\ -K_gA_g\frac{dT(L_g)}{dx} &= K_sA_s\frac{T(L_g)-300}{L_s} \end{aligned}$$

where:

$K_g = 1.4\ W\cdot cm^{-1}K^{-1}$ is the thermal conductivity of graphite

A_g = the area of the cross section of the graphite cylinder

T(x) = the temperature at point x

I = the heating current

ρ = the resistivity of graphite

a = emissivity of graphite

σ = the emissivity of black body

r = radius of the cylinder

F_{rad} = heat flow out of the top of the graphite by thermal radiation

L_g = length of the graphite

$K_s = 0.3\ W \cdot cm^{-1}K^{-1}$ is the thermal conductivity of stainless steel

A_s = the area of the cross section of the stainless stand

L_s = length of the stainless stand

The right hand side of the equation is the heat source, i.e. the heat produced by the current minus the heat radiated. The boundary condition at x = 0 is that the heat flow to the top equals to the heat radiated from the top; the boundary condition at $x = L_g$ is that the heat flow to the bottom equals to the flow through the stainless stand.

This equation cannot be solved analytically. However, as an approximation, we neglect the radiation term. This approximation leads to

$$T(x) = T(0) - \frac{I^2\rho}{K_g A_g^2}x^2 + \frac{F_{rad}}{K_g A_g}x$$

The homogeneous temperature zone is centred at the maximum point

$$\frac{dT}{dx} = 0 \Longrightarrow \frac{2I^2\rho}{A_g}x_{max} = F_{rad}$$

The x_{max} is such a point that the joule heat produced in region 0 to x_{max} will be transported to the top and be radiated out, while the heat produced in region x_{max} to L_g will be transported to the bottom and will flow out by conduction.

x_{max}, the position with zero gradient of temperature, is the ideal place to put the sample. However, since the radiative flow is proportional to T^4 and conductive flow is proportional to T, x_{max} will shift towards the bottom of the cylinder as the temperature increases. Hence, we can only choose a specific temperature to calculate x_{max}. The temperature of 600 K was chosen and the radiative loss estimated from the surface areas of the graphite, the radiation shield, and the shell assuming black body emission. The result is $x_{max} = 1$ cm.

Temperature homogeneity is measured by putting two thermo-couples 1.2 cm apart along the cylinder axis and centering them at the sample position (the sample

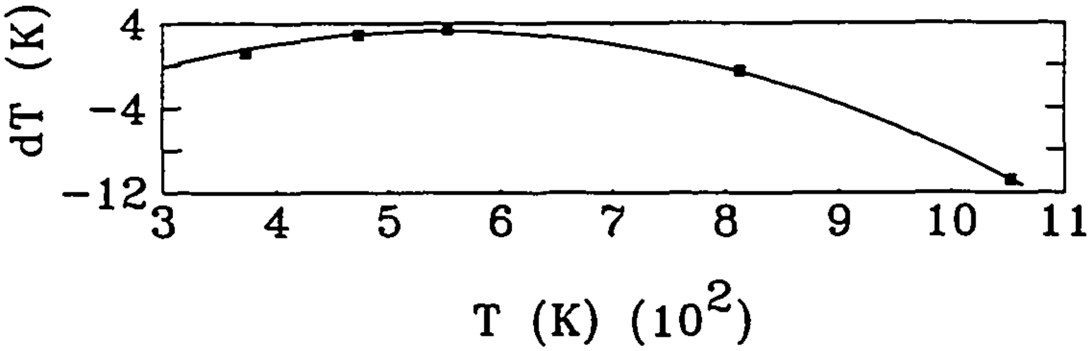

Figure 3.6: Temperature inhomogeneity of the furnace. dT is the difference of the temperatures 6 mm above and below sample centre.

size, or the beam size of the x-ray, is only 1 cm). The temperature difference between these two points is shown in Fig. 3.6. The positive value indicates the top is hotter than the bottom, and vice versa. About 800 K, the difference is zero. Below 900 K, the difference is smaller than 4 K. This homogeneity is satisfactory for the present research.

The temperature of the furnace was measured using a Chromel-Alumel thermocouple, and is calibrated by using the melting points of Bi and Al at 544.52 K and 933.25 K respectively. At the melting points, the transformation from solid to liquid changes the x-ray diffraction pattern from a group of sharp peaks to two broad peaks. The intensities of the diffraction peaks of Bi and Al are measured at various temperatures. Figs 3.7 and 3.8 show that the sharp peaks of Bi disappear at 544 ± 1 K and of Al at 933 ± 3 K, where the errors come from the temperature fluctuations in the thermometer during the x-ray scans.

To test the reproducibility of the furnace geometry, Ni diffraction patterns are taken at different temperatures. According to Eqn. 3.2, the thermal expansion of Ni will cause the diffraction peaks to shift. The experimental peaks are fit with Lorentzians to determine the peak positions from which the thermal expansion is calculated and compared to Pearson's (1958) data (see Fig. 3.9). As a result, it is found the change in geometry due to thermal expansion causes an error in 2θ smaller than 0.05° up to 800 K. In the actual experiments, the diffractometer scans in steps

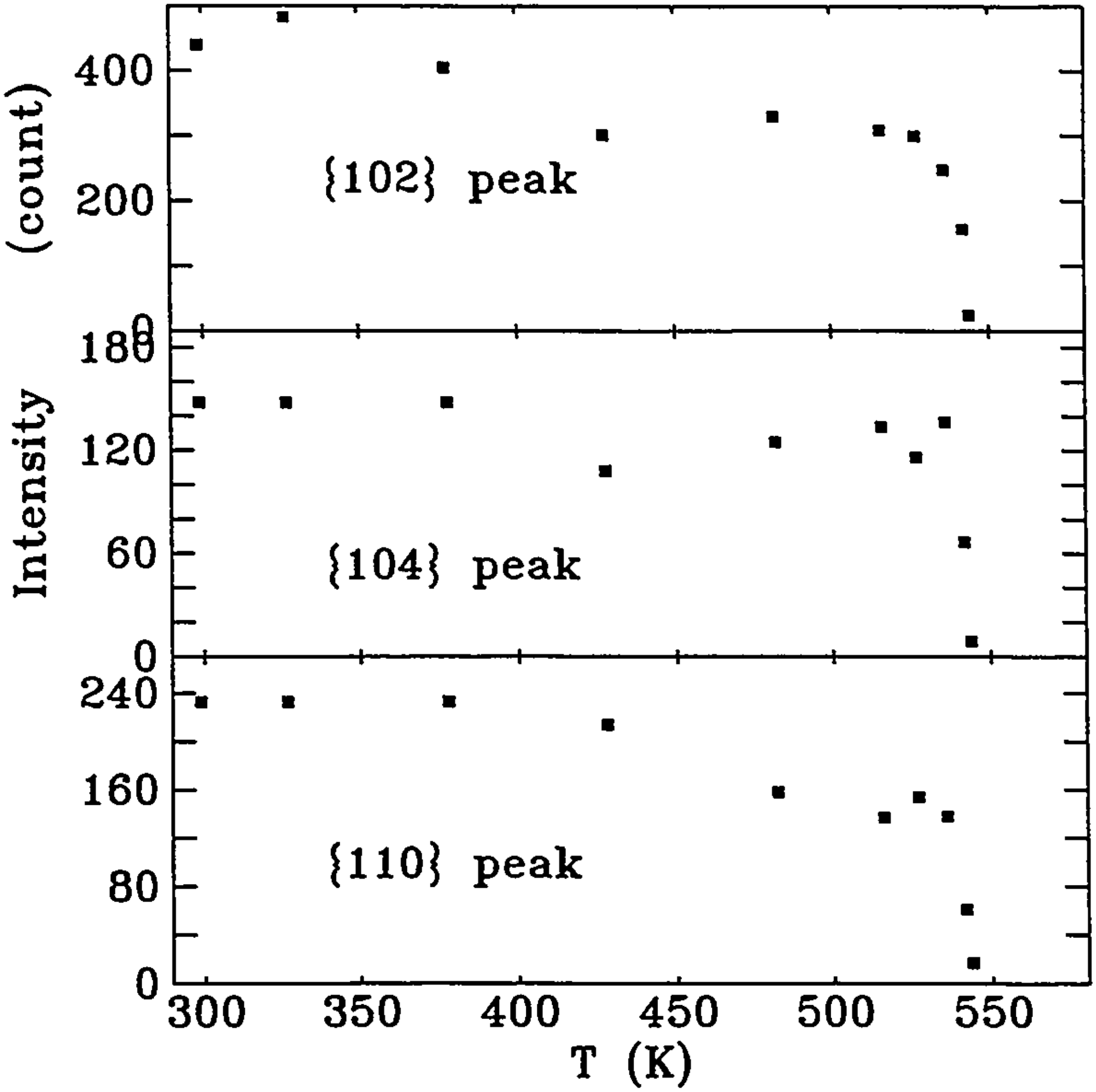

Figure 3.7: The intensities of three x-ray diffraction peaks from Bi powder versus temperature

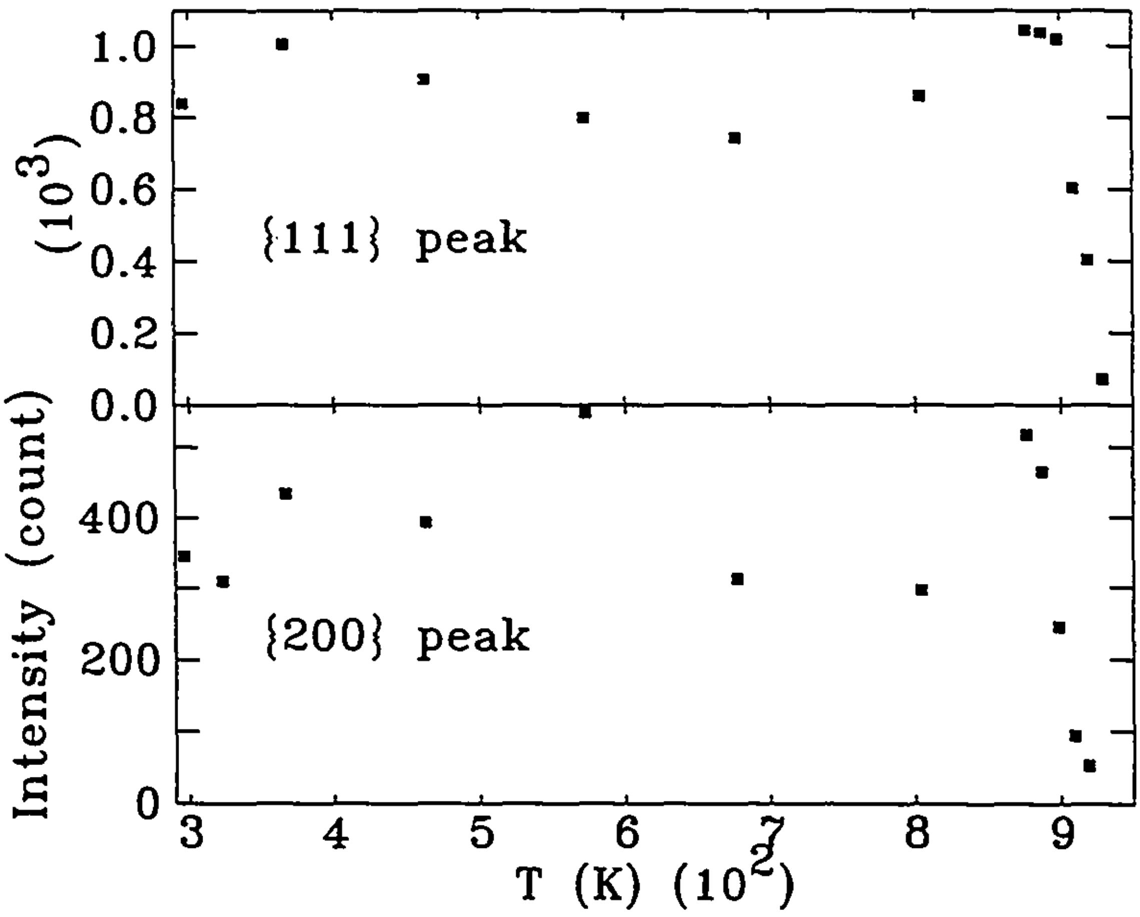

Figure 3.8: The intensities of two x-ray diffraction peaks from Al powder versus temperature

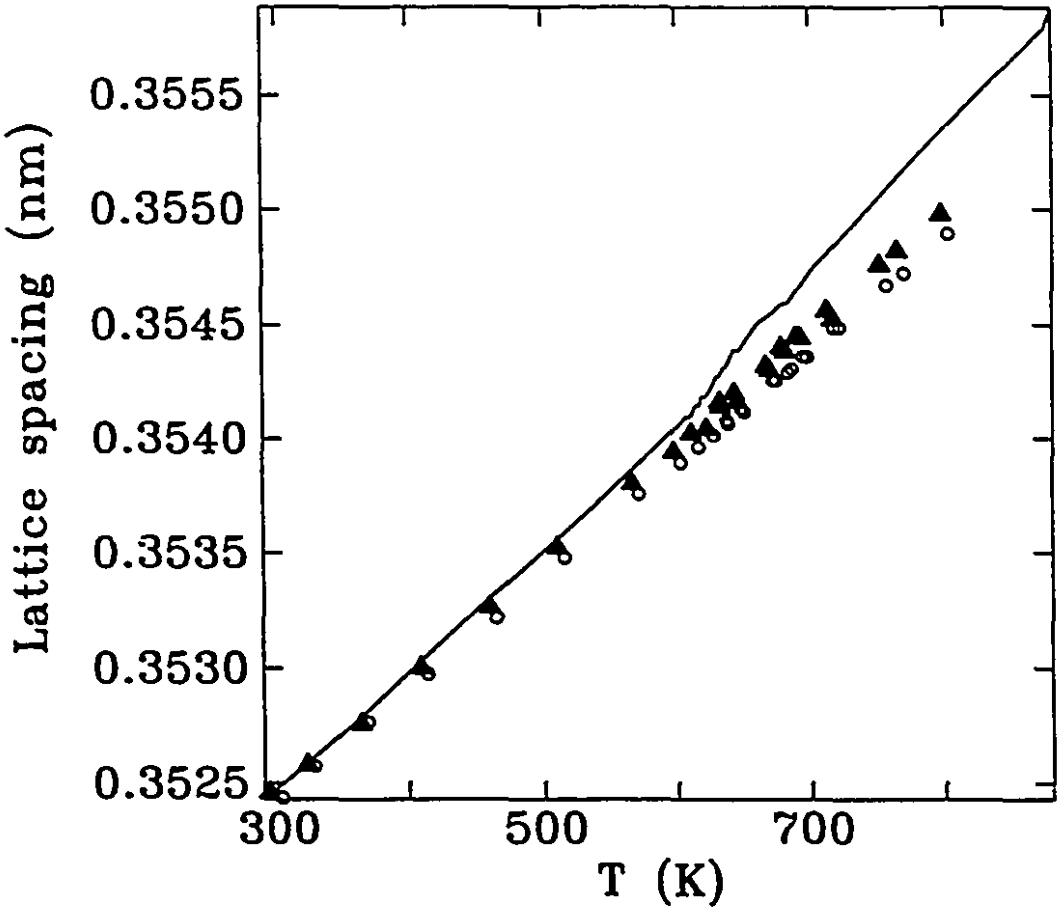

Figure 3.9: Lattice spacing of Ni versus temperature. The solid line is the data from (Pearson, 1958), the circles are from the diffraction of Ni {111} peak using the furnace, and the triangles are from {200} peak.

of 2θ of 0.1°. The error is hence insignificant for the present work.

The absorption of the x-ray by the Be window and the graphite is about 67%, obtained by comparing the peak intensities with and without the furnace. This agrees with the calculation from the Be window of 0.381 mm thick and the graphite of 0.5 mm, which predicts 70% of absorption.

3.4 Differential scanning calorimetry (DSC)

Many different phase transformations are studied in this thesis. Most of them involve enthalpy changes that can be detected by DSC, so that DSC become an important technique in the study: an isochronal DSC scan gives the temperatures and enthalpy changes of transformations over a temperature region in one experiment; the heating rate dependence of a transformation temperature provides information about the activation energy of the transformation; an isothermal DSC scan gives the enthalpy change as a function of time, which reflects the kinetics of a transformation.

The present work uses the Perkin Elmer Differential Scanning Calorimeter DSC-2c. The calorimeter has two identical holders with built-in heaters and temperature sensors. A sample in an aluminium capsule is put in one of the holders, and a reference (usually an empty capsule) is put in the other holder. Both of the holders are programmed to be heated or cooled at a specific rate. A feed back system provides differential electrical power to the heaters to compensate for temperature fluctuation between the holders, so the temperature of the holders is essentially unaffected by the sample behaviour. The differential power required to maintain the balance condition directly corresponds to the heat flow in or out of the sample, and is recorded in millicalories per second as a function of temperature. During measurements, an argon flow passes through the holder chambers to protect the samples from oxidation.

Fig. 3.10 gives an example of a DSC plot. The heat released from the sample, the exotherm, results in a peak on the plot; the heat absorbed by the sample, the endotherm, results in a valley. The heat flow can be rescaled to heat capacity C_p by dividing it with the heating rate, and the enthalpy change $\Delta H = \int \Delta C_p dT$ can be calculated from the area of a peak for the corresponded reaction or transformation. The peak positions are of course related to transformation temperatures.

3.5 Thermomagnetometry

For the study of magnetic transformations, thermomagnetometry is used in addition to DSC. Combined with DSC and x-ray diffraction, thermomagnetometry provides more information about magnetic phases.

The thermomagnetometor used in present work is actually a Perkin-Elmer TGA-7

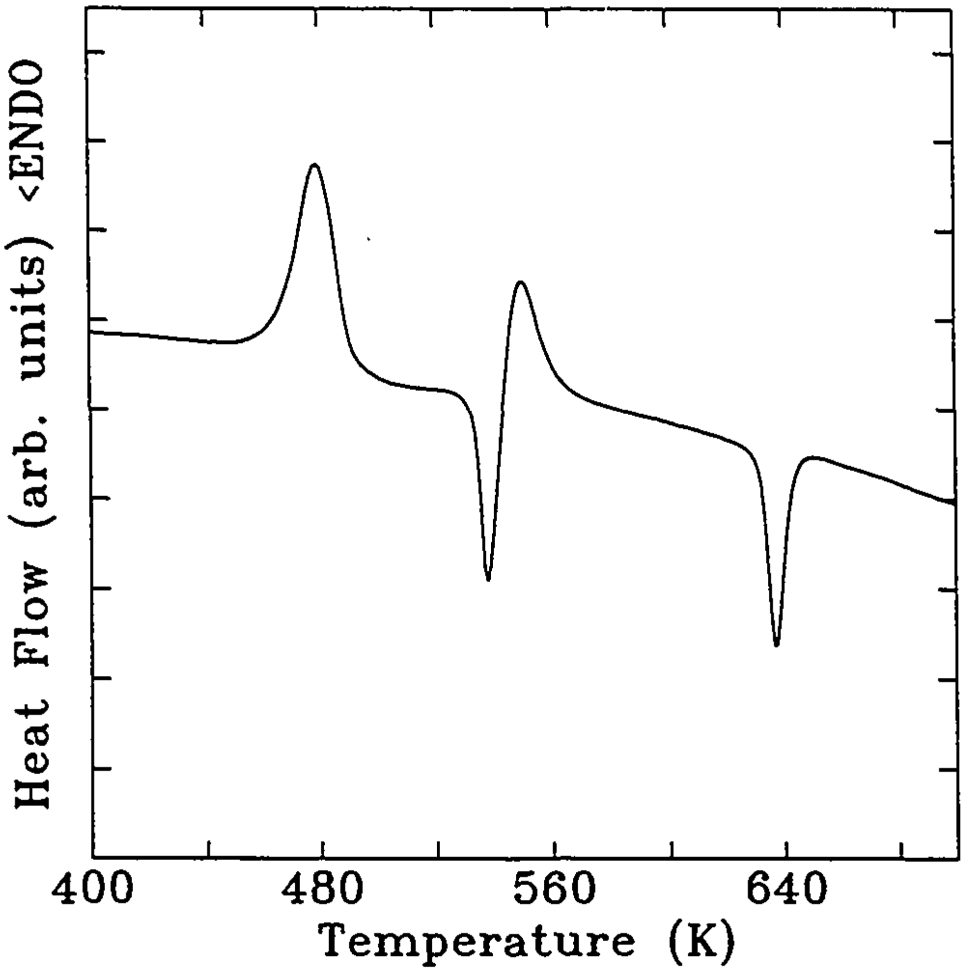

Figure 3.10: A typical DSC scan of MnBi ribbons at the heating rate 80 K/min

thermogravimetric analyzer (TGA), with a field gradient introduced at the sample area. The field gradient and strength are produced simply by putting a small "U" shape magnet outside the furnace tube. The TGA heats and weighs a sample at the same time, and records the weight changes as a function of temperature. The gradient of a magnetic field exerts an extra force on a magnetic sample, so any change of the magnetization of the sample is reflected as a "weight" change. Fig. 3.11 is a schematic diagram of the TGA. The microfurnace is about 23 mm high and 13 mm in diameter, containing a platinum wire that functions as both a heater and a resistance thermometer. Having a small volume, the furnace can heat and cool rapidly (up to $200°C/min$). It can reach $1000°C$ with a precision of $\pm 2°C$. The microbalance operates as a high gain electromechanical servo system which permits the measurement of weight changes as small as 0.1 microgram. When a sample is placed in the sample pan, the beam that supports the sample pan deflects. A detector of the beam position measures the deflection with an optical sensor and uses a d.c. current to restore the beam to its original position. The amount of current needed to restore the beam is a direct measure of the weight on the beam. The measurements conducted in this work has the sample mixed with a piece of Alumel alloy, whose Curie point of 436 K is used to calibrate the temperature.

3.6 Vibrating sample magnetometer

The magnetization as a function of field (i.e. a hysteresis loop) was measured by a vibrating sample magnetometer (VSM). Fig. 3.12 is a schematic diagram of VSM used in this work (Model FM-1, Princeton Applied Reseach Co. New Jerdey). About 10mg of sample is bounded by epoxy resin, and then is hold by a screw at the sample holder. An adjustable DC magnetic field of up to 1.7 Tesla is applied to magnetize the sample. The vibrating sample induces in the pick-up coil an AC voltage that is proportional to the magnetic moment of the sample. The voltage signal is amplified by a lock-in amplifier and recorded as a function of the field H. The temperature of

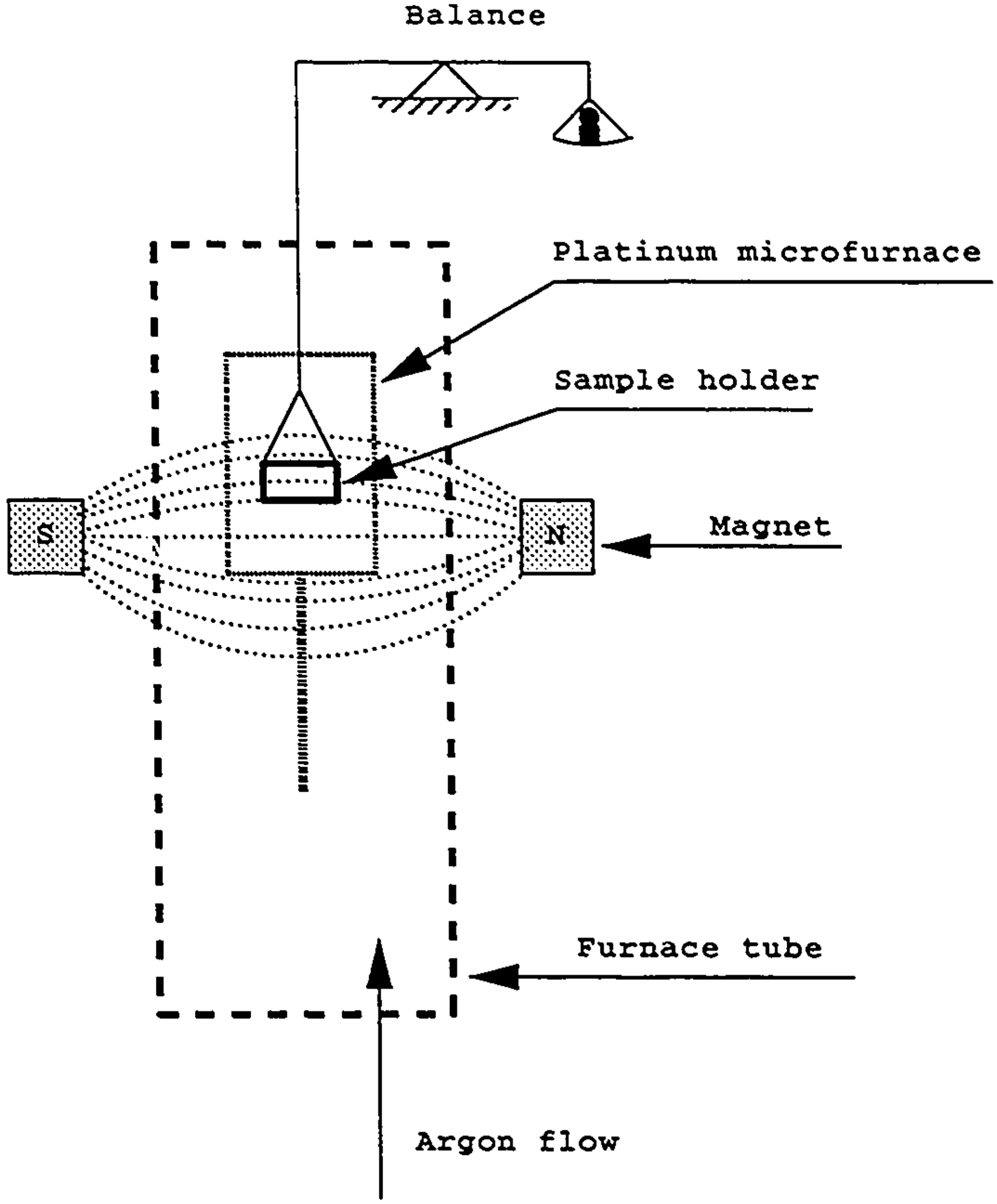

Figure 3.11: A schematic diagram of the thermomagnetomery

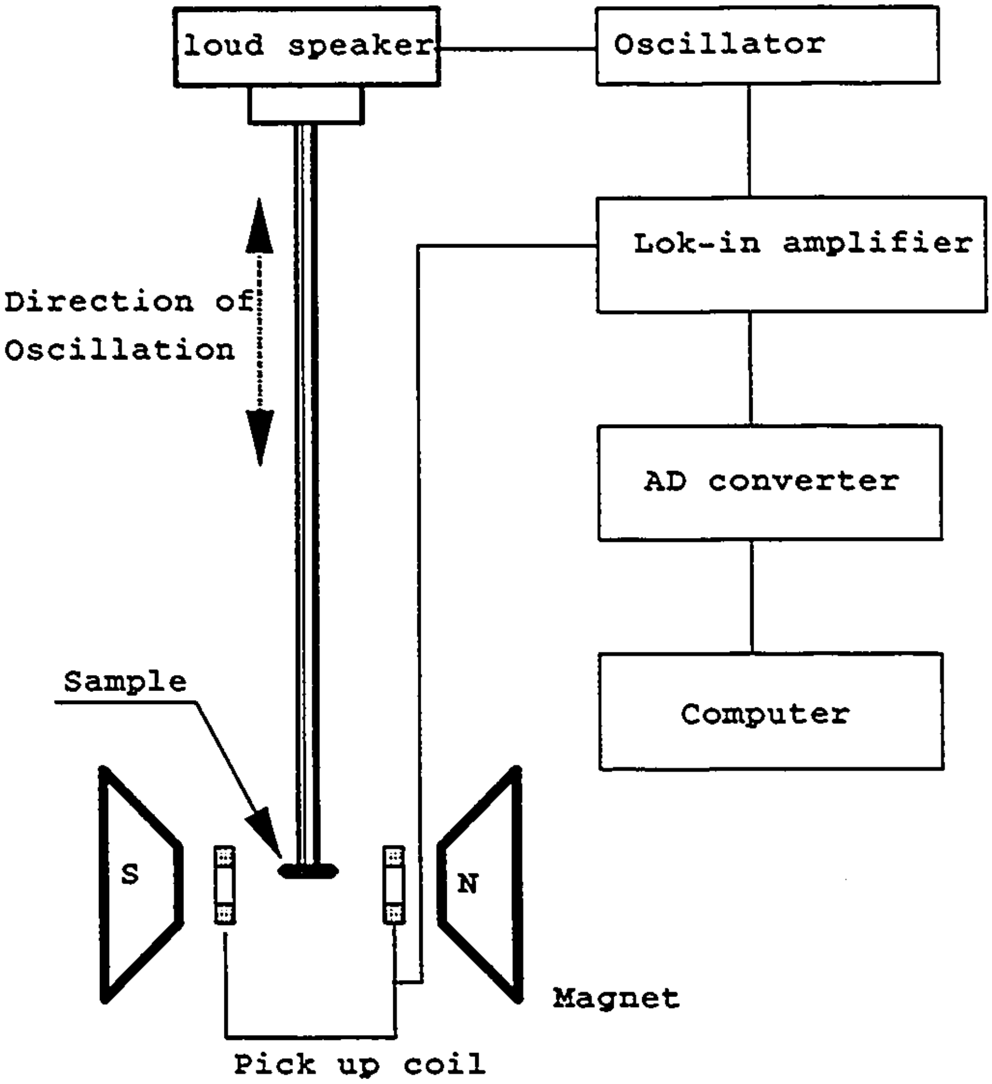

Figure 3.12: A schematic diagram of vibrating sample magnetometer

the sample can be controlled in the temperature range from 300 to 500±1 K in a vacuum of about 10^{-5} torr.

Chapter 4

Amorphous MnBi

The ribbons of MnBi produced by melt-spinning are brittle, shiny on both sides, and typically 1 cm long by 1 mm wide and 10 μm thick. They show no observable deterioration under normal atmosphere even after 3 years. The characteristic x-ray energy spectrum analysis on several samples of a batch of ribbons by scanning electron microscope shows a composition of 51 ± 1 at.% Mn and 49 ± 1 at.% Bi.

4.1 Characterization of amorphous MnBi

X-ray and electron diffraction detect no long range order in the as-made ribbons, as expected from an amorphous phase. Figs 4.1 and 4.2 show the x-ray and electron diffraction patterns of the as-made ribbon, respectively. Besides the extra sharp rings seen in the electron diffraction (which may be indexed as MnO[1]), the two patterns are essentially the same. Comparing Fig. 4.1 with Fig. 3.3, it is clear that the as-made ribbons lack long range order. Fig. 4.1 is, however, a complicated pattern because it has four broad peaks, while most metallic glasses have only two broad peaks in their x-ray diffraction over the same range of scan [see (Takayama, 1976) for example]. This raises the question: Is the unusual pattern produced by a nanocrystalline

---

[1] The very thin ribbon edges used in electron microscope have a proportionally high oxide layer content.

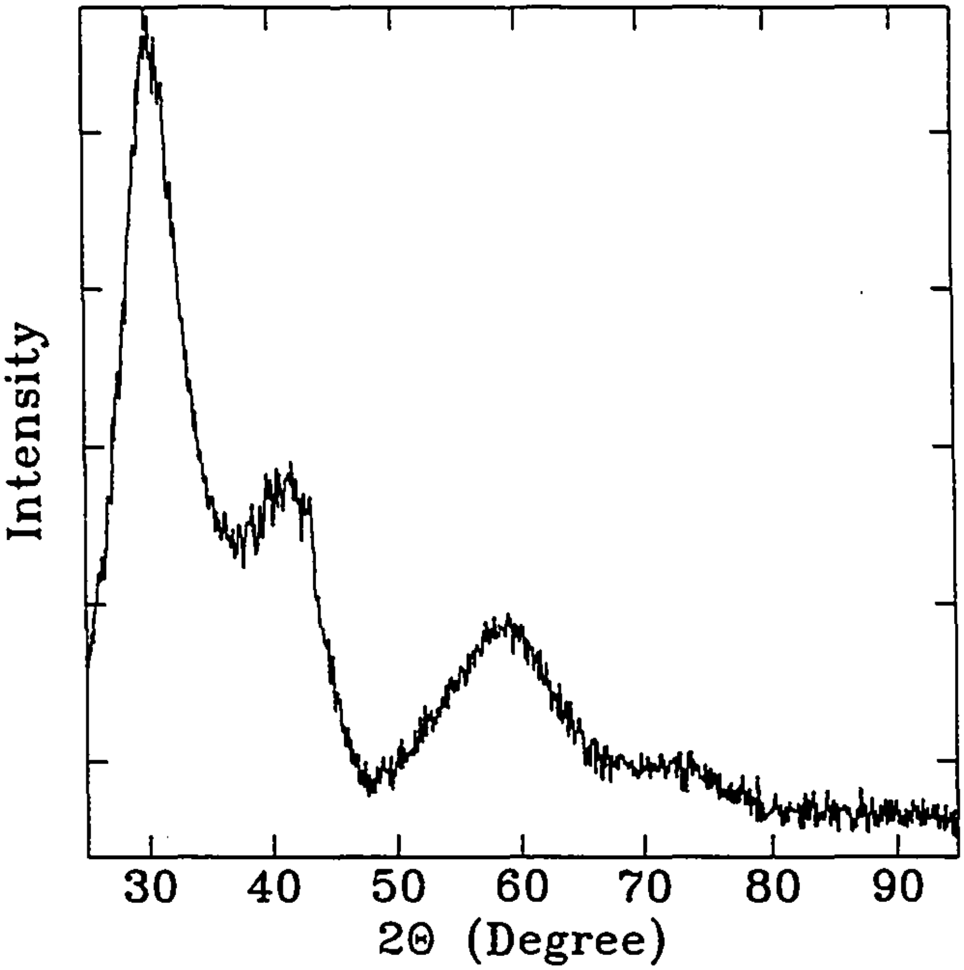

Figure 4.1: X-ray diffraction pattern of as-spun MnBi ribbons

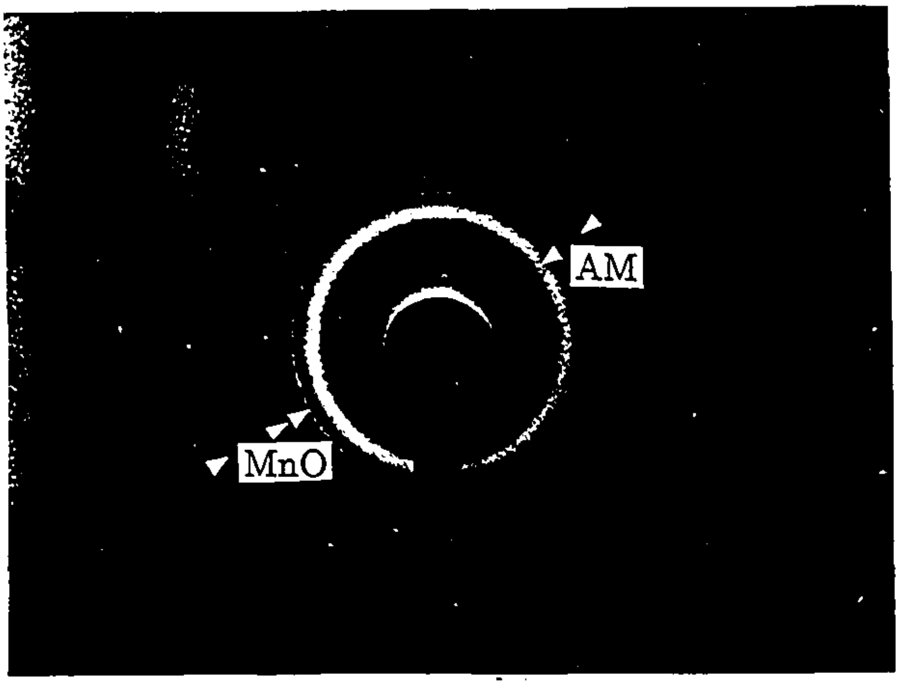

Figure 4.2: Electron diffraction pattern of as-spun ribbons. The sharp rings due to MnO crystals are indicated

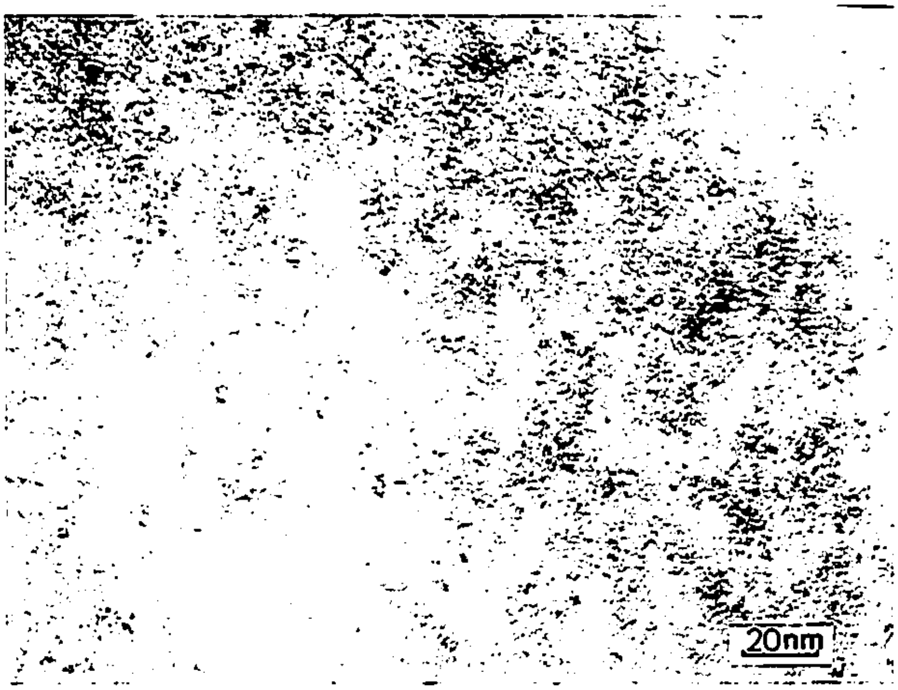

Figure 4.3: Electron micrograph of as-spun ribbons. The small dark grains are MnO crystals

phase or by two separated amorphous phases? A close examination on the electron micrograph (Fig. 4.3) found no distinguishable crystal or grain structure down to the resolution (1 nm) of the instrument. Furthermore, the electron diffraction pattern (Fig. 4.2) is similar to that found for amorphous Mn-Bi formed by vacuum deposition (Yoshida, Yamada and Furukawa, 1968). These suggest that the as-made ribbons are not nanocrystalline.

Various tests have been performed to confirm this.

One test is to heat the sample and see whether the broad peak narrows into a sharp peak as a result of crystal growth. If the ribbons were nanocrystalline, the first peak would be broad but correspond to a strong crystalline line (see Eqn. 3.3). Ribbons have been heated to different temperatures and then quenched back to room temperature. No strong line was found at the position of the centre of the broad peak. Fig. 4.4 shows the x-ray results. In fact, the centre of the broad peak does not correspond to the strongest lines of any known phases of MnBi in Table2.1. This confirmed that the as-made ribbons cannot be nanocrystals.

Another test is to compare the diffraction pattern with that of liquid and amorphous Bi. The scattering factor of an atom is proportional to the electron density, and the x-ray intensity of coherent scattering is proportional to the square of the scattering factors (see Eqn. 3.4). Since Bi has 83 electrons per atom and Mn has only 25, the intensity of x-ray scattered from Bi is roughly 11 times as strong as that from Mn. So the x-ray diffraction pattern of amorphous MnBi is dominated by Bi scattering, and is similar to that of amorphous and liquid Bi. Table 4.1 compares the positions of the four peaks from x-ray pattern of as-made ribbons with those of amorphous and liquid Bi. That the first peak of MnBi is slightly higher than those of amorphous Bi may be attributed to shorter atomic spacing due to the smaller Mn atoms. A sample of MnBi ribbons has been heated to about 700 K for two days in a vacuum of about 10^{-4} torr. As a result, the Mn was almost all oxidized, and the high temperature x-ray scan then showed three peaks due to MnO and the typical pattern of liquid Bi (Fig. 4.5). Comparing to the x-ray patterns of the as-spun ribbons, the

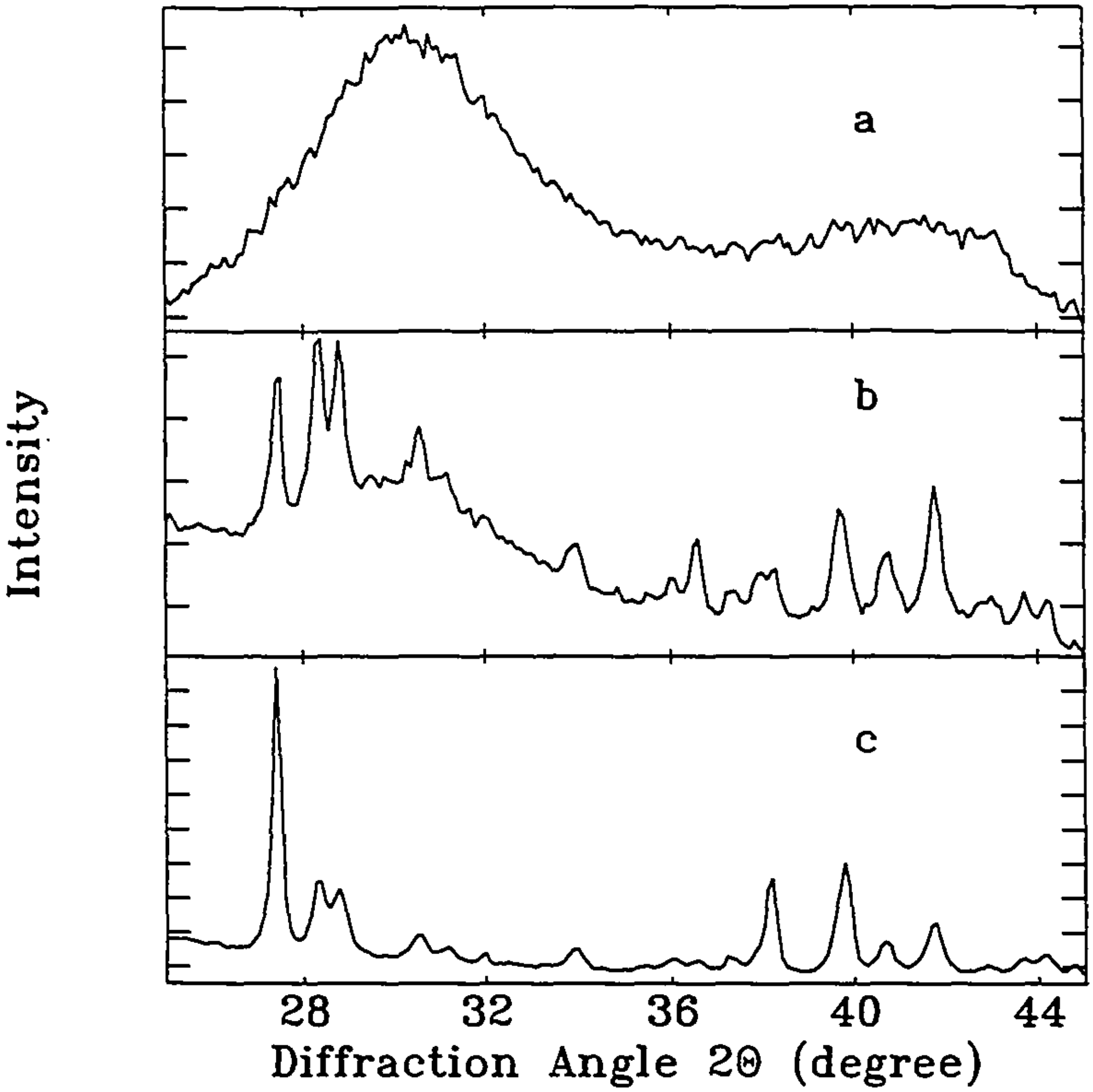

Figure 4.4: X-ray diffraction patterns showing the crystallisation. (a): from as-spun ribbons; (b): from sample that is heated to 400 K at 80 K/min, annealed at that temperature for 3 hrs, and cooled down to room temperature at 320 K/min; (c): from sample that is heated to 500 K at 80 K/min and cooled down to room temperature at 320 K/min.

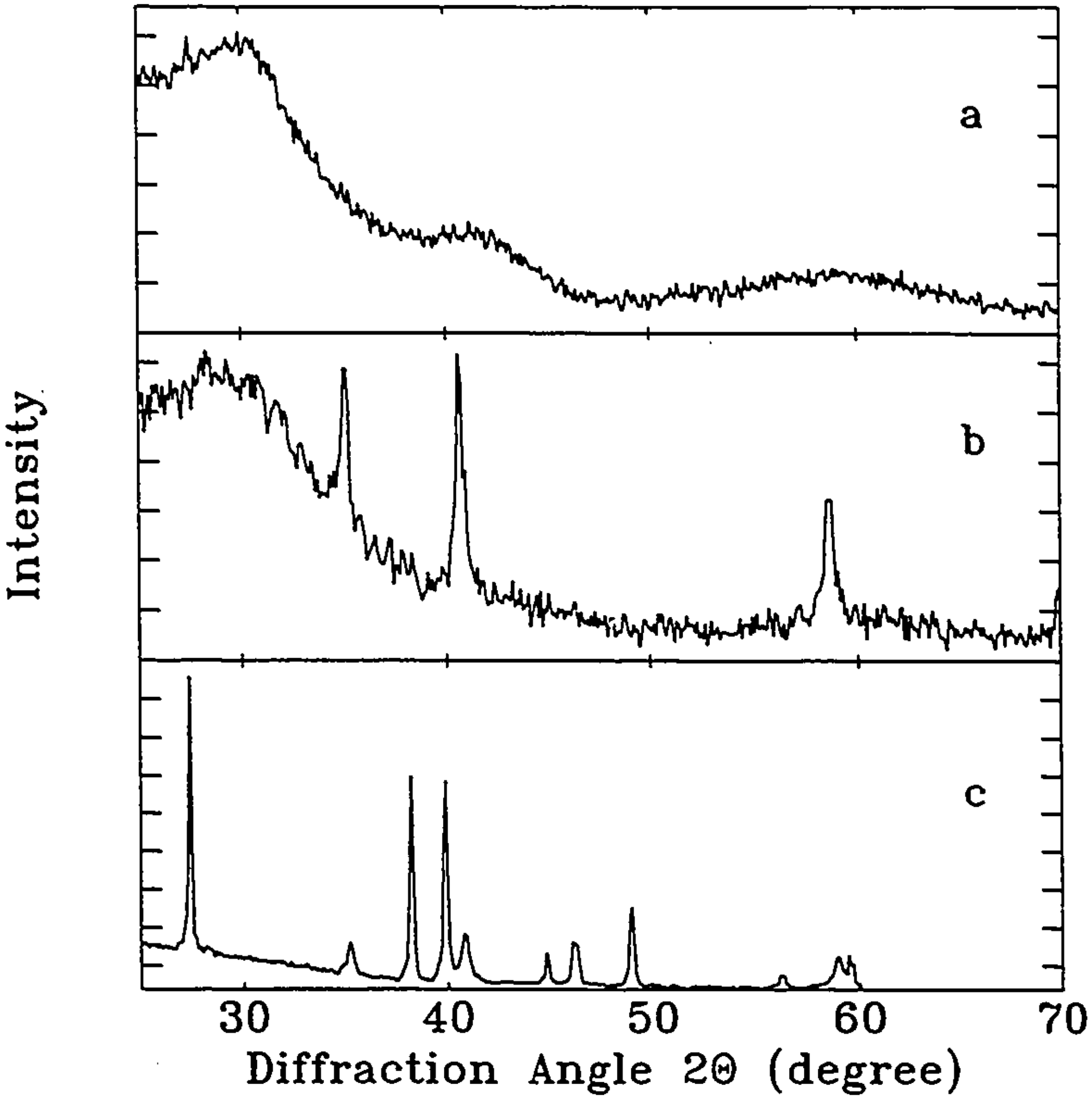

Figure 4.5: X-ray diffractions of one sample of as-spun ribbons at different temperatures. (a): The first room temperature scattering shows amorphous pattern; (b): After operating at high temperature for a long time, all Mn are oxidized, the scan at 685 K shows three MnO peaks and two broad peaks corresponding to liquid Bi; (c): Back to room temperature again, only crystalline Bi and MnO can be seen.

phase	reference	peak positions			
		$Q(\AA^{-1}) = 4\pi sin\theta/\lambda$			
as-spun ribbons	Present work	2.1	2.8	4.0	4.9
liquid-Bi	Present work (685 K)	2.0	-	4.0	-
liquid-Bi	(Takagi, 1956) (673 K)	2.0	-	4.2	-
liquid-Bi	(Takagi, 1956) (383 K)	2.0	2.9	4.0	-
liquid-Bi	(Waseda, 1977) (544 K)	2.11	2.85	4.12	-
liquid-Mn	(Wasedai and Tamaki, 1975)	-	2.83	-	5.19
amorphous Bi	(Behrndt, 1970)	1.98	2.88	3.96	-
amorphous Bi	(Fujime, 1966)	2.0	2.85	4.1	6

Table 4.1: The peak positions of Mn and Bi in liquid or amorphous.

two peaks from liquid Bi are essentially the same as the first and the third peaks from the as-spun ribbons, if we allow for the shifting of the first peak to lower angle as a result of thermal expansion, and for the flattening of the second because of the Debye-Waller factor (see Eqn. 3.4).

The second and fourth peaks of amorphous Bi or MnBi and the second peak of supercooled liquid Bi, which do not appear in the x-ray pattern of liquid Bi, suggest that the Bi-Bi correlation is stronger in the amorphous and supercooled liquid state than in the liquid state (Takagi, 1956; Richter, 1969). The two extra peaks, unfortunately, coincide with those of liquid Mn (see Table. 4.1), so the question of phase separation in the amorphous MnBi cannot be answered by x-ray diffraction.

In conclusion, the as-made ribbons are identified by x-ray diffractions and electron microscopy as amorphous MnBi. Evidence will be presented in Chapter 5 to suggest that phase separation occurs before or at the first step of the crystallization.

4.2 Discussion on formation of amorphous MnBi

Since the Mn-Bi phase diagram (Fig. 2.1) shows no deep eutectic point, the formation of amorphous MnBi may seem surprising, since most metal glasses are formed around deep eutectic compositions where melt temperatures and liquidus are strongly depressed. Generally, the glass-forming ability (GFA) of a metallic alloy has been found to increase with the depression of melt temperatures. Donald and Davies (1978) define this depression ΔT^* by the relation

$$\Delta T^* = \frac{T_{liq}^{mix} - T_{liq}}{T_{liq}^{mix}} \tag{4.1}$$

where T_{liq}^{mix} is a linear interpolation of the melting points of the elements or compounds T_m^A and T_m^B, while T_{liq} is the liquidus or melting point of the alloy. They found that a metallic glass can generally be formed by quenching the melt at a cooling rate of about 10^6 K/s if $\Delta T^* \gtrsim 0.20$. However, MnBi has neither eutectic, nor depressed liquidus, yet still forms a glass by melt-spinning. The criterion of the depressed liquidus therefore fails to explain the formation of amorphous MnBi.

Davies (1976) calculated a relationship between the critical cooling rate R_c and the reduced glass temperature T_g/T_m, where T_g is the glass transition temperature at which a supercooled liquid transforms to a glass, and T_m the melting point. His model, based on the kinetics of nucleation and growth, predicts that for T_g/T_m larger than 0.5, R_c can be less than 10^8 K/s. Experimentally, it is found that the metallic glasses formed by melt-spinning have T_g/T_m in the range 0.45 to 0.65. If T_g is detected in a glass, the crystallization temperature T_x will follow just above T_g (Chou and Turnbull, 1975; Buschow, 1981), where the alloy is in a supercooled liquid state. In practice, therefore, wherever the information about T_g is lacking, the T_x at the highest heating rate of observation is taken as the best estimate of T_g (Davies, 1976; Donnald and Davies, 1978). The T_g of MnBi has not been detected. However, we will show in Chapter 5 that the highest T_x detected is 480 K, which we take as an approximation of T_g. From Fig. 2.1, the T_m of MnBi is 1370 K. The MnBi has then the estimated T_g/T_m ratio of about 0.35, which corresponds to a R_c higher than 10^8 K/s according to Davies's model. This cooling rate is far beyond the reach of melt-spinning. Again, this criterion fails to explain the formation of amorphous MnBi.

One criterion for GFA that does not refer to phase diagrams is the size difference of alloying atoms. It is necessary to have about 15% radius mismatch of the constituent atoms in a melt in order to form a glass (Takayama, 1976; Cahn, 1991). Ueno and Waseda(1968) gave an empirical relation between the solution concentration and the atomic volume mismatch of a glass-forming alloy:

$$|\Delta V_{AB}/V_A| \cdot c_B^{min} = 0.1 \tag{4.2}$$

with

$$\Delta V_{AB}/V_A = (r_B/r_A)^3 - 1$$

where c_B^{min} is the minimum solute concentration of B atoms necessary to obtain glassy phases by rapid quenching from the melt, and r are the radii of the atoms. Taking a radius of 1.70 Å for Bi and 1.35 Å for Mn (Takayama, 1976), the glass-forming region of concentrations estimated from Eqn. 4.2 is from $Mn_{18}Bi_{82}$ to $Mn_{92}Bi_8$.

Thus taking the size ratio criterion, we can expect Mn-Bi to form a glass over a large range of compositions. Three other compositions, Mn_3Bi, Mn_2Bi_3 and $MnBi_2$, have also been subjected to melt-spinning. Fig. 4.6 shows the x-ray diffraction patterns of these samples. The as-made Mn_2Bi_3 indeed appears amorphous. The Mn_3Bi and $MnBi_2$ are, however, crystalline and their peaks are the same as crystallized MnBi, except that Mn_3Bi shows some significant extra Mn peaks, probably because of the extended segregation in the miscibility gap in the liquid state (see Fig. 2.1). Thus, although the range of amorphization by melt-spinning for the Mn-Bi system may be larger than that from MnBi to Mn_2Bi_3, all the compositions are inside the limits predicted by size effect consideration.

Because the atomic size mismatch explains, to some extent, the GFA of MnBi, we also tried to melt-spin some other BiT (where T is a transition metal). FeBi, NiBi, CoBi, and CuBi have about the same size mismatch as MnBi has, but they cannot be spun to from glasses. This result suggests that the size effect may be a necessary but

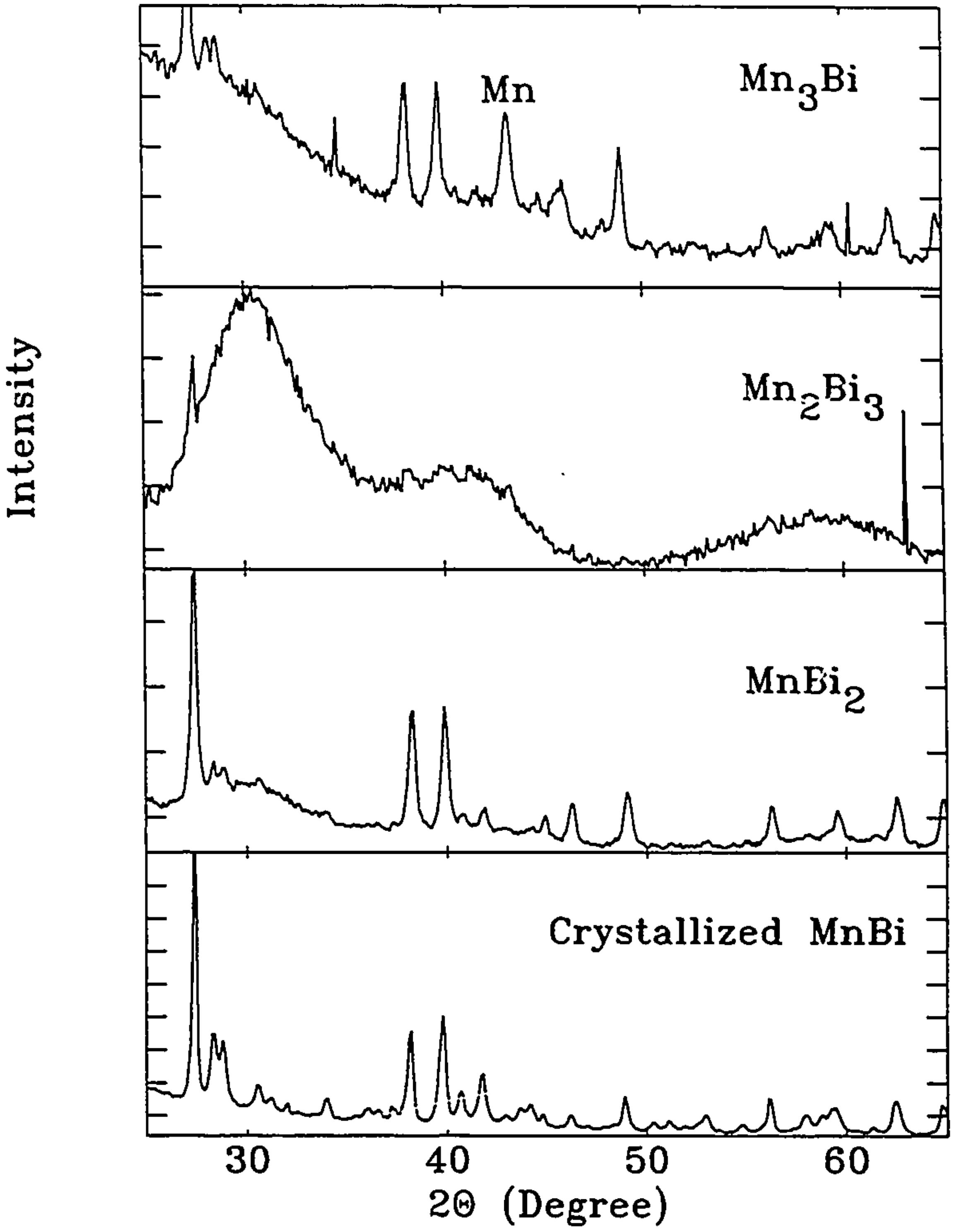

Figure 4.6: X-ray diffraction patterns of different compositions of as-spun Mn-Bi, compared with the pattern of crystallized MnBi ribbons

not sufficient condition, and raises the question of what distinguishes these systems from Mn-Bi.

Comparing the phase diagrams of Mn-Bi with Fe-Bi, Ni-Bi, Co-Bi, and Cu-Bi (Massalski *et al.*, 1986) (Figs. 4.7, and 4.8) one can see that they are very similar: the liquidus is above or close to the linear interpolation of the melting points and there is essentially no melting point depression. The most distinctive features of the phase diagram of Mn-Bi are the many horizontal lines, reflecting the multiple transformations in the coexistent region of liquid and solid. Is this responsible for the GFA of MnBi?

The multiple transformations imply that the solidification of MnBi involves a sequence of physical processes instead of a single process. If the temperature range between T_g and T_m is small (or T_g/T_m is large) so that the quenching can leave the supercooled liquid no time for nucleation, the system will have a better GFA. For multiprocess solidification, the temperature difference between the beginning and end of each process is smaller than the difference from T_m to T_g, so that every process gets less time than a single process solidification does at the same quenching rate; or, they are more difficult to be completed than a single nucleation process. So the horizontal lines in the Mn-Bi phase diagram have the good reason to contribute to GFA.

How, then, do the horizontal lines divide the solidification into multiprocesses? Let us consider one of the transformations, and see, for example, what may happen when a rapidly cooling melt of MnBi passes 983 K, the α-Mn to β-Mn transformation. Just above 983 K, the melt contains segregated β-Mn whose size may not be large enough to be stable because of the fast quench. Below 983 K, the β-Mn becomes unstable, and will transform to stable phase of α-Mn. However, they are small particles in a Mn-Bi melt, and solid-solid transformations are generally much slower than liquid-solid transformation(Christian, 1965) because of elastic strain energy and small diffusion coefficients. So the dominating process is likely to be nucleation of α-Mn from the liquid and dissolving β-Mn in the liquid. Assuming the particles of β-Mn formed

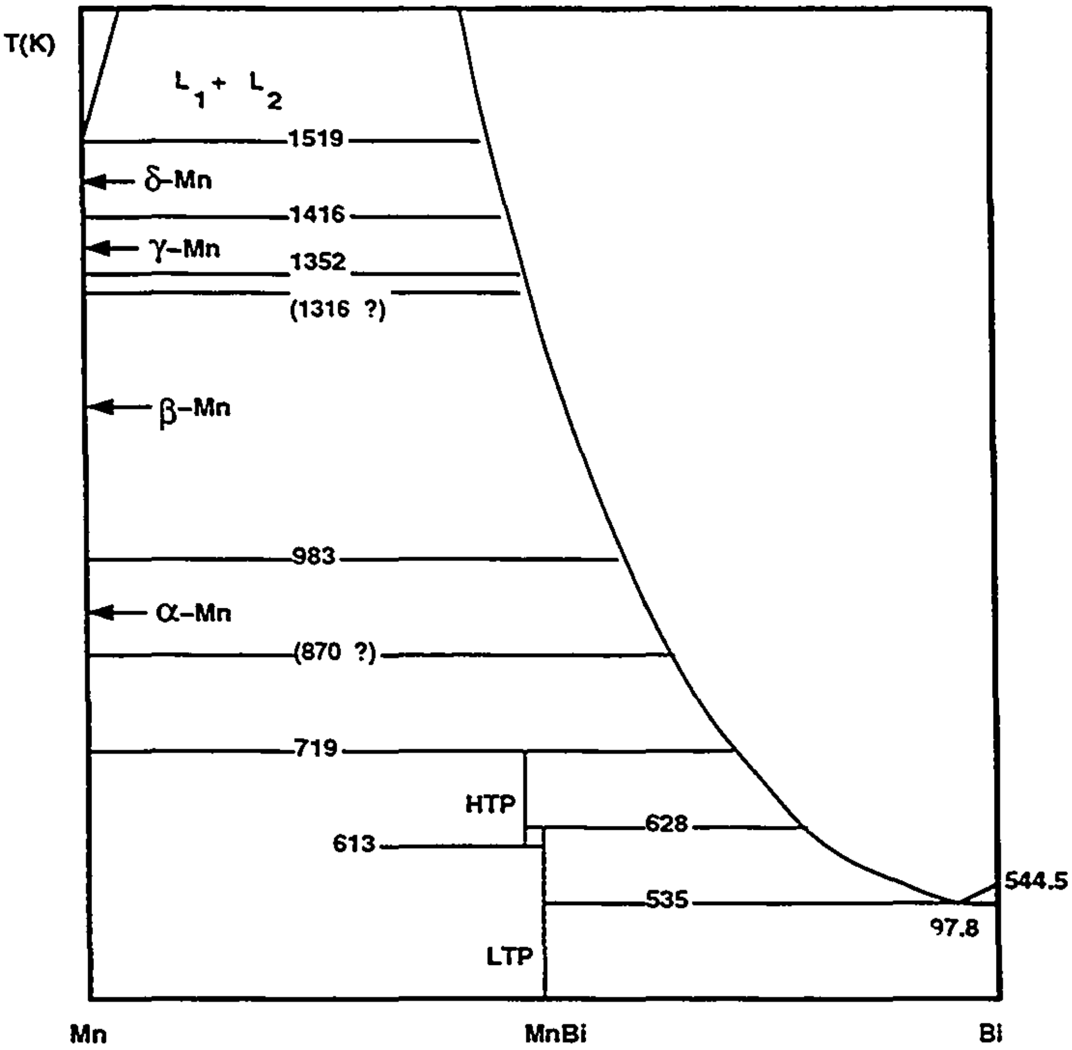

Figure 4.7: Mn-Bi phase diagram.(Hansen, 1958; Chen, 1974)

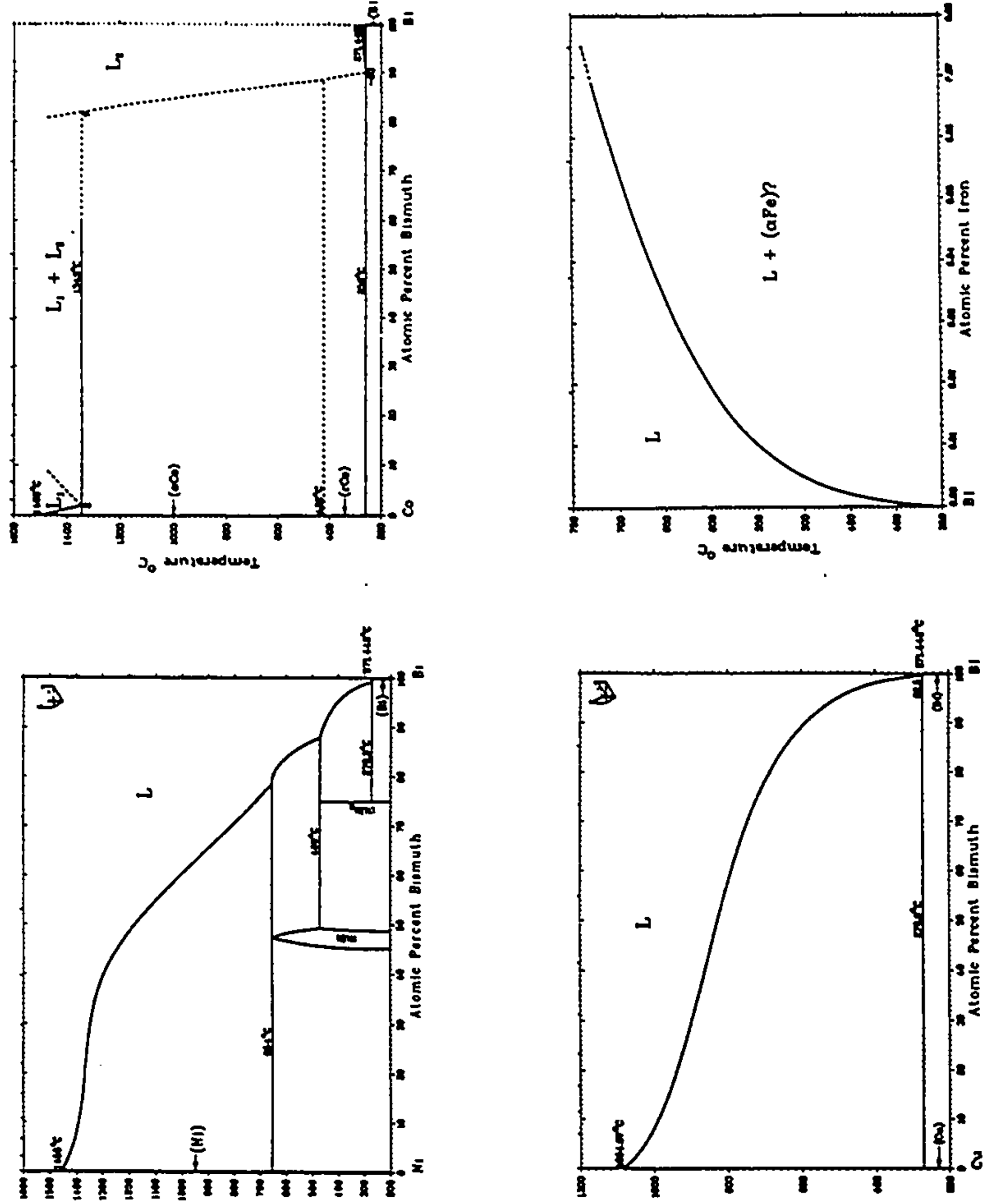

Figure 4.8: Ni-Bi, Co-Bi, Cu-Bi and Fe-Bi phase diagrams

during the rapid quench are so small that they will be dissolved completely when the melt is supercooled to the glass temperature near 480 K, the solidification history above 983 K will leave no trace in the final state. Consequently, the 983 K is effectively the beginning of the solidification viewed from the final state. For every horizontal line in Fig. 4.7, a similar scenario is expected. Since each of them erases the history of solidification above that temperature, the lowest one in the liquid-solid coexistent region will act as an effective melting point as far as rapid solidification is concerned. In Fig. 4.7, the lowest transformation is at 870 K. However, this is an unknown transformation, so that we well take the next lowest transformation, the β-Mn to α-Mn at 987 K, as the effective melting point. The melting point depression ΔT^{*} thus calculated becomes positive, and T_g/T_m becomes 0.49, in agreement both with empirical expectation and Davies's model of a R_c about 10^6 K/s.

In conclusion, the size difference between atoms of Mn and Bi is an important factor for the existence of a stable amorphous MnBi; the multiple phase transformations in the liquid-solid coexistent region play an essential role in the kinetics of forming MnBi in the glassy state.

Chapter 5

Phase transformations of rapidly solidified MnBi

Amorphous MnBi is not in configurational equilibrium, and transforms to more stable crystalline states upon heating. The enthalpy change of the transitions can be detected by DSC. Fig. 5.1 shows DSC scans of as-made ribbons at different heating rates. There are four signals in a typical DSC scan: two exothermic peaks and two endothermic peaks. The two endothermic peaks reflect reversible phase transformations, for they are repeatable in subsequent scans and also appear as exotherms during cooling. The equilibrium phase diagram (Fig. 2.1) shows that the first endotherm corresponds to the melting of Bi, and the second to the transformation of LTP to HTP. The two exothermic peaks reflect irreversible transformations, for they do not appear after the first heating, nor during cooling, nor during a repeated scan. As we will see, the first exotherm corresponds to crystallization of amorphous MnBi to metastable phases, and the second corresponds to the formation of LTP. After each of the exotherms, the alloy becomes more and more stable. Detailed discussions on each of the transformations are presented.

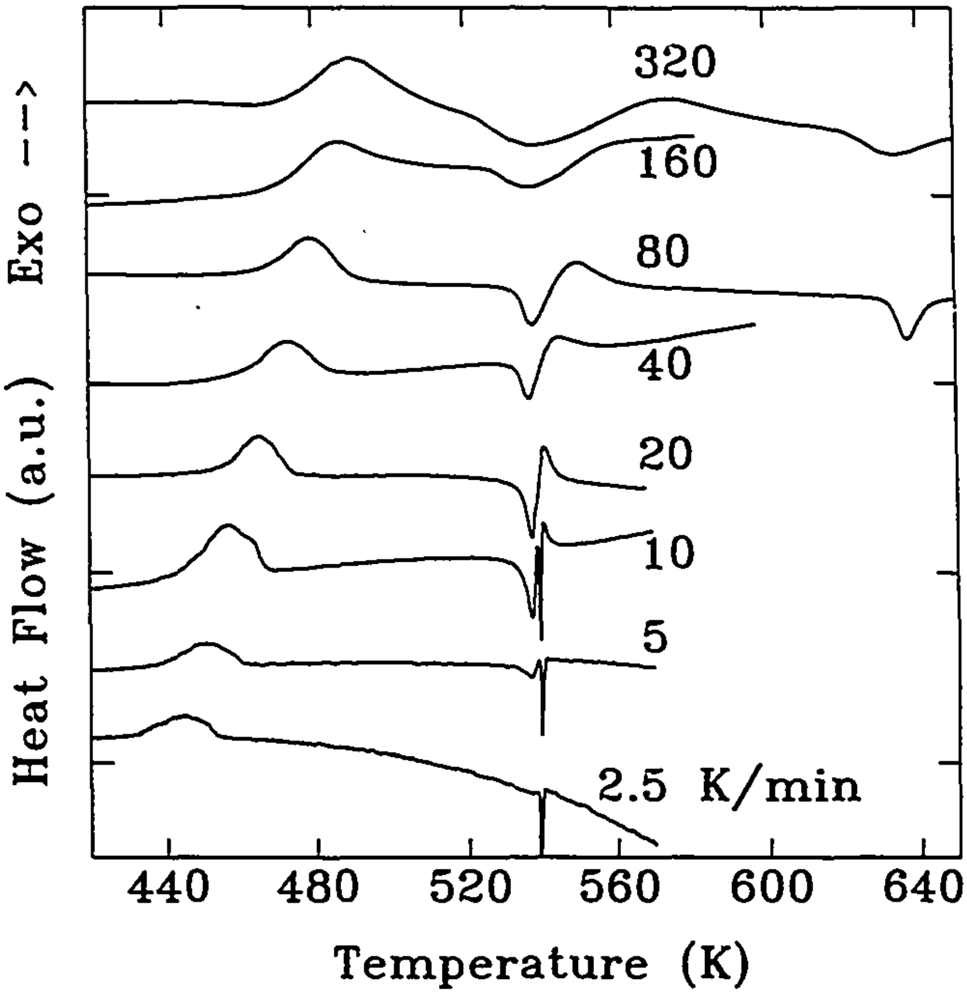

Figure 5.1: DSC scans of MnBi ribbons at different heating rates

hkl	d (nm)		intensity(a.u)	
	exp.	cal.	exp.	cal.
401	0.3121	0.31144	100	100
600	0.2885	0.28824	19	12
520	0.2763	0.27693	4	1
241	0.2641	0.26424	30	50
440	0.2498	0.24962	21	19
431	0.2411	0.24021	20	5
102	0.2222	0.22263	44	2
202	a	0.21730		14
701, 351	a	0.21646		7
621	0.2108	0.21154	11	19

Table 5.1: The x-ray diffraction data of Mn_3Bi from calculation and experiment. Calculation is based on the data in Table2.1 and on Equ. 3.4. The label a in d indicates overlap with peaks of NP .

5.1 Crystallization

5.1.1 Experimental results

The first exotherm in Fig. 5.1, between 440 K and 480 K (depending on heating rate), corresponds to crystallization. The products of the crystallization are principally Bi, Mn_3Bi, and NP, though evidence for small amounts of α-Mn, β-Mn and $MnBi_2$ are also seen. The x-ray diffraction scan, taken at room temperature, after heating the sample to the first exotherm is shown in Fig. 5.2(a). Tables 5.1 and 5.2 show that the x-ray pattern of Mn_3Bi agrees with Yoshida's observation(Yoshida, Yamada and Furukawa, 1968) within 0.35% of atomic spacings, and NP agrees with Guillaud's result(Guillaud, 1951b) within 0.86%. A sample has been examined in a pulsed field of 18 T at 300 and 100 K, and none of the phases exhibits the large magnetic moment characteristic of ferromagnetic or ferrimagnetic order.

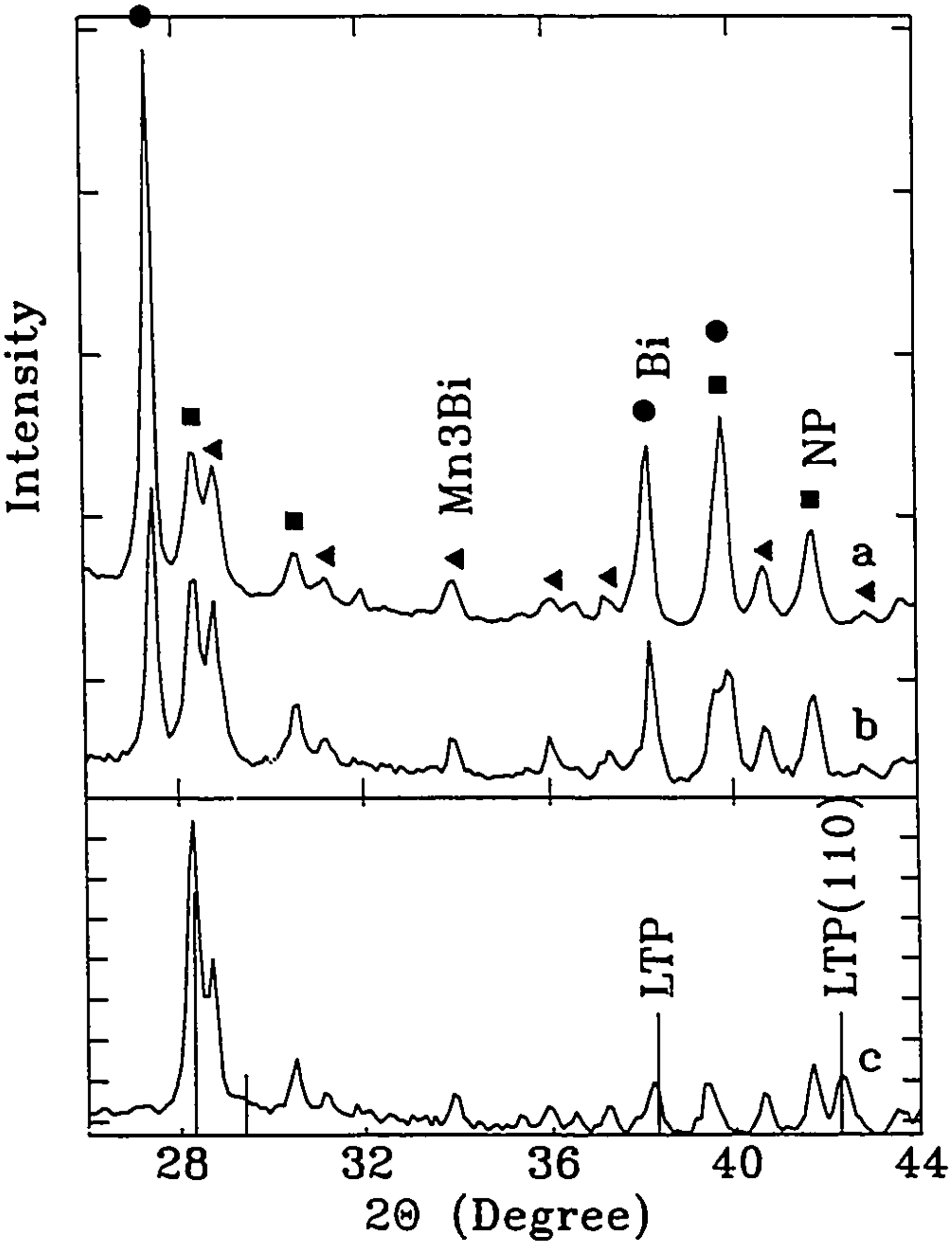

Figure 5.2: (a) X-ray diffraction pattern, taken at room temperature, for a sample heated to 500 K at 80 K/min and cooled down to room temperature at 320 K/min. (b) X-ray diffraction pattern taken at 400 K after a 2-hrs anneal at 400 K. (c) X-ray diffraction pattern taken at 543 K, showing the peaks of Bi disappear as a result of melting, and LTP grows.

hkl	d (nm)		intensity(a.u)	
	exp.	cal.	exp.	cal.
001	0.554	0.58300	4	< 1
100	a	0.37412		5
101	0.316	0.31487	100	100
002	0.294	0.29150	39	9
102	ab	0.22994		34
110	0.2166	0.21600	66	37
003	0.1937	0.19433	2	< 1
201	0.1787	0.17812	12	18
112	b	0.17355		11
103	0.1728	0.17246	19	16
202	0.1570	0.15743	19	9
004		0.14575		3
210	0.1414	0.14141	6	< 1
211		0.13742		1
104	0.1361	0.13581	6	< 1
203	0.1344	0.13477	3	< 1

Table 5.2: The x-ray diffraction data of NP from calculation and experiment. Calculation is based on the data in Table2.1 and Eqn. 3.4. The labels a and b in d indicate overlap with peaks of Bi and Mn_3Bi respectively.

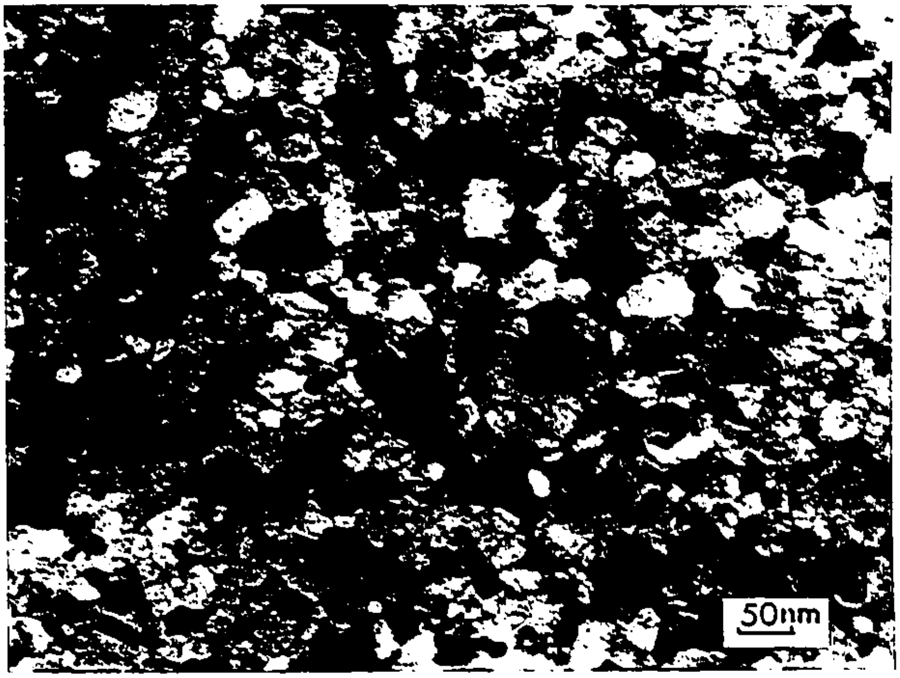

Figure 5.3: Electron micrograph of a ribbon crystallized *in situ* in the electron beam.

The same transformation is seen by TEM, where the sample is crystallized in situ through heating by the electron beam. The resulting micrograph shows a mosaic of small crystals about 10-50 nm in size [Fig.5.3]. Figure 5.4 shows the corresponding electron diffraction pattern.

The transformation may also be effected by isothermal annealing even at temperature as low as 40 K below the exotherm, producing the same mix of phases [see Fig.5.2(b)]. Since crystallization of amorphous metals have been observed to occur generally by nucleation and growth processes (Köster and Herold, 1981), the crystallized fraction $x(t)$ of the isothermal annealing can be described by the Johnson-Mehl-Avrami (1939; 1940; 1941) equation

$$x(t) = 1 - exp[-(K_T t)^n] \tag{5.1}$$

where the constant n is the Avrami exponent whose value depends on the nucleation rate and the type of growth process. The exponent n can be determined by the slope of the plot of $ln\ ln(1/(1-x))$ versus $ln(t)$. After normalization, the enthalpy released as a function of time can be scaled to $x(t)$. Isothermal crystallization in the DSC can

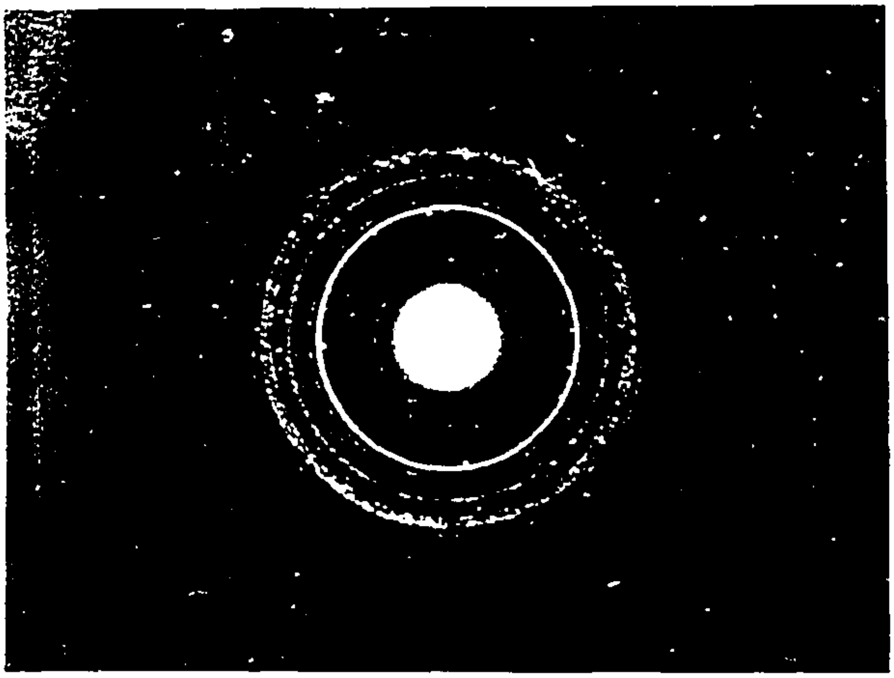

Figure 5.4: Electron diffraction pattern of a ribbon crystallized *in situ* in the electron beam.

thus be used to calculate the exponent n and to determine the kinetic mechanisms of the crystallization.

Several factors affect the result of an isothermal scan. The first factor is the sample mass. A large signal needs a large sample. On the other hand, too much sample decreases the thermal conduction between sample and the sample holder, and so distorts the real isothermal signal. So a proper choice of sample mass is important. The second factor is the heating rate that brings the sample to the temperature for isothermal scan. There is an unwanted transient signal when the DSC instrument transforms from heating a sample to keeping the sample at a certain temperature. The transient signal is proportional to the heating rate. An isothermal measurement needs to bring the sample to the required temperature as soon as possible, while keeping the transition signal as small as posible. For this purpose, we divided the heating into two steps, with the first having a higher heating rate and the second a lower. The third factor is the isothermal temperature. The higher the temperature, the higher the signal, since the transformation rate is then faster. However, too

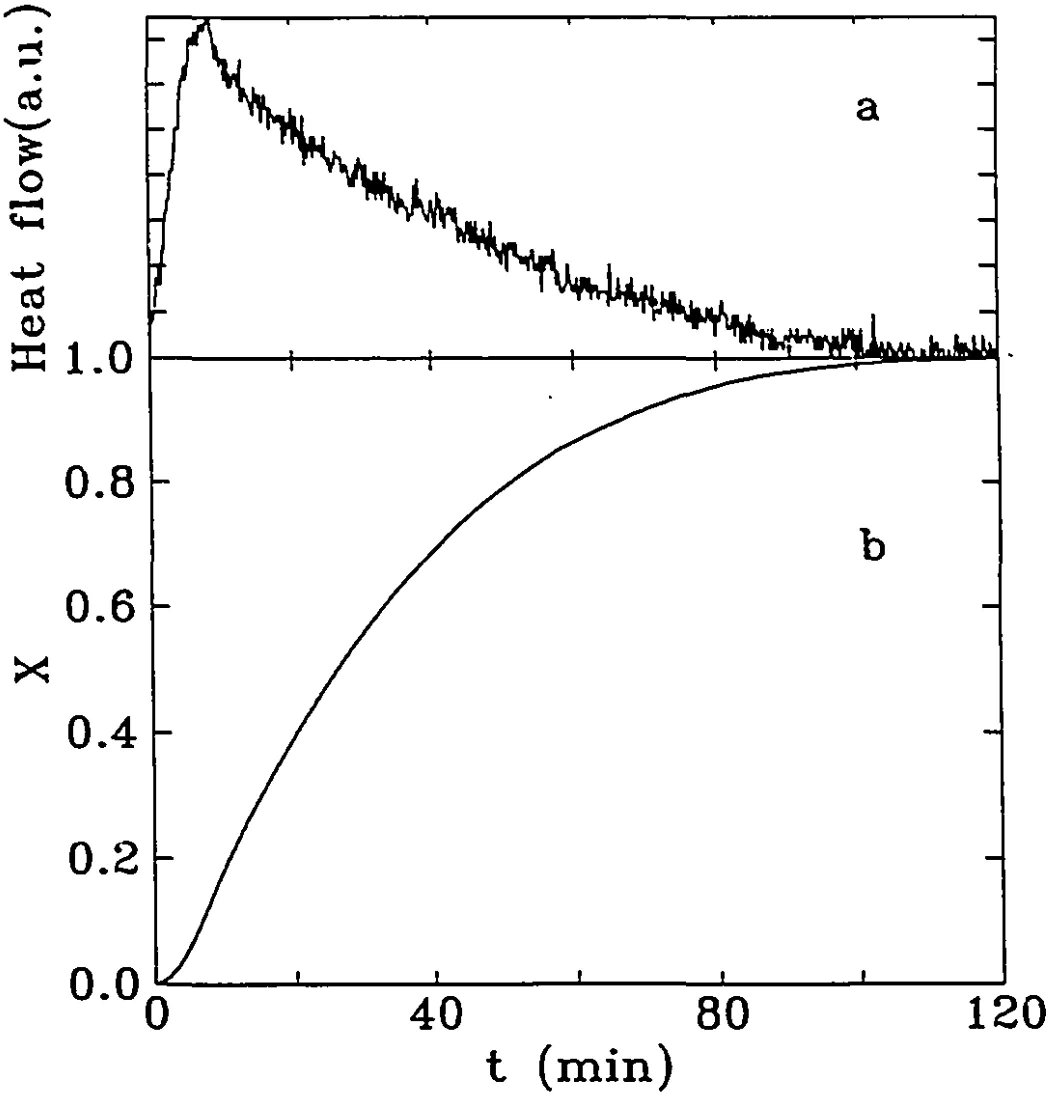

Figure 5.5: (a) The isothermal DSC data of as-made ribbons at 405 K. (b) The enthalpy released till time t, integrated from plot (a) and normalized to one, to show the fraction of crystallization.

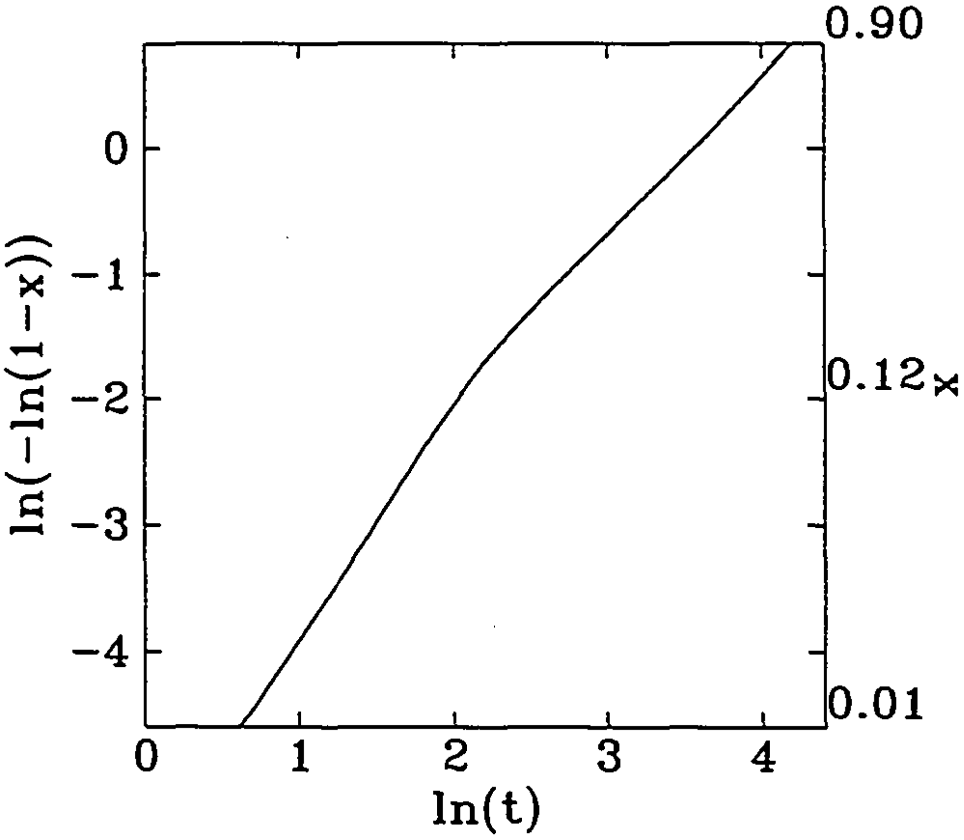

Figure 5.6: Avrami plot for the crystallized fraction x between 0.01 and 0.9.

high a temperature gives an incubation time (the time lag needed for a measurable amount of transformed fraction to occur) too short to be handled in the experiment. So a proper choice of the temperature is important to get a significant signal and a manageable incubation time.

Isothermal crystallization was carred out as follows: about 16 mg of sample is heated to 370 K from room temperature at a rate of 20 K/min, and further heated to 405 K at 5 K/min. The sample was allowed to equilibrate for 30 seconds at 405 K, after which the DSC begins to record the heat flow into or out of the sample. After all transformations are completed , the sample is scanned again using the same procedure, to obtain the background. Fig. 5.5(a) shows the isothermal crystallization of amorphous MnBi. The total heat released during the 120 minutes of annealing is 5.7±0.3 kJ/mol, the same enthalpy change (within error) measured in an isochronal DSC scan at a heating rate of 5 K/min (Fig. 5.1). Fig. 5.5(b) shows the crystallized fraction of the sample calculated from the heat flow of the isothermal transformation. Fig. 5.6 gives the Avrami plot that produces an exponent $n = 1.9$ for the crystallized fraction in the range $x = 0.01$ to 0.12 and $n = 1.3$ for $x = 0.12$ to 0.9.

Though the enthalpy change is the same as that of the isochronal DSC scan, uncertainty in incubation time may lead to an error in n (Mao and Altounian, 1991). The uncertainty in the incubation time in this experiment is about 30 seconds, the time used to let the sample reach a uniform temperature. The error of the origin of the time axis t_0, or the choosing of incubation time affects the exponent n by (Mao and Altounian, 1991)

$$\Delta(\frac{1}{n}) = \frac{d}{dt_0}[\frac{ln(t_2 - t_0) - ln(t_1 - t_0)}{ln(-ln(1 - x_2)) - ln(-ln(1 - x_1))}]\Delta t_0 \tag{5.2}$$

$$\Delta n = -n^2 \Delta(\frac{1}{n}) \tag{5.3}$$

In Eqn. 5.2 the sign of the error in n is determined by the sign of Δt_0; if the sign of Δt_0 is definite, the error will shift towards only one direction. This is the case in the present occasion. From Fig. 5.5(a), we can see that the peak rises rapidly at the very beginning so the origin of the time axis cannot be taken any later (in fact, the transformation may already have begun). The errors, Δn, thus calculated, for $t_0 = 0$ and $\Delta t_0 = +30$ seconds, are negative, and are 0.5 and 0.1 for n of 1.9 and 1.6 respectively. We thus get $n = 1.9^{+0.5}$ for the first stage of crystallization, and $n = 1.3^{+0.1}$ for the second stage.

The crystallization through nucleation and growth is a thermally activated transformation. The temperature dependence of Equ. 5.1 is reflected in K_T, the K_T is a function of temperature. Assuming an Arrhenius behaviour (Henderson, 1979)

$$K_T = K_0 exp(-E/k_B T) \tag{5.4}$$

the activation energy E can be obtained by Kissinger's method (Kissinger, 1957; Henderson, 1979). We can see from Fig. 5.1 that the peak positions, T_p of the crystallization exotherm depend strongly on the heating rate Φ. The plot $ln(\Phi/T_p^2)$ verse $1/T_p$, the Kissinger's plot, will give an approximate straight line that has a slope of $-E/k_B$ (Henderson, 1979). Fig. 5.7 shows the Kissinger's plot for MnBi that gives an activation energy E of 1.7 eV for the crystallization. The crystallization is then characterized by the crystallization temperature T_x between 440 and 480 K, the enthalpy change of 5.7 kJ/mol, and its nucleation and growth process with an activation energy of 1.7 eV and an overall Avrami exponent around 1.8.

5.1.2 Discussion

First, it is interesting to notice that the crystallized state has many phases. From Fig. 4.6, we see that the crystallized phases can appear over a finite composition range below the crystallization temperature. According to the Gibbs' phase rule (Landau and Lifshitz, 1980), a system with two thermodynamic degrees of freedom–the temperature and composition, and two independent components–Mn and Bi, cannot have more than two phases in equilibrium. The coexistence of more than three phases is, therefore, obvious evidence that the crystallized MnBi ribbons are in a non-equilibrium state.

Second, the kinetics of the crystallization can also provide information about the

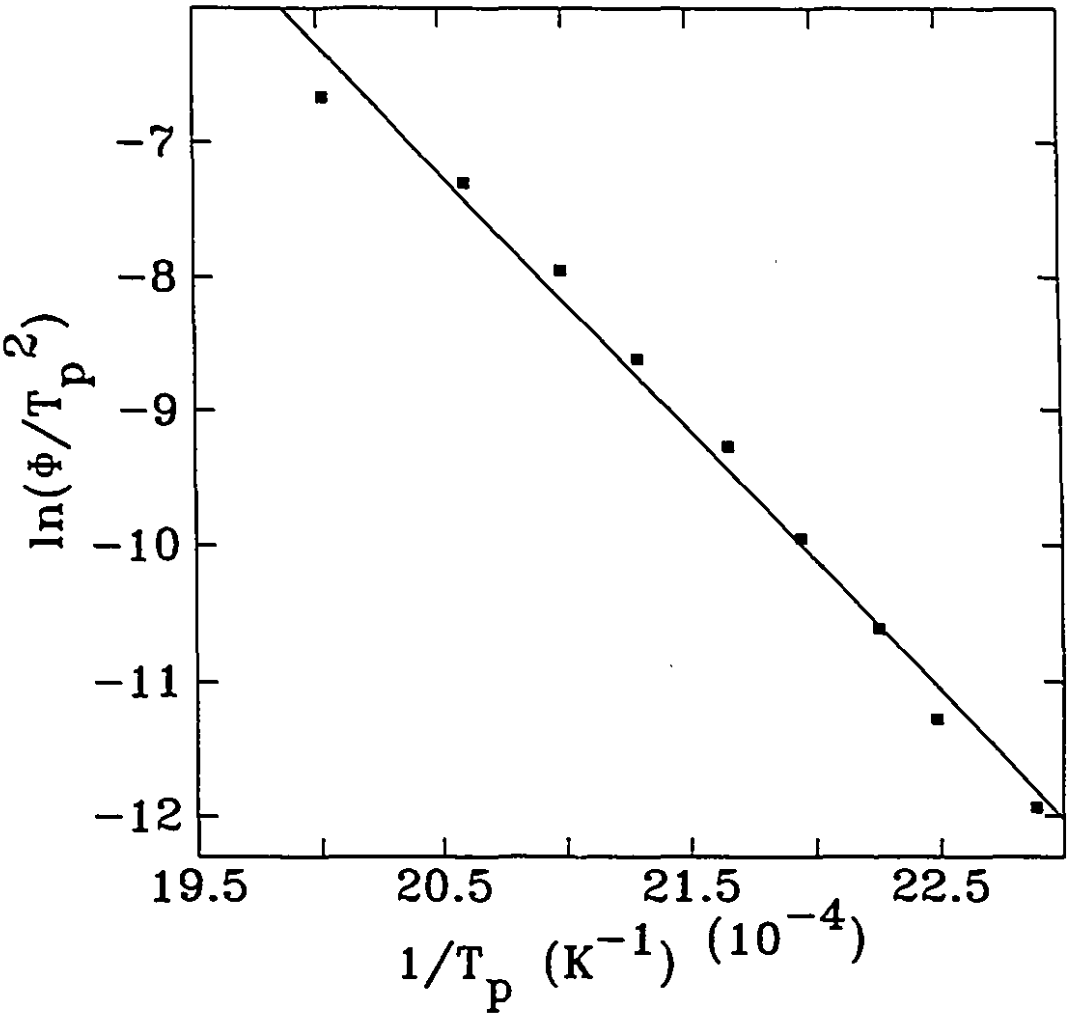

Figure 5.7: Kissinger plot of the crystallization of amorphous MnBi, with heating rate Φ from 1.25 to 320 K/min. T_p is the position of the exothermal peak.

as-spun MnBi.

Christian (Christian, 1965) concluded that the transformation of diffusion controlled growth has $1.5 < n < 2.5$ when nucleation rate is decreasing, and $1 < n < 1.5$ when growth is from appreciable initial volume with zero nucleation rate. The observed initial exponent of $n = 1.9^{+0.5}$ excludes the possibility of grain growth of particles of appreciable initial volume at beginning. In addition for coarsening of grains, in isothermal calorimetry, the signal decreases monotonically (Chen and Spaepen, 1991) instead of forming a peak. We conclude from the study of crystallization, therefore, that the as-made MnBi ribbons are amorphous and the crystallization is a diffusion controlled process.

If the as-spun MnBi is a uniform amorphous phase, and diffusion is the main barrier, the crystallization is expected to be polymorphous (the transformation between structures of the same composition), because it needs no change in concentration and needs the least diffusion. (See the dashed line and process 1 in Fig. 5.8.) This will result in a direct transformation from amorphous to crystalline MnBi, in contrast to some of the crystallized phases that are detected, such as Bi and Mn_3Bi. One possible explanation is that the amorphous MnBi may be phase separated. This separation tendency can also be seen from the immiscibility of the liquid state in the equilibrium phase diagram Fig. 2.1. If as-made ribbons are in phase separated states, the evolution of a multi-phase state can be explained from Fig. 5.8.

In summary, the kinetic analysis of the crystallization confirms that the as-spun MnBi is amorphous. The amorphous state may be inhomogeneous in concentration, or phase separated. The crystallization, occurring between 440 and 480 K, is a diffusion controlled process that has an activation energy of 1.7 eV and releases 5.7 kJ/mol heat. The result is a multi-phase state that contains mainly Bi, Mn_3Bi and NP. Though the first crystallized state is more stable than the as-spun MnBi, it is not in equilibrium.

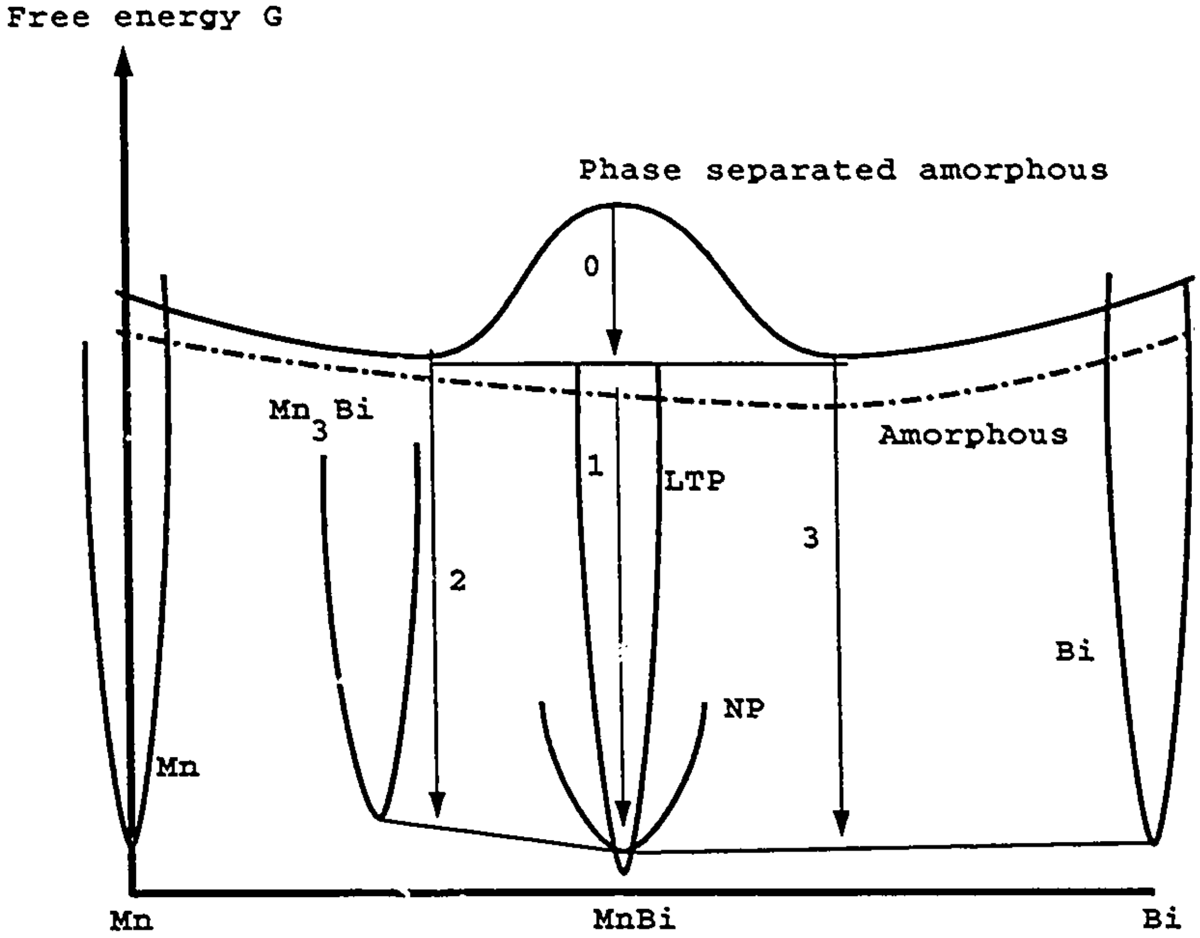

Figure 5.8: Hypothetical diagram of free energy versus composition near room temperature. Process 0: phase separation; Process 1: polymorphous transformation; Process 2 and 3: eutectoid transformations.

5.2 The formation of LTP

Since the first crystallized state is not in equilibrium, it is expected to transform to an equilibrium state upon further heating. From the DSC thermograms in Fig. 5.1, we can see that after the first crystallization (the first exotherm in DSC), there is an endotherm–at low heating rate, two endotherms–close to 540 K, followed by a second exotherm. The endotherms at 536 K and 539 K (seen most clearly at 10 K/min heating rate), correspond to melting of the Bi-rich eutectic and Bi(Mn), respectively, as indicated by the temperatures of those events in the phase diagram (Fig. 2.1). This interpretation is confirmed by high temperature x-ray diffraction results. At a temperature just above the two endotherms, the crystalline Bi peaks disappear while other peaks still can be seen in addition to newly grown LTP [Fig. 5.2 (c)]. Immediately after (or even during) the melting of Bi, the exotherm corresponding to the formation of LTP appears, as shown in Fig. 5.1. Fig. 5.9(a), an x-ray diffraction pattern taken at 543 K, shows a completed transformation of the multi-phase state to LTP: Mn_3Bi and NP have disappeared and almost pure LTP is seen, with a small amount of liquid Bi. The corresponding room temperature x-ray diffraction pattern is shown in Fig. 5.10. A DSC scan of the sample cooling down from 600 K to room temperature shows a small exothermic peak owing to the freezing of the residual Bi. The enthalpy of this peak correspond to about 5 wt.% of the unreacted Bi. The area ratio of the Bi (102) peak to LTP (101) peak in Fig. 5.10 is 7%. Assuming the peak ratio can represent the weight ratio, this result is very close to that from the enthalpy.

As a ferromagnetic phase, LTP is magnetically distinguishable from the amorphous phase and from the mix of phases just after crystallization. This makes thermomagnetometry a powerful tool to detect the transformation of LTP. Fig. 5.11 shows the magnetization of MnBi ribbons as a function of temperature at different heating rates. The magnetization indeed increases rapidly around 540 K, confirming the formation of LTP. At heating rates higher than 10 K/min, the reaction needs a wider range of temperature. This agrees with the DSC scans (Fig. 5.1) where higher heat-

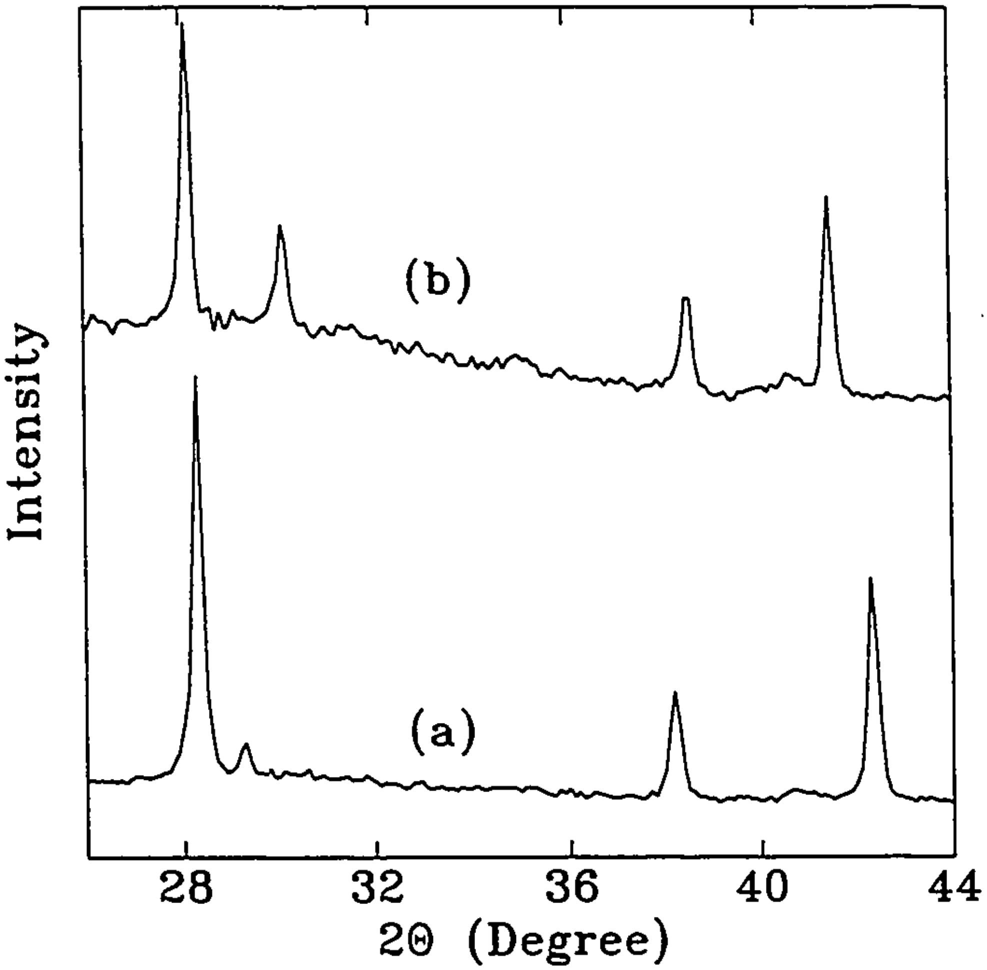

Figure 5.9: High temperature x-ray diffraction pattern of (a) LTP taken at 453 K and (b) HTP taken at 650 K.

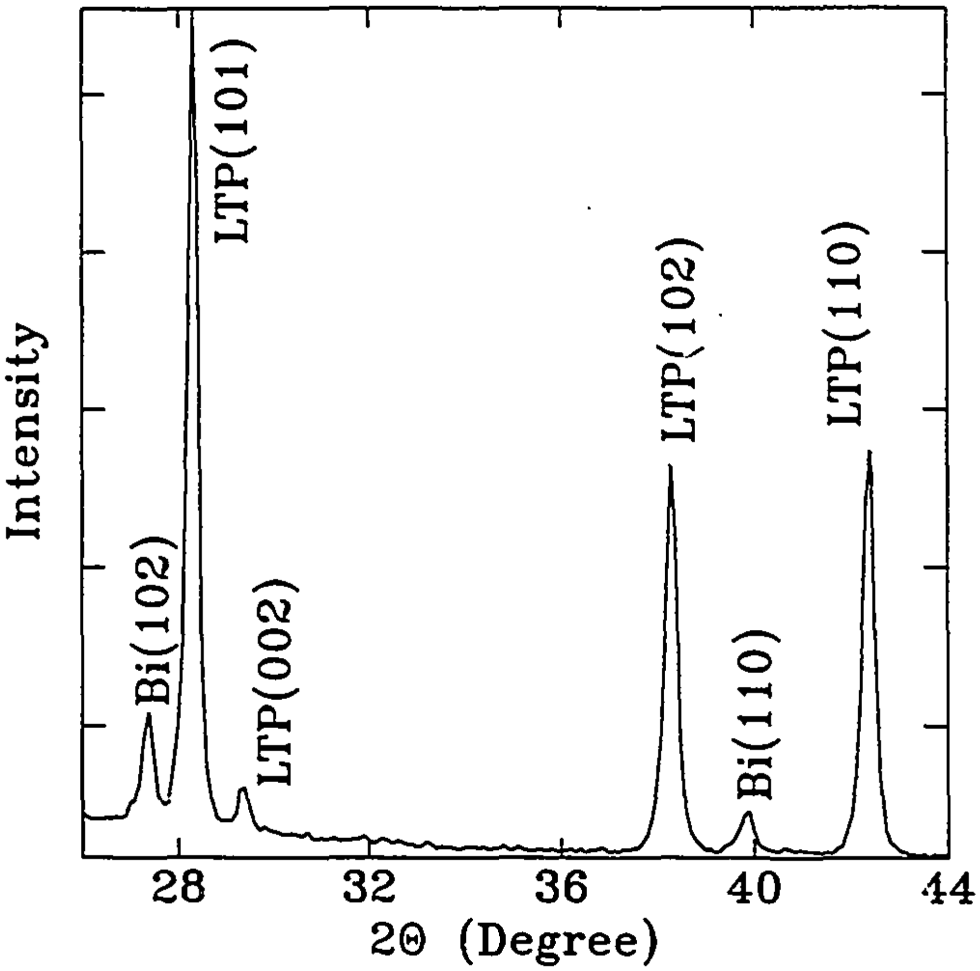

Figure 5.10: Room temperature x-ray diffraction pattern of LTP. Sample was heated to 600 K at 80 K/min, then cooled down to room temperature at 320 K/min.

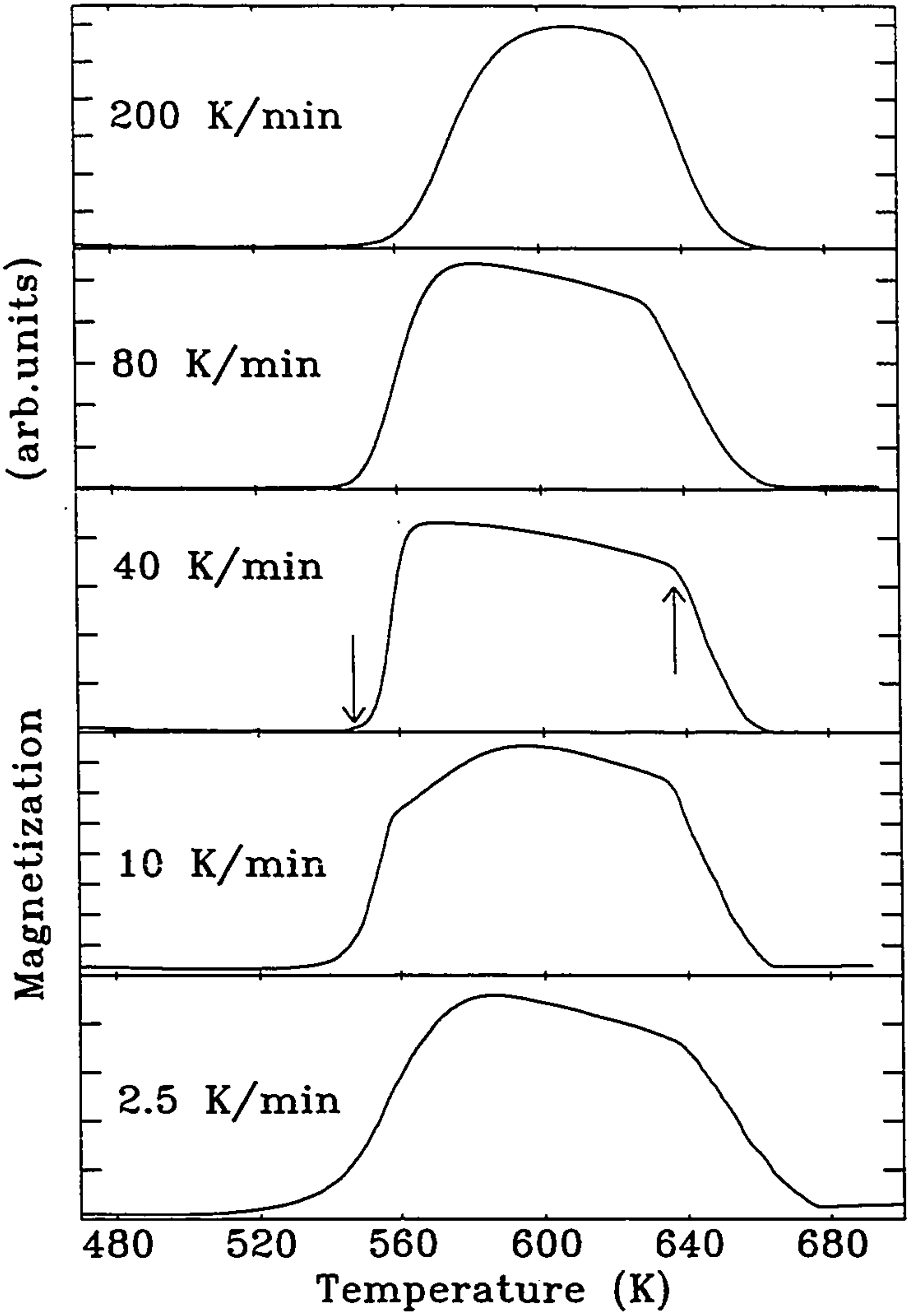

Figure 5.11: TGA scans of as-spun MnBi at different heating rates. In 40 K/min scan, the down and up arrows mark the starts of forming LTP and transforming LTP to HTP, respectively.

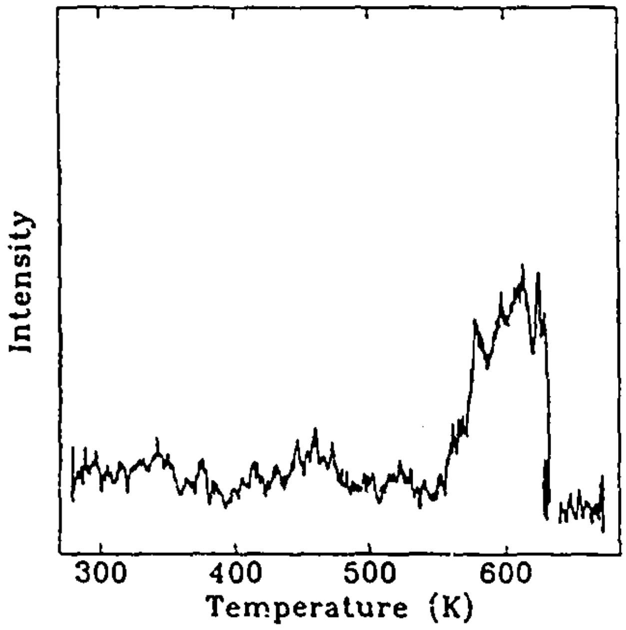

Figure 5.12: Intensity of the LTP (110) Bragg peak as a function of temperature at a heating rate of 200 K/min

ing rates increase the separation of the exotherm from the endotherm. At heating rate of 2.5 K/min, about 10 % of LTP is already formed below 540 K (assuming the magnetization to be proportional to the amount of LTP.) Though a small amount of LTP can be formed below the melting temperature of Bi, the reaction is strongly accelerated at the melt.

The enhancement of the reaction upon melting of Bi is dramatically shown in Fig. 5.12, where the intensity of the x-ray diffraction of LTP (110) peak at $2\Theta = 43^\circ$ is plotted as a function of temperature. This line does not overlap with any diffraction lines of the other Mn-Bi phases, as shown in Fig. 5.2, and so offers a unique signature of the LTP phase. The intensity increases abruptly about 540 K (for a heating rate of 200 K/min), saturates at 600 K, and then disappears about 630 K with the transformation to HTP. The feature of the peak agrees well with the TGA scan of 200 K/min (Fig. 5.11).

Being stimulated by the melting of the Bi-rich eutectic, the reaction of the multiphase to LTP is more-or-less like the reaction of solid-liquid to solid. Compared to equilibrium solidification (where MnBi liquid is first segregated to Mn and liquid then forms HTP through peritectic reaction), however, this transformation has much less segregation (NP has the same composition as LTP, and Mn_3Bi is closer in composition to LTP than Mn is). Rapid quenching has suppressed segregation, and so makes the final reaction to single MnBi phase more effective.

5.3 Transformation of LTP to HTP

The transformation of LTP to HTP at 628 K (see Fig. 2.1) is complicated. At the transition, the composition changes by 8% even though the crystal symmetry remains the same (see Table 2.1 and reference (Chen and Stutius, 1974)). The c/a ratio of the lattice parameters decreases by 4.2% though the volume remains almost unchanged (Roberts, 1956). Furthermore, the transition involves a change in magnetic order and is thermally hysteretic – the transition occurs, for single crystals, at 628 K upon heating and at 613 K upon cooling.

The last endotherm of the DSC scans (Fig. 5.1) is the LTP-HTP transformation. This is confirmed by x-ray diffraction at 650 K that shows a clear HTP pattern (see Fig. 5.9(b)). From Fig. 5.11, we can also see the abrupt drop of the magnetisation around 640 K. The TGA scan of a sample, heated above the transformation temperature and water quenched to room temperature, (Fig. 5.13) shows a Curie point of 450 K, in agreement with the reported value of QHTP (Chen and Stutius, 1974), and with the value extrapolated from the susceptibility of HTP according to the Curie-Weiss law (Heikes, 1955). The enthalpy of the endotherm for the transformation, measured by DSC, is about 2.4 kJ/mol.

Fig. 5.14 is a TGA scan including the cooling curve. The offset base line after the transformation does not disappear even after the magnetic field is removed. Therefore, there has been an increase in sample weight, presumably because of oxidation. This means that MnBi has partially decomposed and cannot be recovered: there is some Mn oxide and pure Bi in the sample. The partial decomposition can also

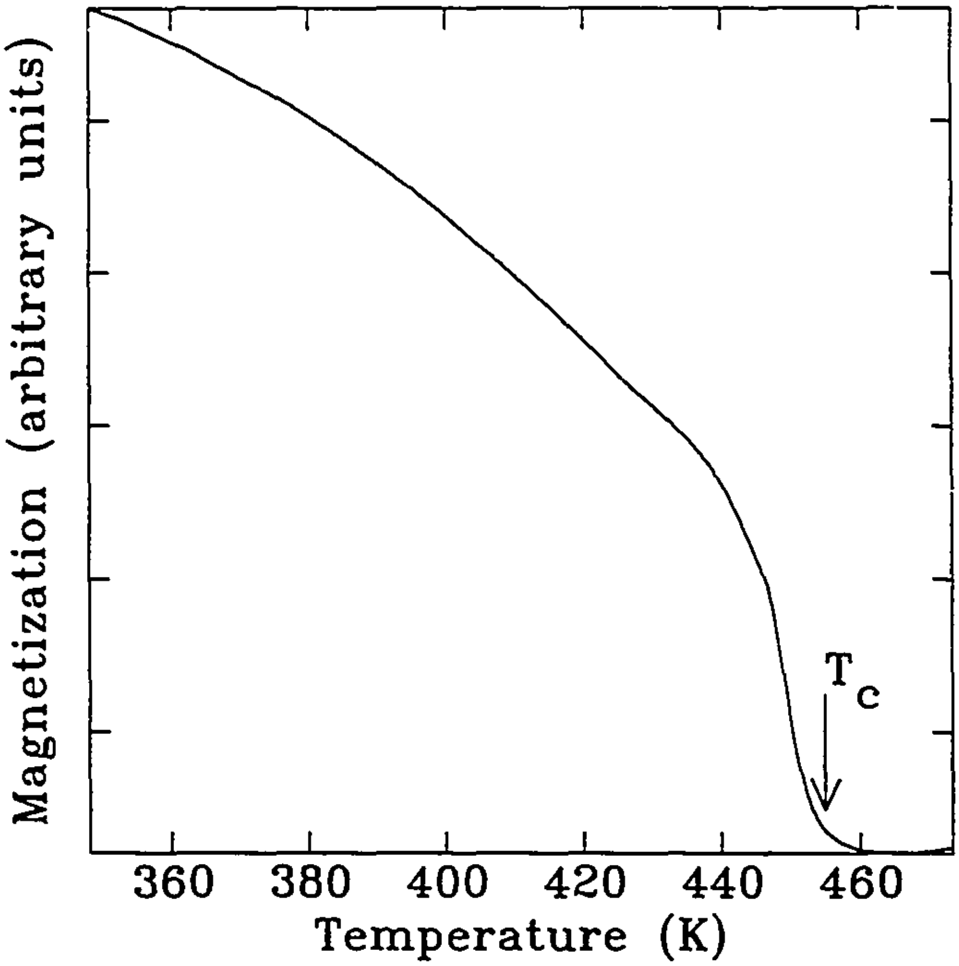

Figure 5.13: TGA scan of QHTP, at a heating rate of 80 K/min. The magnetic transition is clearly seen at 450 K.

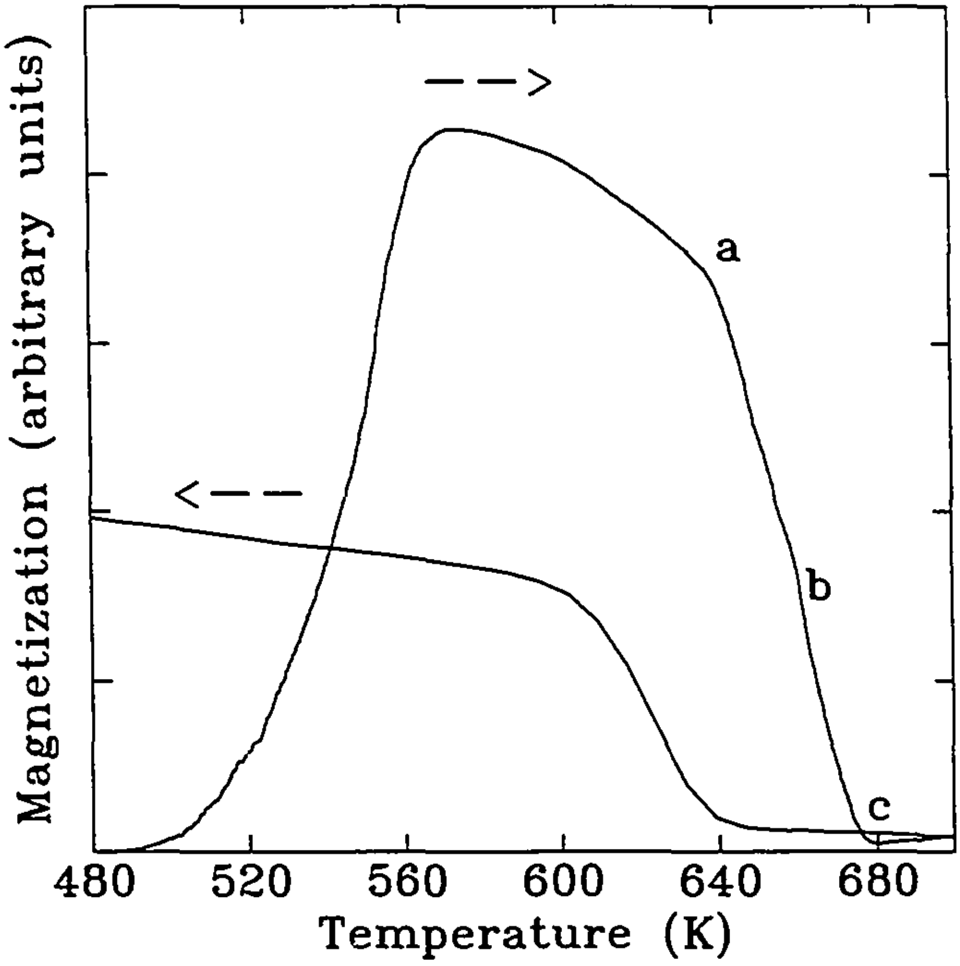

Figure 5.14: A TGA scan of as-spun MnBi at rate of 1 K/min, the arrows give the heating and cooling directions. a, b and c indicate the beginning, at maximum rate and end of the transformation of LTP to HTP.

be seen in the DSC scan. A sample is heated to 700 K at 10 K/min, then cooled at the same rate. The enthalpy change corresponding to condensation of Bi during cooling increased 100% than that heated only to 570 K, indicating increased Bi after LTP-HTP transformation. The partial decomposition of MnBi is the reason why the magnetisation does not recover its original magnitude after the sample is cooled far below the transition temperature. Nevertheless, the thermal hysteresis is clearly seen: upon heating, the magnetic transition begins at 641 K, and ends at 677 K; upon cooling, it begins at 639 K and ends at 605 K. The magnetic transition regions, both for heating and cooling, cover a span of temperatures of about 35 K. This transition region agrees with those observed by x-ray (Haudek and Unger, 1971) and neutron diffraction (Roberts, 1956; Andresen *et al.*, 1967), where the intensities of diffraction peaks are plotted versus temperature. If we rescale the magnetization to the original magnitude in LTP, the heating and cooling transitions become parallel slopes with displacement of about 40 K, which look more similar to the x-ray and neutron diffraction data. The thermal hysteresis displacement, however, is not consistent: it is 40 K here, about 30 K in Roberts (1956), less than 20 K in Andresen et al.(1967), and larger than 90 K in Haudek and Unger (1971). This may be because of different stress state between the samples, as we will see below.

The range of the magnetic transition is almost independent of heating rates, as can be seen from Fig. 5.11. Fig. 5.15 plots the temperatures at the beginning, maximum rate, and end of the magnetization change versus the heating rates (see also Fig. 5.14). If we divide the temperature ranges, from the beginning to the end of the transition, by the heating rate, we obtain the time for the transition. For 1 K/min the transition time is 2130 s, which is two orders of magnitude larger than the result for a heating rate of 200 K/min. Comparing with the DSC results, where the times of the transition that involves enthalpy change are constantly around 10 s regardless of heating rates (the same kind of calculation from Fig. 5.15), it is clear that DSC and TGA detect two different processes. In fact, for heating rates smaller than 40 K/min, we can see that the magnetic transition starts only after the end of the enthalpy change. The

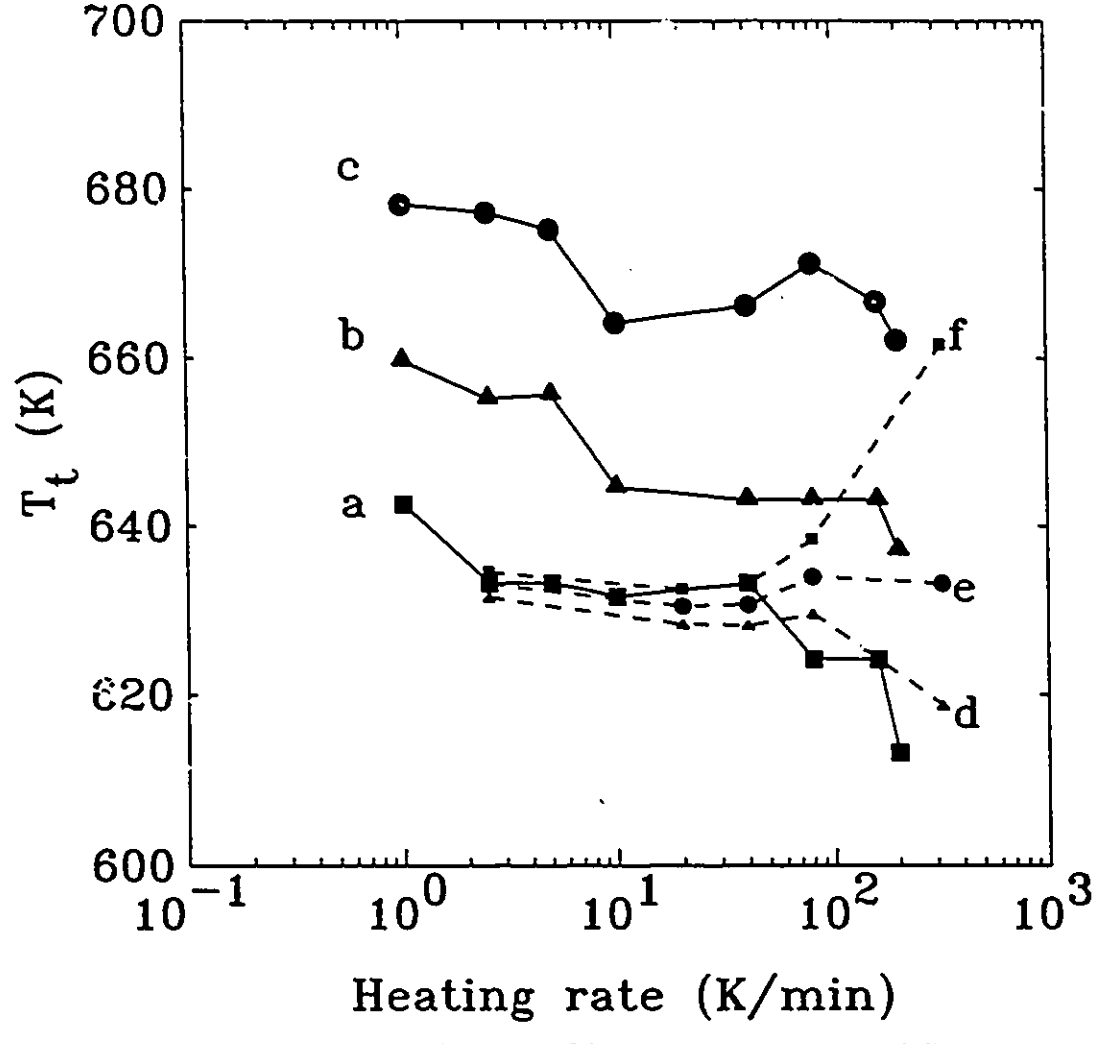

Figure 5.15: The TGA(solid lines) and DSC(dashed lines) data at different heating rates. (a, b, c) are the temperatures of begins, at highest rates, and ends of magnetic transition respectively. (d, e, f) are onset, maxima and ends of endotherm peak.

different time scales of the two processes enable us to calculate the enthalpy change of the DSC peak. Neglecting the entropy change caused by the magnetic transition, the enthalpy change detected by the DSC can be estimated from the entropy change because of Bi melting and the increase of Mn interstitials in HTP.

From Fig. 2.1 and the mass conservation law, the MnBi at 628 K will decompose to 91.7% of $Mn_{1.08}Bi$ and 8.3% of liquid $Bi_{90}Mn_{10}$. The latent heat of fusion, ΔH, of Bi is 13 cal/gram at 544 K, or 14 kJ per mole of MnBi. Assuming ΔS is the same for Bi melting at different temperatures and $\Delta S = \Delta H/T$, the enthalpy change for Bi melting at 630 K is then $14 \times 630/544 = 16.6$ kJ/mol. For 8% Bi, this results in a 1.33 kJ/mol enthalpy change.

The $Mn_{1.08}Bi$ has the same structure as LTP except for the 8% of interstitials of Mn atoms (Chen and Stutius, 1974; Andresen *et al.*, 1967). For every MnBi molecule, there is one interstitial site available (see Fig. 2.2). For N MnBi molecules and $n = 0.08N$ interstitials, the entropy can be calculated as $k_B ln(N!/(N-n)!n!)$. The result is 1.29 kJ/mol. Together with 1.33 kJ/mol from Bi melting, the total enthalpy change is about 2.6 kJ/mol, which agrees well with the experimental result of 2.4 kJ/mol.

The LTP to HTP transformation can therefore be explained as follows. At a temperature of 630 K, LTP decomposes into Bi-rich liquid and $Mn_{1.08}Bi$. This process takes about 10 s , as observed by DSC. The $Mn_{1.08}Bi$ is still in the LTP, i.e. LTP with interstitials but no change in lattice parameters. This assumption is consistent with the x-ray and neutron diffraction results. Furthermore, magnetic properties are closely related to interatomic distances, which explains why in Fig. 5.15 the magnetization has not changed–for the low heating rates–after the endothermic DSC peak. In the next stage, the LTP of $Mn_{1.08}Bi$ transforms to HTP. The transformation is martensitic: it involves no compositional changes or diffusion, but deformation, and the transformed fraction strongly depends on temperature but not on time (Christian, 1965).

Fig. 5.15 shows also that the temperature of the magnetic transition tends to decrease with increasing heating rates, while the peak positions of the endotherm remain unchanged. This may be the result of stress that produce deformation energy. The c/a ratio of LTP has a positive temperature coefficient of $22.5 \times 10^{-6}\ K^{-1}$ (Roberts, 1956). When heating rate is high, the increase in c/a ratio creates a stress in the polycrystalline sample that favours the HTP whose c/a ratio is 4% smaller than LTP. For low heating rates, the stress may not accumulate because of relaxation. This phenomenon has been observed in MnBi thin films (Haudek and Unger, 1971) where a stress opposite to the present case increases the transformation temperature.

The heating rate dependence of the magneto-structural transition and the independence of the compositional transition suggest that the two process may not be strongly correlated. This can also be demonstrated from the thermal hysteresis for both processes. Two MnBi samples were cooled from 700 K in the DSC at a rate of 40 and 20 K/min respectively. The exothermal peaks corresponding to the transition are at 629 and 628 K respectively, whereas the heating scans give a peak at 633 K (see Fig. 5.15). This hysteresis of 5 K is much smaller than 40 K, the hysteresis of the magneto-structural transition.

In summary, the LTP-HTP transformation has two experimentally distinguishable processes: the compositional transition and the magneto-structural transition. The compositional transition has a transition temperature which is independent of the heating rate and shows a small thermal hysteresis. The magneto- structural transition is very similar to a martensitic transition. It is thermally hysteretic, affected by stress and heating rate, and the amount transformed depends strongly on temperature.

Part II

Magnetic properties of the low temperature phase of MnBi

Chapter 6

Theory and technique of magnetic measurements

One of the most unusual properties of LTP is its magnetic anisotropy: it is not only very high, but also increases with temperature. Indeed, the anisotropy of LTP is so high above room temperature, that the only reported result covering high temperature region comes from extrapolation of a low field measurement (Stutius, Chen and Sandin, 1973). In the present work, we used high magnetic field produced by a pulse magnet, in combination with the so-called singular point detection technique (SPD), to measure the anisotropy field directly. Typically, pulsed fields have a lower homogeneity than static fields, because eddy currents are generated which alter the field distribution; also the coil producing the field undergoes elastic deformation due to the Lorentz force. To extract a reproducible signal from a sample in such a field lasting so short a time, and to combine it with the SPD technique is one of the achievements of the present research.

6.1 Magnetic properties and magnetic hysteresis

In the present work, we measured three magnetic properties of LTP: saturation magnetization M_s, anisotropy field H_a, and coercivity H_c.

Saturation magnetization M_s is an intrinsic property of ferromagnetic materials. It is the maximum magnetic dipole that can be produced per unit volume of the sample, and is the result of alignment of magnetic moments inside the material. The magnetic moments are aligned below the Curie temperature T_c by the quantum mechanical exchange interaction and mis-aligned by the thermal agitation. From these two considerations and assuming the magnetic moments are localized, the temperature dependence of M_s can be described, for most materials, by spin wave approximation near 0 K, by scaling theory near T_c and classical molecular field approximation in the middle range. For 3d-transition metals and their alloys, the magnetic moments come from 3d electrons. There are two possibilities of the electron state: local or itinerant. For insulating metal oxides, the local electron state of a metal ion produces the local magnetic moment; for metallic materials, there are effective " atomic moments" as a result of averaging over fast quantum fluctuations of the itinerant electrons (Capellman, 1986). MnBi has an M_s at 0 K that corresponds to almost 4 μ_B per Mn atom. This suggests that the moment comes from the localized electrons of the Mn^{3+} ion. Stutius et al. (1975) adopted this view to explain transport phenomena and specific heat, assuming interstitial defects play an important role. However, Coehoorn and Groot (1985) calculated the band-structure of MnBi, suggesting a part of the d-electrons is delocalized. Their calculation also agrees with many experiments and gives an atomic moment of 3.7 μ_B. Although the material should show a spontaneous magnetization in the absence of a magnetic field, there is no macroscopic magnetisation without a field because of self demagnetization. The specimen splits into many small regional domains. In each domain the spontaneous magnetization takes such a direction that the over all sample shows no net magnetisation: this reduces the static magnetic energy. An external field can destroy the domain structure, forcibly aligning all the moments, and the technical saturation of the magnetization is a measurement, within error, to the spontaneous magnetisation M_s expected from theory.

The anisotropy field is another intrinsic property. It reflects the preference of the orientation of the local magnetization direction to a particular direction in the crystal lattice. The origin of the anisotropy arises from the coupling of the orbital degrees of freedom of electrons to the crystal lattice, so that the electron spin as well as the spontaneous magnetization can reflect the local symmetry through the spin-orbit interaction. As a consequence, the energy of the system changes with the magnetization direction, and this part of the energy is called the anisotropy energy. If this energy is expressed as a function of directional cosines, the form of the function is restricted by the lattice symmetry. When the anisotropy energy E_K is expanded in powers of directional cosines, the lowest three terms under the restriction of hexagonal crystal symmetry are (Zijlstra, 1967)

$$E_K = K_1 sin^2\theta + K_2 sin^4\theta + K_3 sin^6\theta + ... \tag{6.1}$$

where the K's are called the anisotropy constants, and θ is the angle between the direction of the magnetization and the direction of the c-axis of the crystal. Because of the anisotropy energy, the M_s of a domain feels a torque $-dE_K/d\theta$, that is attributed to an equivalent field, the anisotropy field H_a

$$H_a = -\frac{1}{M_s}\frac{d^2 E_K}{d\theta^2} \tag{6.2}$$

At $\theta = \pi/2$, $H_a = 2(K_1 + 2K_2 + 3K_3)/M_s$. Adachi (1961) calculated the anisotropy energy for materials of NiAs structure, assuming the electrons are in a localized ionic state. Though it agrees well with many materials, the calculation cannot explain the anisotropy of MnBi. On the other hand, the band-structure calculation (Coehoorn and de Groot, 1985) does not have enough numerical accuracy to describe the anisotropy. Despite of the lack of theoretical understanding, the anisotropy field is an important quantity to measure, for it helps to understand both the coercivity and the mechanism of the magnetisation process.

Coercivity, H_c, is an important technical property that indicates the magnetic hysteresis of a magnetization process, the higher the H_c, the larger the hysteresis. As a hard ferromagnetic material, MnBi displays magnetic hysteresis – i.e. its macroscopic magnetic state depends not only on external conditions but also on its magnetic

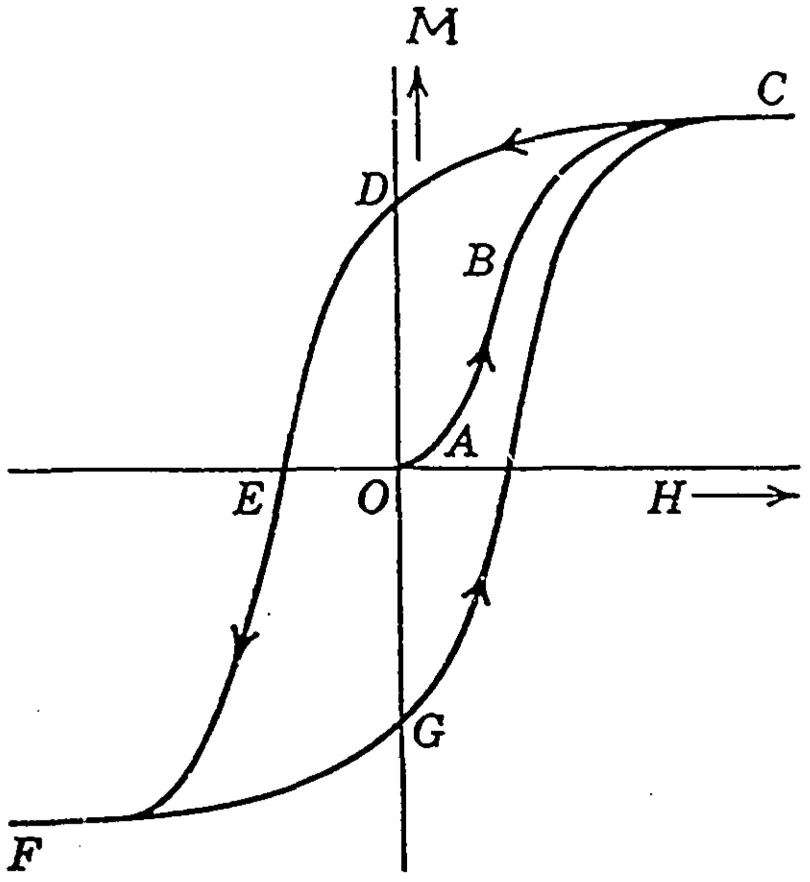

Figure 6.1: A magnetic hysteresis loop, after Chen(1990)

history. In other words, the material has a memory about its previous state. The hysteresis is due to the energy disspation during magnetization. It is sensitive to the homogeneity of the material and depends also on intrinsic properties M_s and H_a.

Fig. 6.1 shows a characteristic hysteresis loop of a polycrystalline ferromagnetic material (Morrish, 1965; Chen, 1990). Starting from a demagnetised state, the magnetisation, M, increases with an increasing field, H, along the curve OABC, until it reaches a static value called the saturation magnetisation, M_s. If the applied field H is then reduced to zero, M will, from the saturated state C, decrease not along CBAO to zero but along CD to a finite value called the remanence. Increasing H in the opposite direction continues the decrease of M along DEF, until it saturates at F. The field H at point E, where $M = 0$, defines the coercivity H_c. Decreasing H and reversing it along the original direction will cause M to pass from the saturated state F to the other saturated state C along path FGC. The closed loop CDEFGC is the hysteresis loop. The two remanence states D and G are usually used for memory applications. However, there is a so-called demagnetization field even when the external field is removed. A magnetized sample may produce magnetic poles on its surface. the poles in turn produce a magnetic field inside the sample and opposite to the direction of M. This field strength is determined by the magnetization M, the shape of the sample and the magnetic environment. As a result, an operating magnet is not at the remanence state but at a point in the demagnetisation curve DE, at which the largest absolute product of H and magnetic induction B [$B = \mu_0(H + M)$ in SI units] is defined as the energy product $(BH)_{max}$, which is a measure of the magnetic energy applicable in a magnet of a unit volume.

In the present work, M_s and H_c are obtained from hysteresis loops, and H_a is obtained by the singular point detection technique.

6.2 Singular point detection technique, SPD

Introduced by Asti and Rinaldi in 1972, the singular point detection (SPD) technique is an effective and direct method to measure the anisotropy field H_a of a polycrystalline sample. It is found (Asti and Rinaldi, 1974) that the magnetization curve M(H) of a polycrystalline sample has a singularity in the higher order derivative located exactly at H_a, which can thus be directly measured.

The detailed discussion below will focus on hexagonal crystals whose c-axis is the easy magnetisation direction; this is the case relevant to MnBi.

To understand the SPD technique, we will first examine the non-analyticity of the magnetization curve of a single domain particle.

We follow Asti's convention, denoting (x, y, z) as the directional cosines of M_s, instead of Cartesian coordinates (see Fig. 6.2). The directional cosines of the external field, H, are denoted as (a, b, c). To approximate the second term of Eqn. 6.1, the

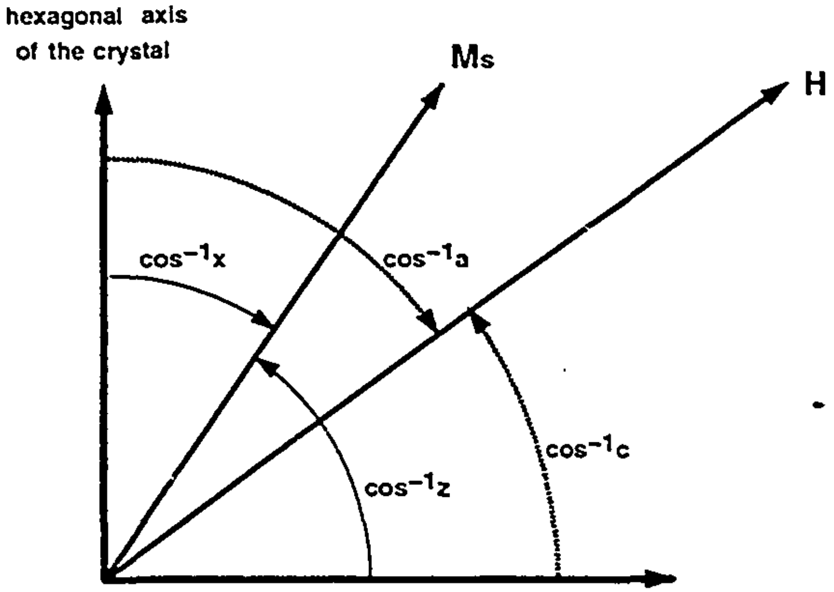

Figure 6.2: (x, z) and (a, c) are defined as the directional cosines of M_s and H respectively in a Cartesian coordinate system referred to the crystal

M_s, H and the hexagonal axis lie in one plane, which is chosen as $y = b = 0$. The magnetization M is the projection of M_s onto the direction of H, and the direction of M_s is found by minimizing the energy. The total energy of the system is the anisotropy part (Eqn. 6.1) minus the scalar product of M_s and H, thus:

$$E = K_1(1 - x^2) + K_2(1 - x^2)^2 - M_s H(ax + cz) \tag{6.3}$$

where x, z and a, c are the directional cosines of M_s and H, respectively.

Defining a dimensionless energy as $\epsilon = E/M_s H$, the equilibrium condition is then

$$\frac{d\epsilon}{dx} = [-2K_1 x - 4K_2(1 - x^2)x]/M_s H - (a - cx/z) = 0 \tag{6.4}$$

and the stable condition is

$$\frac{d^2\epsilon}{dx^2} = [-2K_1 - 4K_2(1 - 3x^2)]/M_s H + c/z + cx^2/z^3 > 0 \qquad (6.5)$$

If the reversible magnetization is approaching saturation ($x \sim 0$) and if H is near the hard direction ($a \sim 0$), then eqn. 6.4 becomes, to first order of a and third order of x,

$$a = \gamma x + Lx^3 \qquad (6.6)$$

and Eqn. 6.5 becomes

$$\gamma + 3Lx^2 > 0 \qquad (6.7)$$

where

$$\gamma = 1 - \frac{H_a}{H} \qquad (6.8)$$

and

$$L = \frac{1}{2} + \frac{4K_2}{M_s H} \qquad (6.9)$$

Equation 6.6 gives three solutions for x; at low fields they are all real, whereas at high fields only one is real. Taking the specific case $a = 0$, we see trivially that for $H < H_a$, there are two stable positions for the magnetization at $x = \pm\sqrt{-\gamma/L}$ and one unstable at $x = 0$. When $H > H_a$, there is only one real solution at $x = 0$ and this is the stable position. As H passes through H_a, the stable solution x is continuous but the derivative $(\partial x/\partial H)$ is discontinuous, and this is reflected in a singularity in the behaviour of the derivative of the magnetization.

The question now is whether the magnetisation curve M(H) of a polycrystalline ferromagnet also exhibits a singularity at H_a. The answer is yes, as shown by Asti and Rinaldi (1972; 1974) both theoretically and experimentally.

Let us consider H approaching H_a and M approaching M_s, so that the domain structure has been eliminated and thus any interaction between grains can be ignored. Under these circumstances, the magnetization of a sample can be approximated as a simple average over M of every grain. Furthermore, we consider only grains whose hard direction almost coincide with H (these grains are responsible for most of the singularity). This implies $\gamma \sim x \sim 0$, $a \sim \gamma x \sim 0^2$ (Eqn. 6.6), so that the M for one grain to the second order of x is

$$M = M_s(ax + cz) \simeq M_s(1 - x^2/2) \tag{6.10}$$

Assuming homogeneous distribution in directions of the grains, the M contributed by these grains can be expressed as

$$M = \int_0^{a_1} M_s(1 - x^2/2)da \tag{6.11}$$

From Eqn. 6.6, $da = (\gamma + 3Lx^2)dx$, so Eqn. 6.11 becomes

$$\begin{aligned} M &= M_s a_1 - \frac{M_s}{2}\int_{x_0}^{x_1} x^2(\gamma + 3Lx^2)dx & (6.12)\\ M &= M_s a_1 - \frac{M_s}{2}[\gamma x^3/3 + 3Lx^5/5]_{x_0}^{x_1} & (6.13)\end{aligned}$$

From the last section, $x_0 = \sqrt{-\gamma/L}$ for $\gamma < 0$, and $x_0 = 0$ for $\gamma > 0$, and there is a singularity in x_0 at H_a. The arbitrary upper limit a_1 and x_1 can be assumed regular, so the M becomes

$$M = \frac{2LM_s}{15}\left(\frac{|\gamma| - \gamma}{2L}\right)^{5/2} + Reg(H) \tag{6.14}$$

where Reg(H) is the regular part of M(H). To the first order approximation near H_a, γ is the reduced field $(H - H_a)/H_a$. The d^2M/dH^2 therefore, has a cusp at H_a (behaviours as $\sqrt{H_a - H}$ below H_a and constant above H_a), which the SPD experiment detects.

6.3 Pulse Magnet and magnetic measurements

Producing a high magnetic field is necessary for measuring hysteresis loop and anisotropy field of polycrystalline MnBi, because only a field much higher than H_a can ensure the saturation of the magnetization. In the present work, we used a pulsed field technique, which is not only an economical and reliable method for achieving high fields (10 – 50 T), but also is helpful for SPD measurement (Grossinger, 1982), since the fast change of the field actually magnifies the signal of dM/dt, the signal detected by a pick-up coil, and hence of d^2M/dt^2. However, when employing a pulsed field, care is needed to extract a reliable signal in a field of such short duration and relatively poor homogeneity.

The pulsed magnet used was first constructed by B. Neufeldt (1989) as part of an M.Sc thesis; later, the computer interface for the ignition control and data acquisition was enhenced by A. Cambron; finally, the author in collaboration with X. Chen rebuilt the temperature control system, pick-up coil, and improved the data acquisition. At present, the system can produce a pulsed field of 22 T, and can be used to measure hysteresis loops and anisotropy fields in the temperature range 80 K to 870 K. The measurement time is so short during a pulse that the temperature can be regarded constant, and the temperature read immediately after a pulse carries an error smaller than 1 K, the resolution of the temperature indicator.

A schematic circuit of the pulsed magnet is shown in Fig. 6.3 The principle of the magnet is to charge a capacitor bank (2mF) to a high voltage (maximum 5 kV), then to discharge it through a solenoid (21.8 mH) that produces a pulsed field. The voltage of the solenoid is clamped by a diode to one direction to prevent a large negative voltage from being applied to the capacitor. As a result, the pulsed field is asymmetric: it rises fast and falls slowly. It reaches its peak value in 10 ms, about quarter cycle of the L-C circuit ($\frac{\pi}{2}\sqrt{CL}$), and takes about 110 ms to fall down as the energy dissipates slowly [exp(-Rt/L)] through the small resistance R (0.5 Ω at 77 K) of the solenoid. The solenoid is 10 cm long with internal and external radii of 1 and 3 cm respectively. An optimistic estimate is that all the energy stored in the capacitor, $CV^2/2$, converts to field energy inside the solenoid space v, $B^2v/2\mu_0$, which gives a peak field of 45 T for 5 kV voltage of the capacitor bank (Neufeldt, 1989).

The solenoid is confined by a steel mantle to prevent it from being deformed by the Lorentz force (see Fig. 6.4). The whole magnet is cooled by liquid nitrogen, which lowers the resistance of the wire. The sample is placed in a small dewar. A heater and a thermo-couple in contact with the sample control the temperature of the sample chamber. Fig. 6.5 shows the sample holder. Wound on the outside of the sample

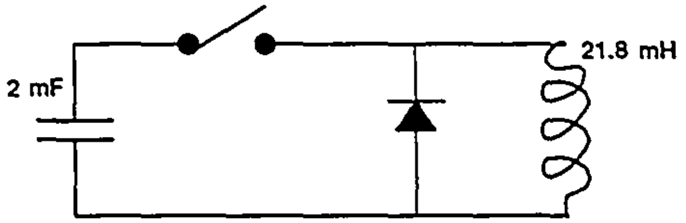

A: Basic Circuit of the Pulsed Magnet

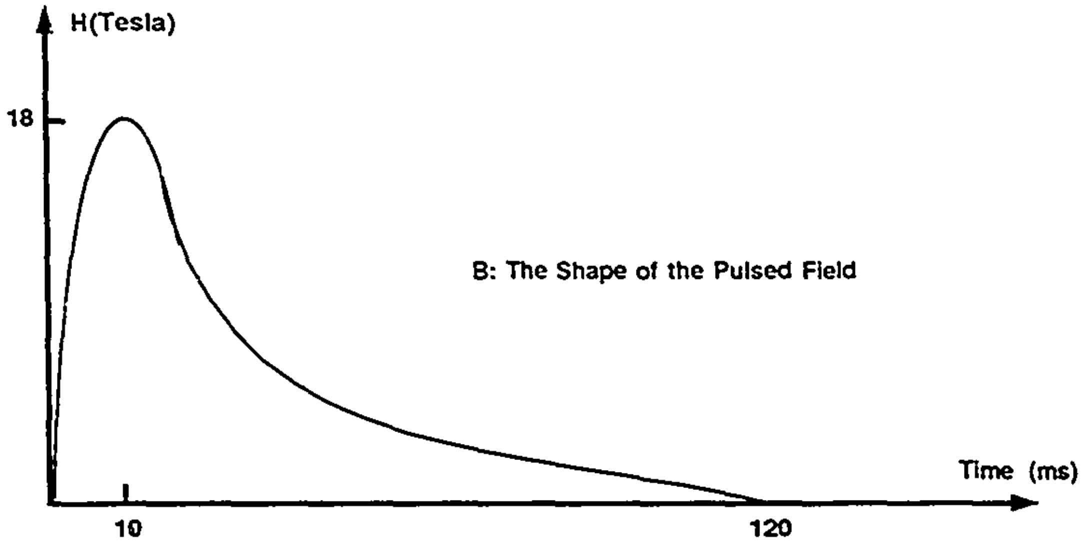

B: The Shape of the Pulsed Field

Figure 6.3: A schematic diagram of the basic circuit and shape of the pulse

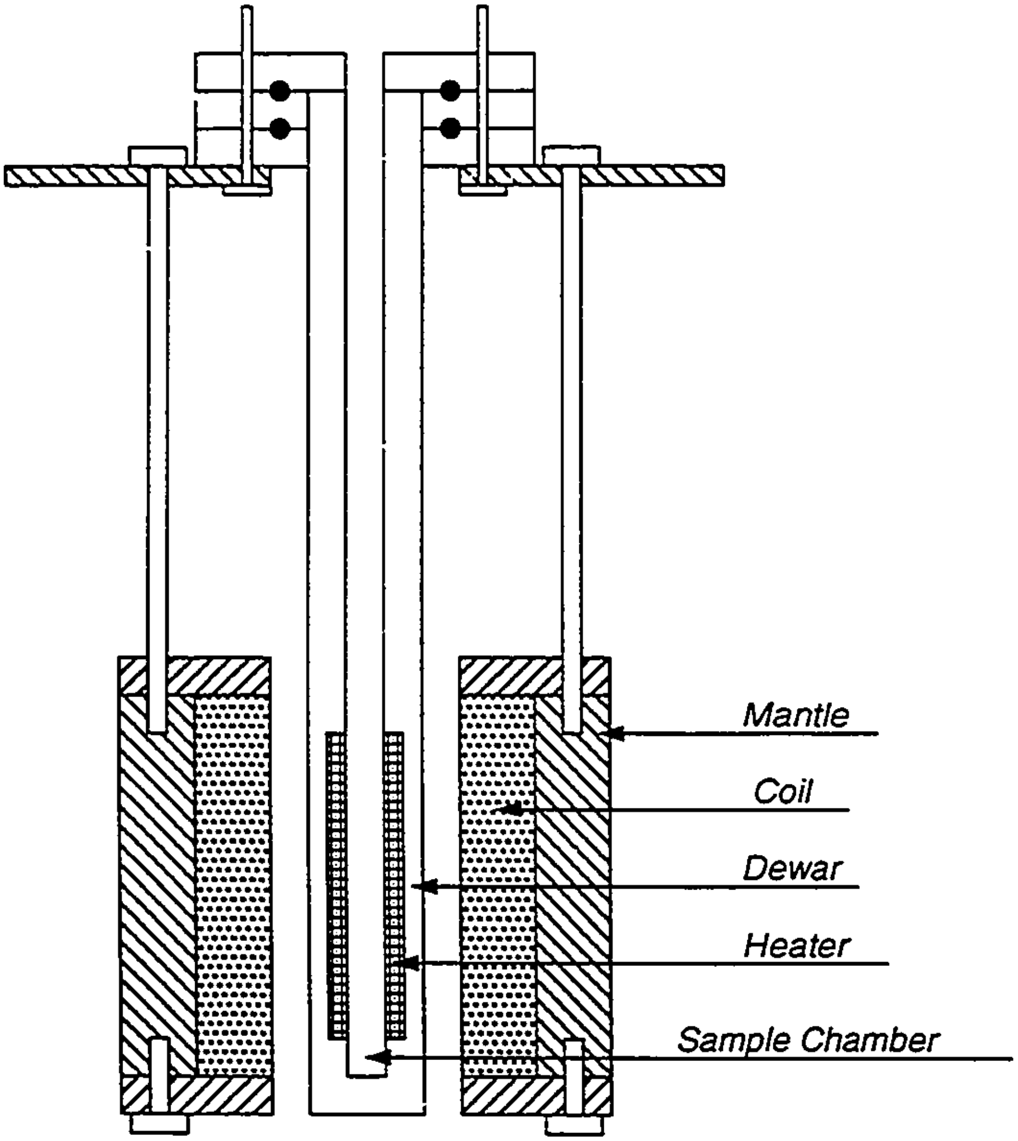

Figure 6.4: A schematic diagram of the magnet

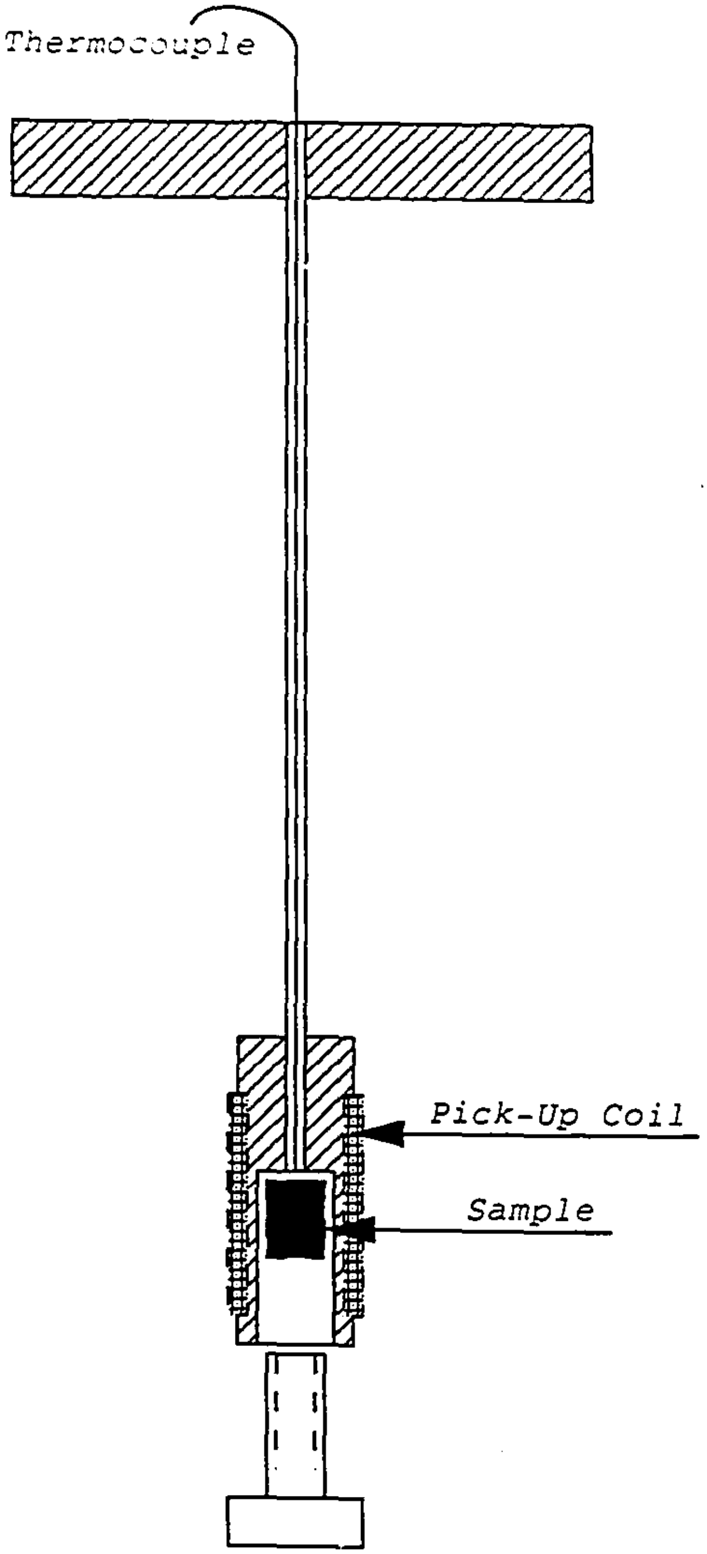

Figure 6.5: A schematic diagram of the sample holder

holder, balanced coils picks up a signal proportional to the rate of magnetization change, dM/dt, of the sample.

This coil is similar in design to that of Allain et al. (1968) (see Fig. 6.6). The main coil with N turns around the sample is compensated by two coil of opposite N/2 turns each at the ends of it. Thus only the rate of change of magnetic flux due to the sample is detected, that due to the pulsed field being mostly cancelled out. The compensation of the coil is better than 99%, as estimated from the flux change rate of the pulsed field in the cross-section of the coil about 0.5 Wb/s and the noise level detected about 5×10^{-3} Wb/s. In addition to the noise, the eddy current induced in the mantle and the elastic deformation of the solenoid under the Lorentz force produce a phase shift between the field and the current. The phase shift is frequency dependent, and produces large error between the data collected during the increasing and decreasing of the field because of the asymmetric shape of the pulse. A phase displacement circuit is used in the coil system to compensate for the phase shift (see Fig. 6.6). The background is first stored in computer which is subtracted from the raw data to reduce any systematic error. Fig. 6.7 shows an example of magnetization measurement. The magnetization in the saturation region for increasing and decreasing fields are the same within the noise, indicating the error cause by the phase shift has been eliminated; the signal to noise ratio is about 20.

The computer collects the data through an analogue-to-digital converter (ADC). The ADC converts data in 3 μs. Taken with the time to store it in memory, the total time to collect one data point is 28 μs. If the field reaches 18 T within 10 ms, there will be on the average 20 data points for M or dM^2/dt^2 per tesla. This gives a resolution in field about 0.05 T. However, the rate of change of the pulsed field is not uniform. The field rises so fast at beginning that only 8 data points can be collected in the first one tesla region of the 18 T pulse. Thus a coercivity below 0.125 T is read as zero within the resolution (see Fig. 6.7). There are two way to integrate dM/dt to obtain M: electronically or digitally. One problem with digital integration is the long falling tail of the pulsed field (Fig. 6.3), which brings in too many data points

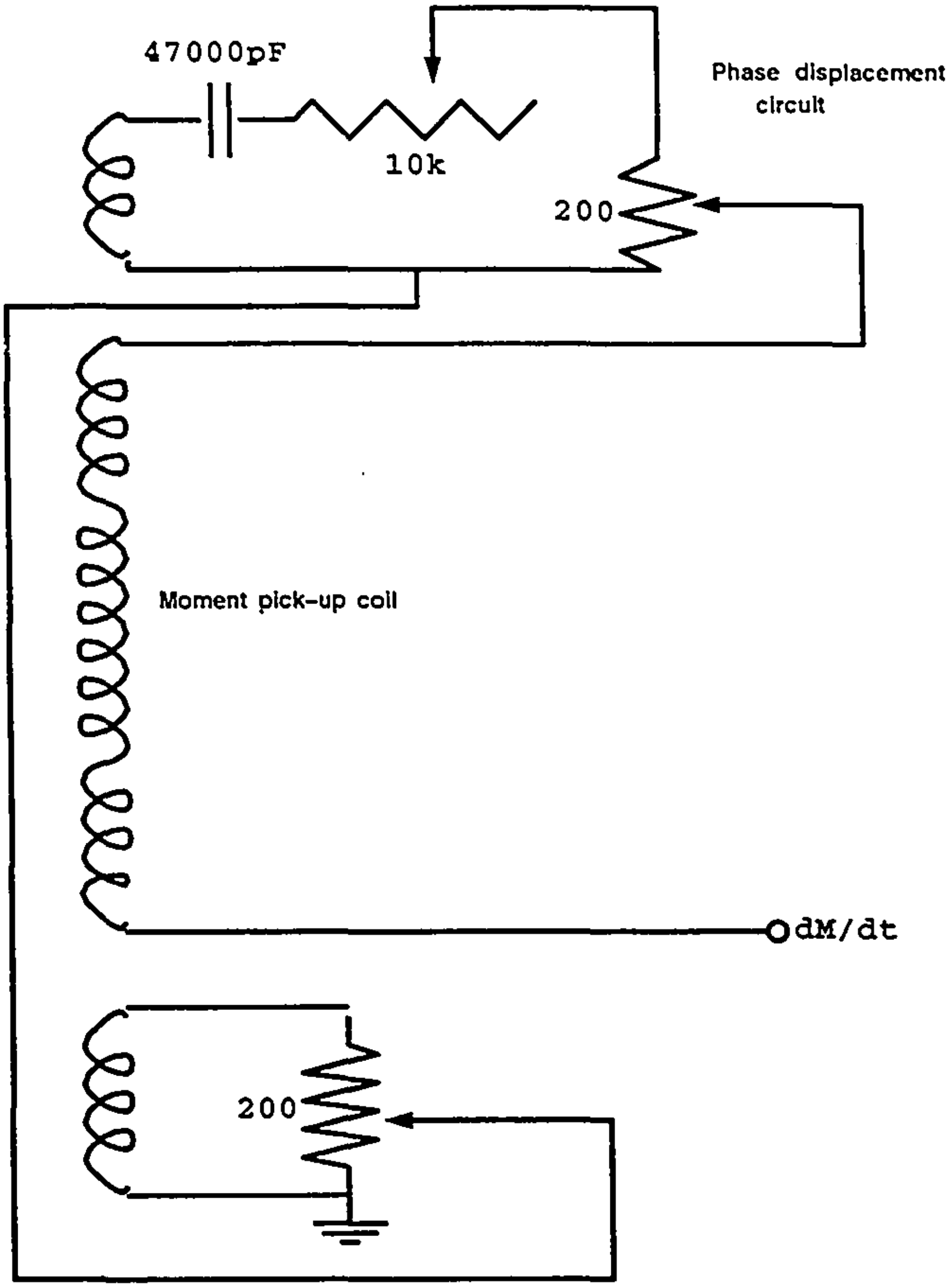

Figure 6.6: The circuit of the pick-up coil

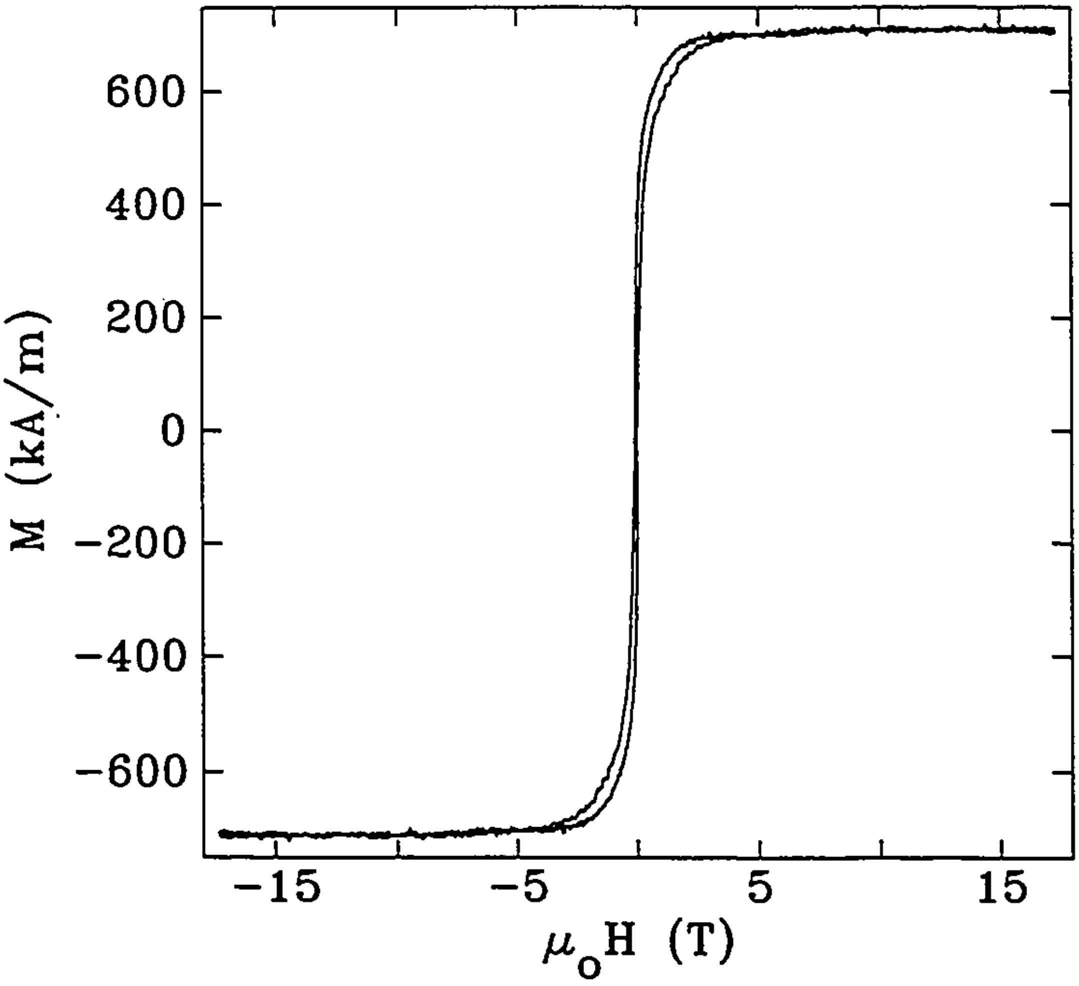

Figure 6.7: Hysteresis loop of LTP at 165 K

into the integration and leads to a significant accumulated digital error. The error is proportional to the square root of the number of the data points. This problem can be solved by diluting the sampling frequency f_s on the falling part of the pulse, and at same time, magnifying the data in proportion to the time waited between two samplings (Neufeldt, 1989). To solve this problem, analogue switches with switching time of 0.1 μs were used to change the magnification when the pulse begins to fall (see Fig. 6.8), and the sampling frequency was controlled in the program by increasing the waiting time for the ADC conversion (see Fig. 6.9). However, the coercivity of MnBi is so low at low temperatures, that most of the magnetization process occurs at the beginning of the pulse where the noise is largest. Digital integration thus becomes unsuitable for measuring materials with relatively low coercivity. As a solution, we use electronic integration for these cases (see Fig. 6.10).

The magnitude of magnetic moment measured by this apparatus is calibrated against a sample of pure Fe cylinder 2.5 mm high and 3.28 mm in diameter. The calibrated linear scale is checked again by measuring the magnetization of a pure Ni sample and the error is contained within 5 %. We use electronic differentiation to get d^2M/dt^2 as well.

The experiment measures d^2M/dt^2 while SPD theory refers to d^2M/dH^2. So the question is what is the relation between d^2M/dt^2 and d^2M/dH^2. For a fast changing field, the magnetization M depends on field H(t) and time t, i.e. $M = M[H(t), t]$ or $dM/dt = (\partial M/\partial H)(dH/dt) + \partial M/\partial t$. As far as SPD is concerned, however, the magnetization near saturation is due to reversible rotation of the magnetic moments and can be regarded as an instant response to the external field. Therefore, we can use the steady approximation of $M = M[H(t)]$ or $dM/dt = (dM/dH)(dH/dt)$. Thus, we get the relation between d^2M/dt^2 and d^2M/dH^2 as

$$\frac{d^2M}{dt^2} = (\frac{dH}{dt})^2\frac{d^2M}{dH^2} + \frac{d^2H}{dt^2}\frac{dM}{dH} \tag{6.15}$$

The last term is regular if H(t) behaves regularly, which gives an offset to the SPD signal and is determined by the sign of the curvature of H(t) (Grossinger, 1982); the first term is the required quantity d^2M/dH^2 that provides the signal for SPD and is

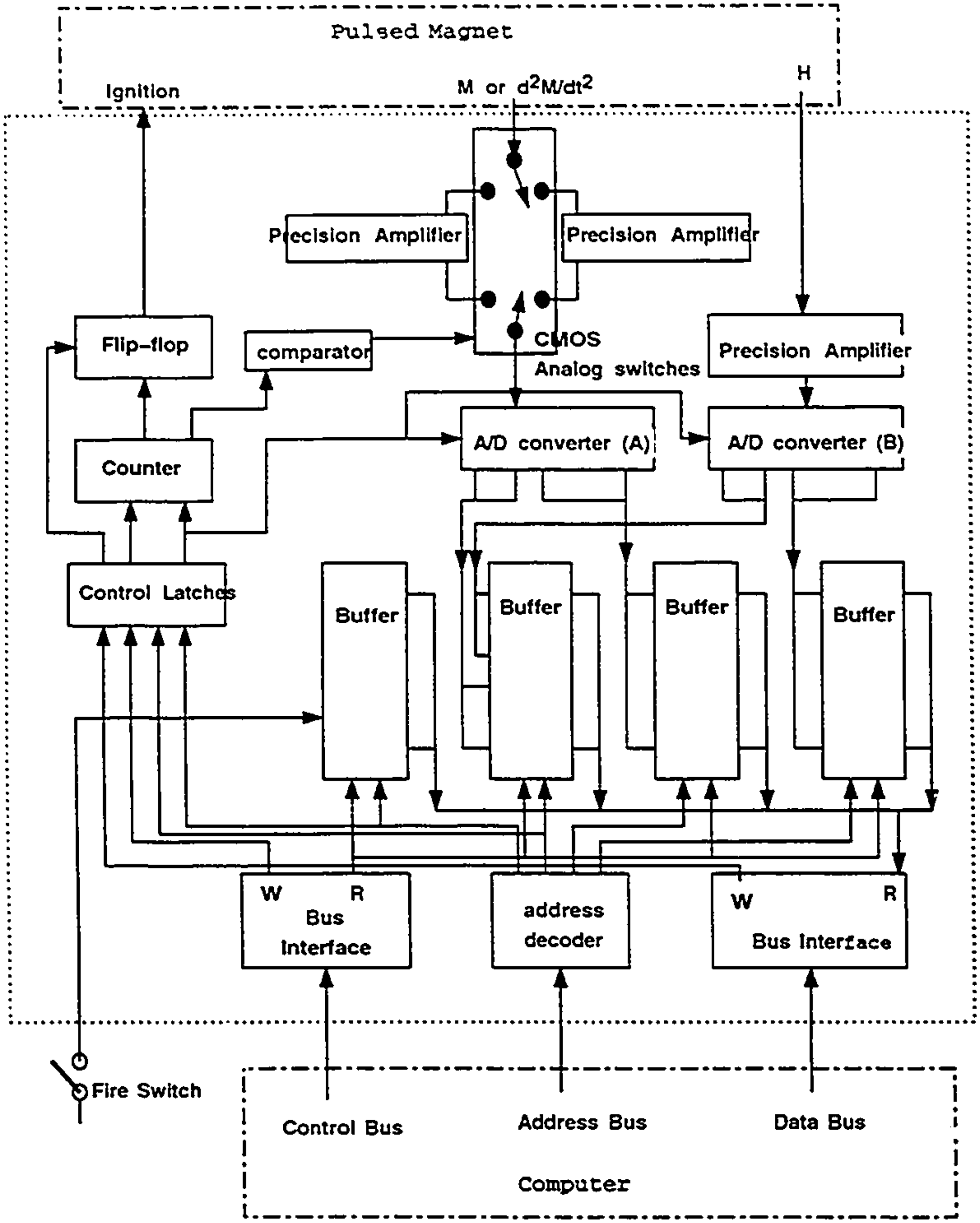

Figure 6.8: A block diagram of computer-magnet interface.

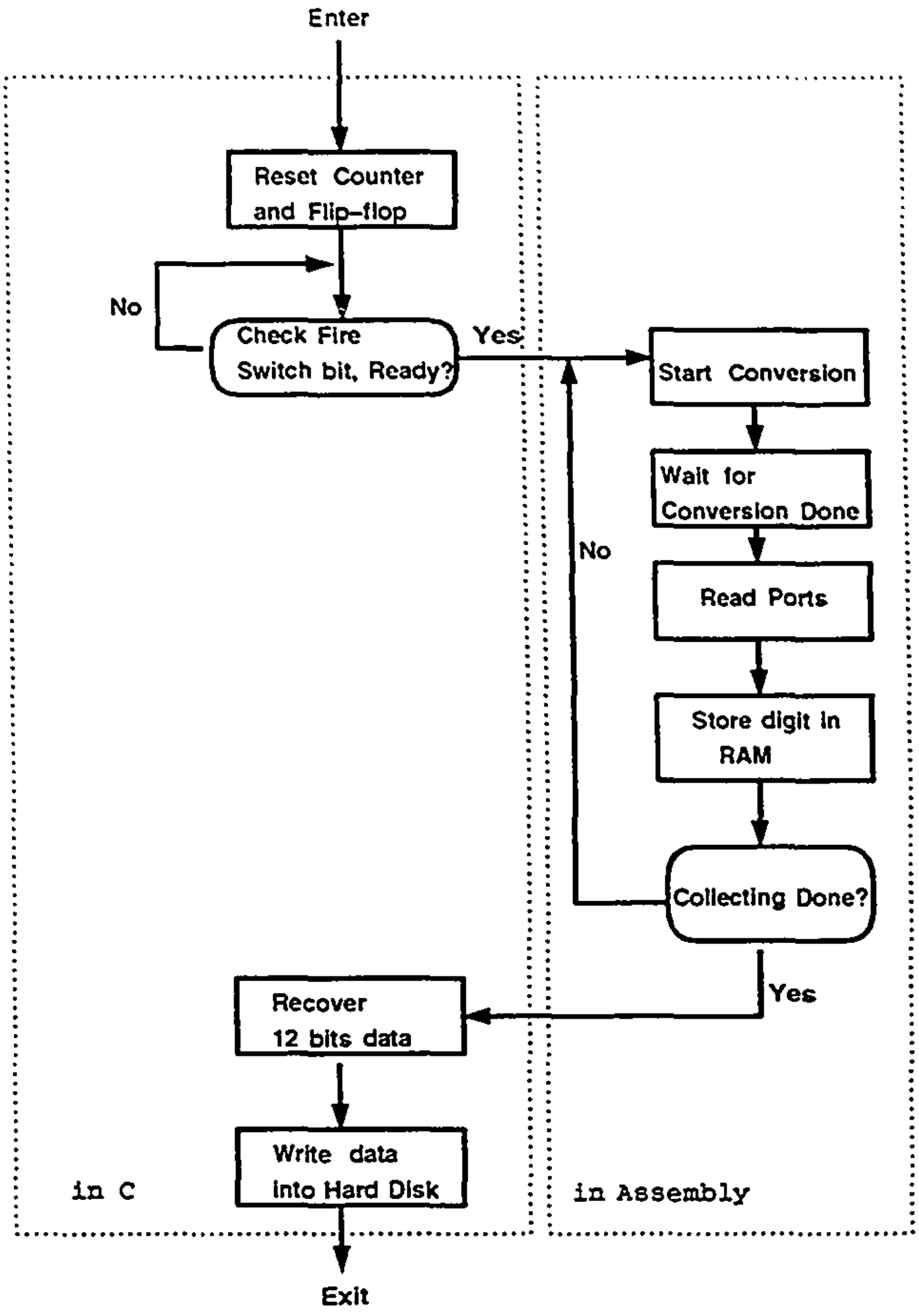

Figure 6.9: A block diagram of the soft ware interface.

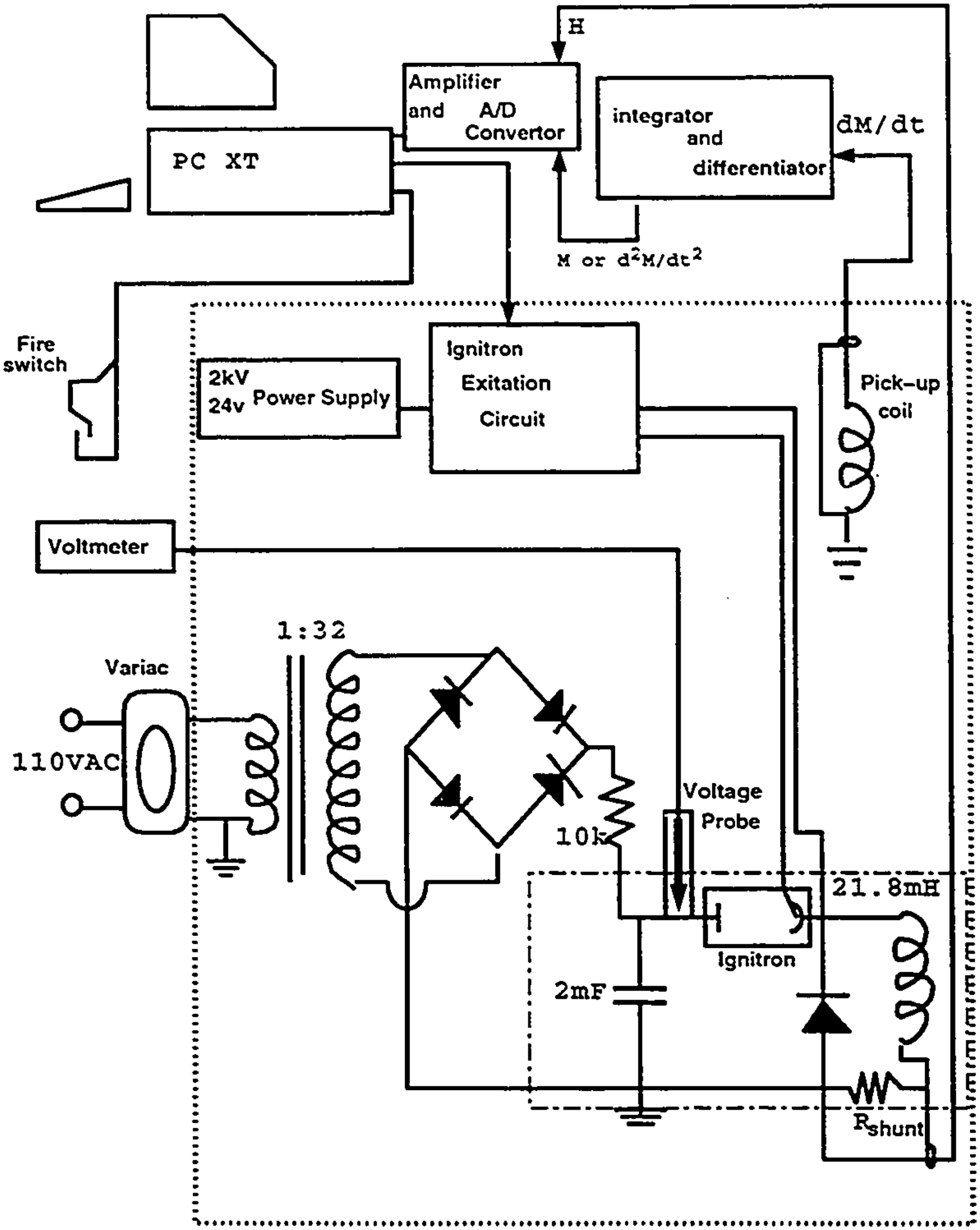

Figure 6.10: The circuit of the pulsed magnet

magnified by the square of dH/dt (Chen *et al.*, 1992). We used the increasing side of the pulse for SPD, because the factor dH/dt is much larger and also H(t) has regular behaviour. [H(t) in the decreasing side of the pulse is not regular when the clamping diode begins to conduct, where H(t) changes from L-C oscillation behaviour to R-L damping behaviour.] From Fig. 6.3, we can see that dH/dt is not a constant. The change of the square of dH/dt is so large that it is difficult for 1024 digital points to represent the signal over the whole field range and still maintain the required resolution. As a solution, an optimized magnification is used so that only the middle part of the whole field range is useful for SPD. Fig. 6.11 shows an example of the SPD measurement. In the low field range, dH/dt is so large that the signal saturates; in the high field range, there is increased noise in proportional to Lorentz stress in the solenoid, and decreased dH/dt, so the signals become undetectable. Therefore, the singularity of d^2M/dt^2 occurs at the same position as d^2M/dH^2, while the signal-to-noise ratio strongly depends on the position of the signal during the pulse.

One way to increase the signal-noise ratio is to reduce the contribution from the regular part in Eqn. 6.15. For this reason, we have adopted the following operational procedure. The specimen is first magnetized to its remanent state, so that the SPD measurement is taken only from the reversible magnetization (from D to C in Fig. 6.1); second, the signal-to-noise ratio is improved by adjusting the voltage of the capacitor bank to alter the maximum field of a pulse, so to put the signal near the middle of the field range where the signal-to-noise ratio is the highest. In Fig. 6.11, we can see that if field range were increased to 18 T, the required signal will be lost in the saturation region; if the field range were reduced to 5 T, the signal will be covered by the noise at the high field region. If a sample has two signals at low and high field respectively, each signal will be detected in a separate measurement of suitable strength of pulse. This is a drawback due to the changing value of dH/dt, but the pulsed magnet can produce significant SPD signal (in Fig. 6.11, the signal-to-noise ratio is at least 4), and measures anisotropy fields from 1.5 to 12 T. The flat SPD signal (see Fig. 6.11) causes an uncertainty in determining the position of the singular point, of about 0.3

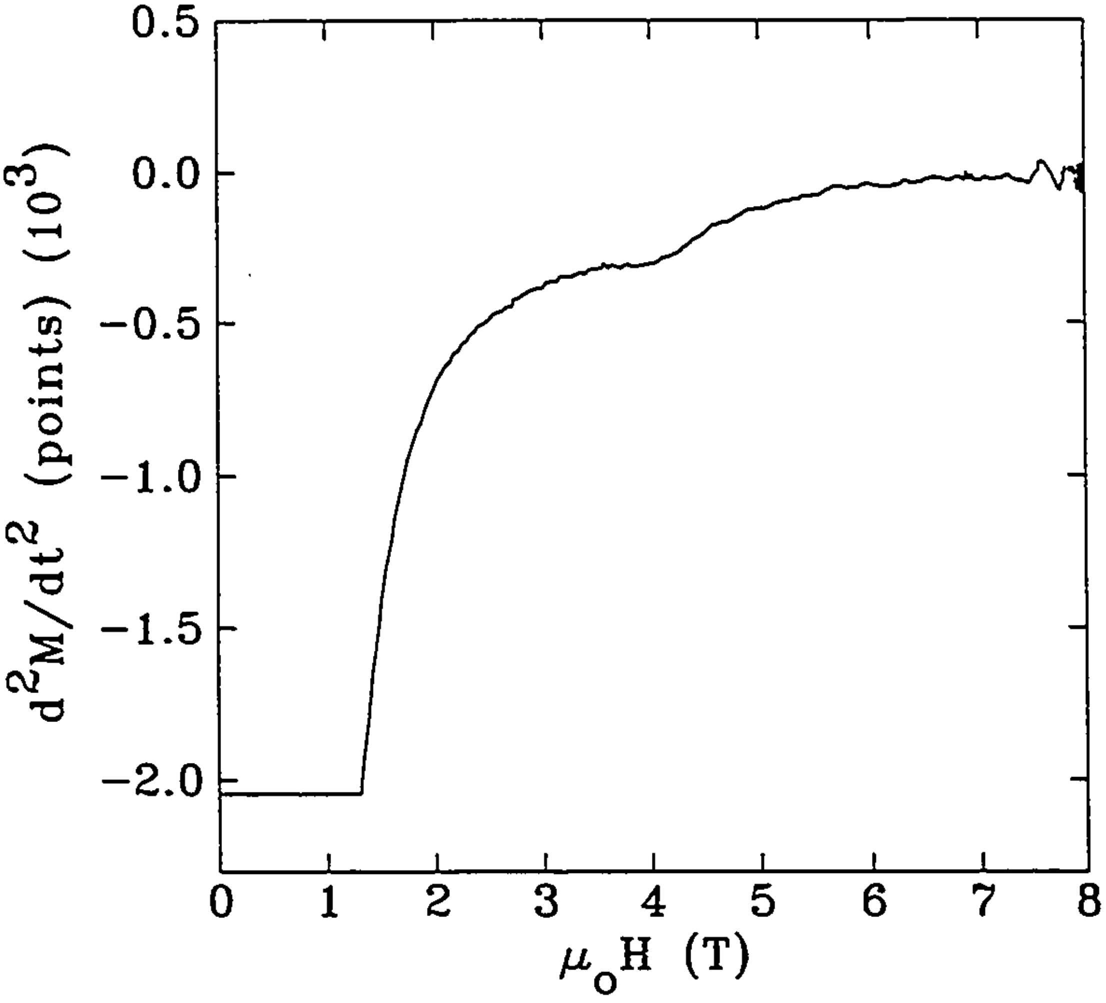

Figure 6.11: A SPD signal of LTP at 256 K detected on the increasing side of a pulsed field of 8 T peak value.

T, compared with which the resolution of the date acquisition system smaller than 0.125 T is satisfactory. The signal-to-noise ratio can also be improved by increasing the sample weight to increase the filling factor of the pick-up coil, and by aligning the hard crystal direction of sample along the field.

The specimen is prepared by compressing 210 mg of as-spun ribbons to form a cylinder 3.1 mm high and 3.28 mm in diameter. This specimen is heated at a rate of 80 K/min to 570 K to form LTP, and is checked by x-ray (Cu-K_α) diffraction. The pulsed field is applied along the axis of the cylinder. The demagnetization factor of the specimen is calculated to be 0.283 (SI units) by interpolating the tabulated value for a cylinder (Chikazumi, 1964), and is used in data processing.

Chapter 7

Results of the measurement of magnetic properties

7.1 Hysteresis loops

Hysteresis loops of LTP of MnBi, prepared by annealing the melt-spun alloy, have been measured in a pulsed field of 18 T from 80 K up to 630 K, the temperature at which LTP transforms into HTP. Fig. 7.1 shows some of the hysteresis loops at different temperatures. Fig 7.2 plots the saturation magnetization, M_s, versus temperature. Roberts (1956) fitted M_s of LTP, obtained by neutron diffraction, to a $J = \frac{1}{2}$ Brillouin function. However, a best fit to our data gives $J = 1.57 \pm .02$, much close to Guillaud's result of $J = \frac{3}{2}$ (1951c). Our data, both in magnitude and temperature dependence, also agree with two other measurements: the data measured by vibrating sample magnetometer on single crystal MnBi (Chen and Stutius, 1974) and that measured by the gradient method on polycrystalline MnBi(Heikes, 1955). Since MnBi undergoes a magneto-structural transition (LTP-HTP), its M_s may deviate from Brillouin (Bean and Rodbell, 1962). In fact, our data are more satisfactorily fitted by the expression

$$M_s(T) = M_s(0)\{(1-p)[1-B(T/T_c)^{3/2}] + p(1-T/T_c)^{1/2}\} \qquad (7.1)$$

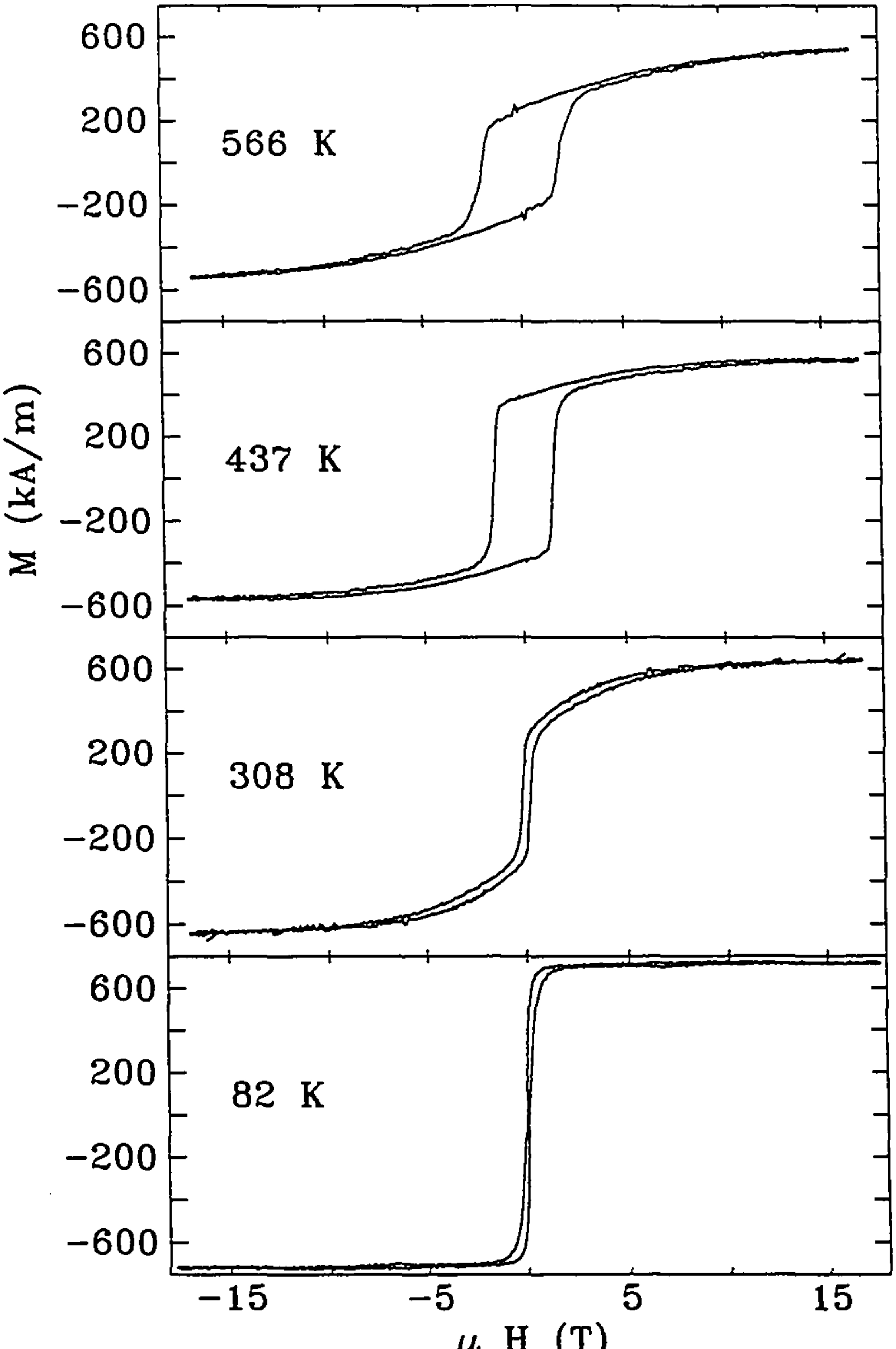

Figure 7.1: Hysteresis loops of LTP at different temperatures

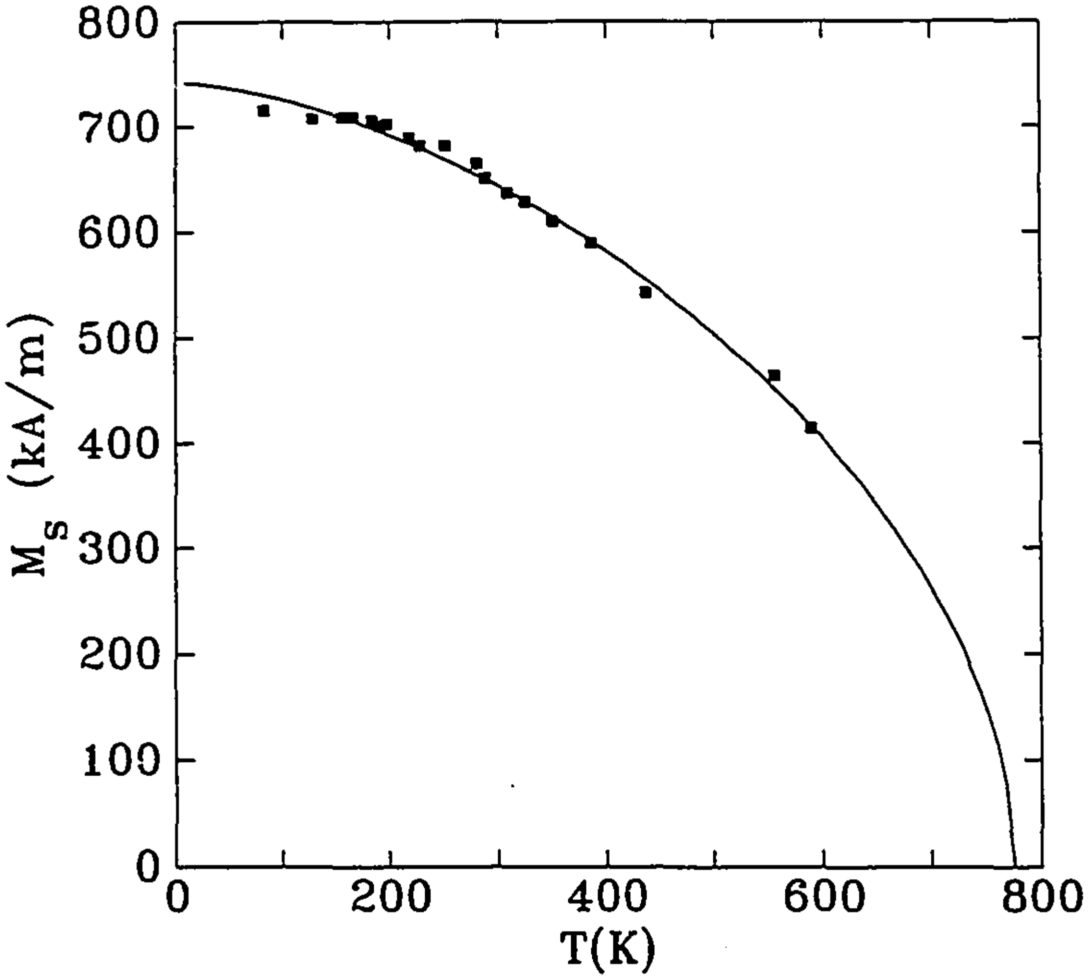

Figure 7.2: Saturation magnetization of MnBi LTP at various temperatures. The square symbols represent the experiment data, and the solid line is calculated from Eq.7.1

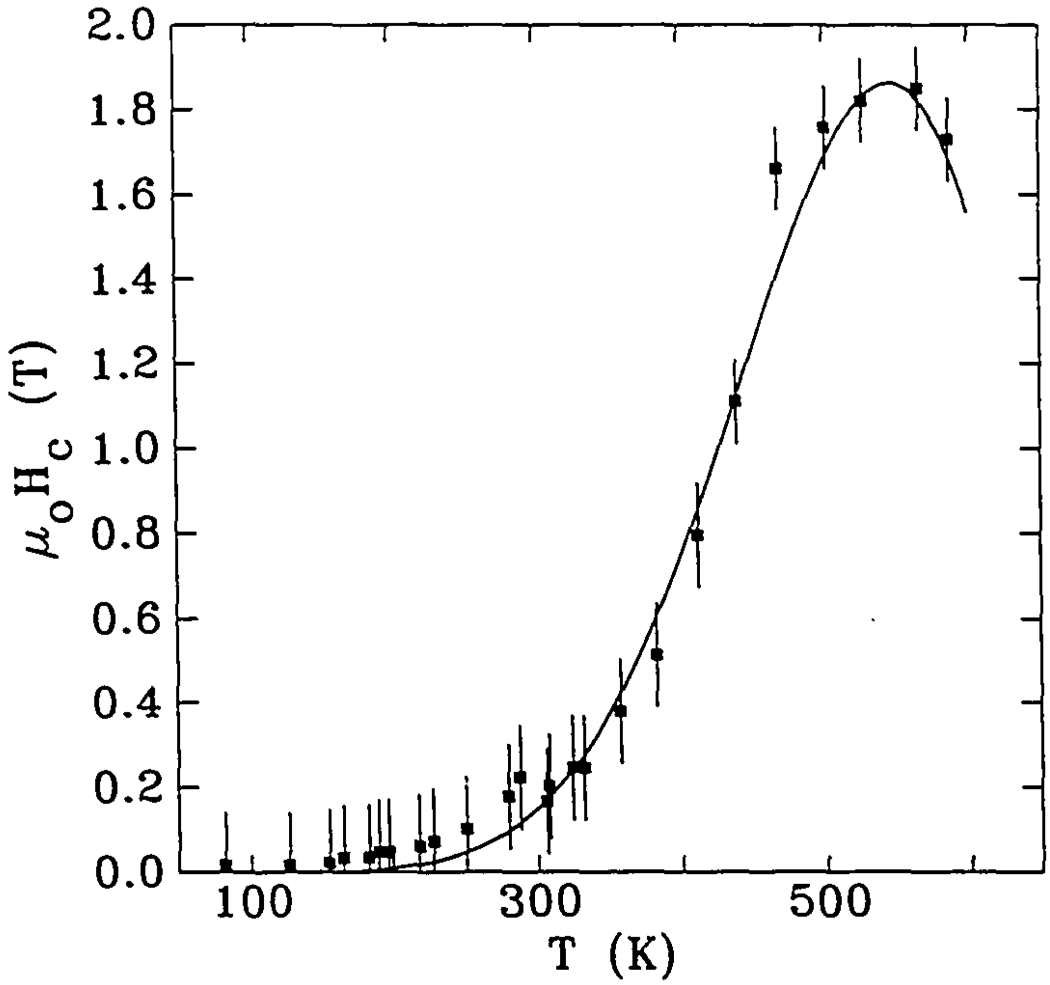

Figure 7.3: The coercive field H_c of LTP prepared by rapid solidification. The square symbols are the experiment data, and the solid line is a fit to the hybrid wall pinning model (see Chapter 8).

where $p = (T/T_c)^n$ is a weight function such that, at low and high temperatures, spin wave behaviour, $[1 - B(T/T_c)^{3/2}]$, and critical point behaviour, $(1 - \frac{T}{T_c})^{1/2}$, are recovered respectively (Callaway, 1976). Best fit to the data gives $M_s(0)$=742 kA/m, B=0.4, n=1.25 and T_c=775 K. If the critical exponent is changed from mean field approximation result of 1/2 to the 3-d Ising model result of about 1/3, the data can also be fitted satisfactory with only a 10% difference in B and T_c. Since the LTP transforms to the high temperature phase at 613 K (Chen and Stutius, 1974), the T_c thus obtained is virtual, and cannot be measured directly in an experiment.

Fig 7.3 plots the coercivity,H_c obtained from the loops, versus temperature. It is not greater than 0.2 T below room temperature, but is increased one order of magnitude at 450 K. Above 450 K, the H_c saturates at 1.7 ± 0.1 T.

7.2 SPD measurement results

Measuring d^2M/dt^2, the SPD technique detects, besides the singularity of magnetization curves, any abrupt changes in the magnetization (Asti and Bolzoni, 1985) even when the amount of the change is very small. We have measured d^2M/dt^2 from 80 K to 600 K. The H_a signature of LTP has been detected from 147 K to 586 K. In addition, a small amount of abrupt changes in magnetization were detected from 80 K to 200 K. These two sets of data will now be presented.

Though there have been many measurements on the anisotropy of LTP (Guillaud, 1951a; Albert and Carr Jr., 1961; Stutius, Chen and Sandin, 1973), we report here, the first direct measurement of H_a of LTP. Fig.7.4 shows a set of SPD signals. The second derivative of magnetization with respect to time, d^2M/dt^2, is plotted against magnetic field for various temperatures. The singular points appear as kinks in these curves. This indicates that the easy magnetization direction lies along the hexagonal c-axis; if the easy direction lies in basal plane, the singular point can only appear in the third derivative (Asti and Rinaldi, 1974). This result about easy direction agrees with reported ones (Hihara and Koi, 1970; Stutius, Chen and Sandin, 1973). Fig.7.5 shows the temperature dependence of the anisotropy field, which has a maximum value of 9 T at 514 K. In the temperature region 400 to 600 K near its maximum value, the H_a is much larger than that of Nd-Fe-B (Grossinger *et al.*, 1987) and has a very low temperature coefficient. The anisotropy constant (Asti and Rinaldi, 1974)

$$K = K_1 + 2K_2 + 3K_3 = \mu_0 H_a M_s/2 \tag{7.2}$$

is calculated from M_s and a polynomial fit to data for H_a. Fig.7.6 shows the calculated anisotropy constant, which has the same trends of temperature dependence as that reported by Chen and Stuitius (1974), where the value of $K_1 + K_2 + K_3$, instead of $K_1 + 2K_2 + 3K_3$, is plotted.

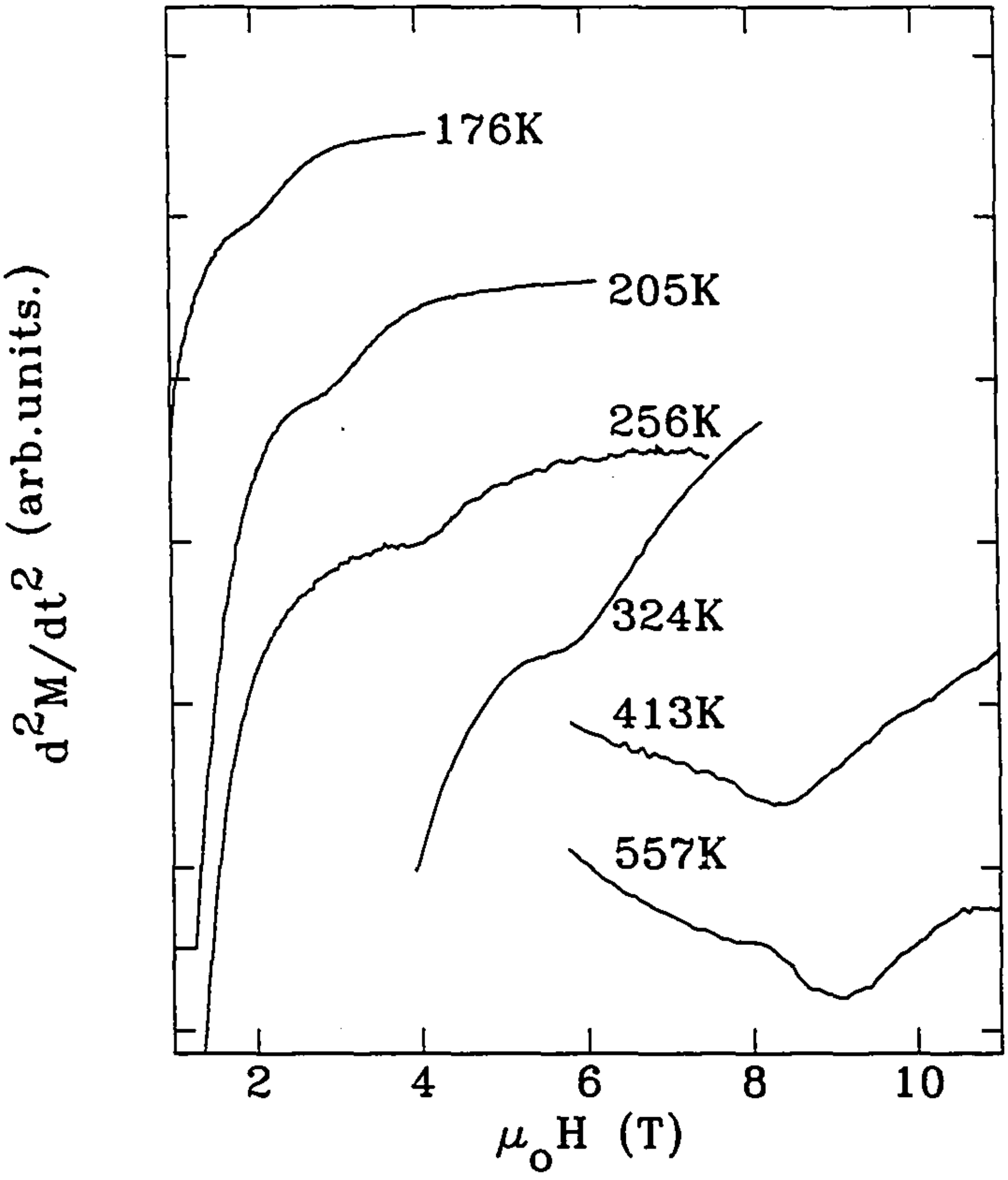

Figure 7.4: Examples of SPD signals. The kinks in the d^2M/dt^2 curves occur at the anisotropy field, H_a.

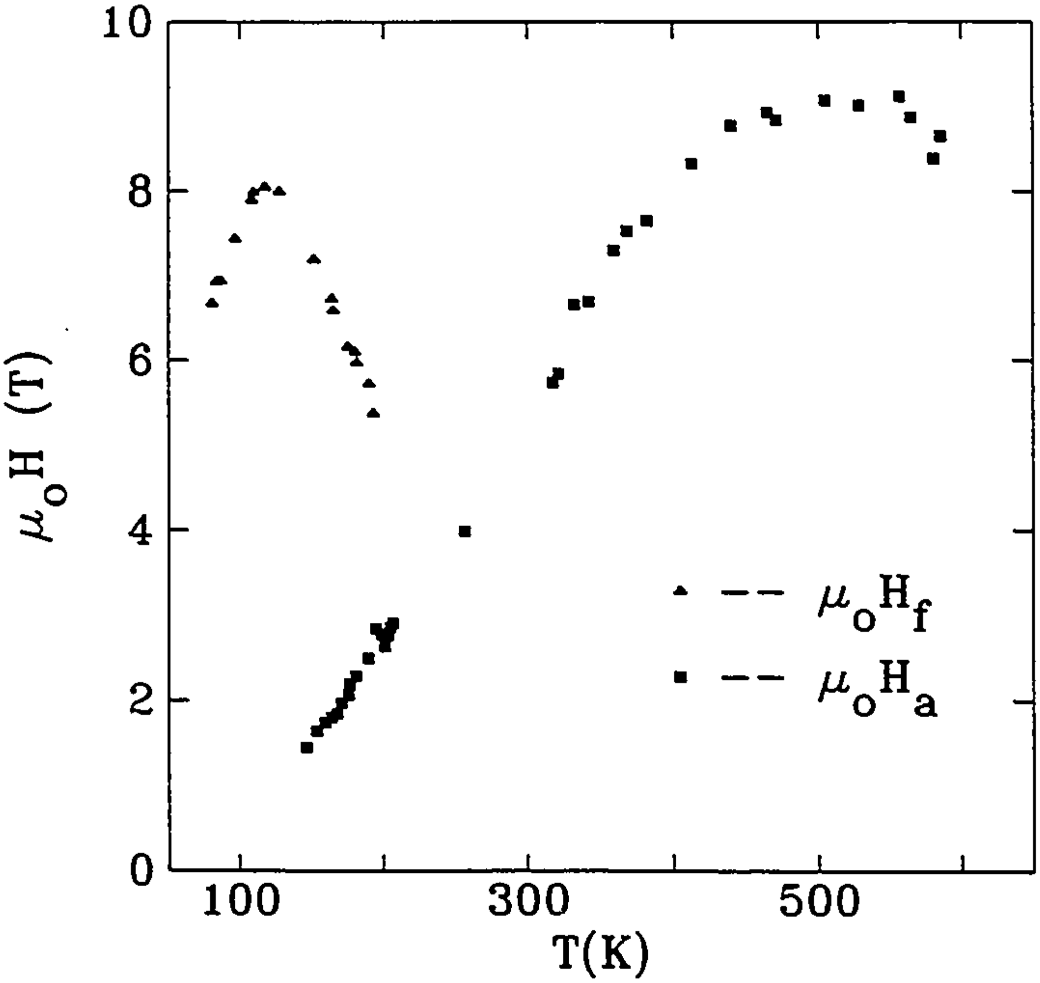

Figure 7.5: Temperature dependence of $\mu_0 H_a$, the anisotropy field of LTP, and the critical field $\mu_0 H_f$ of spin reversal in the HC phase.

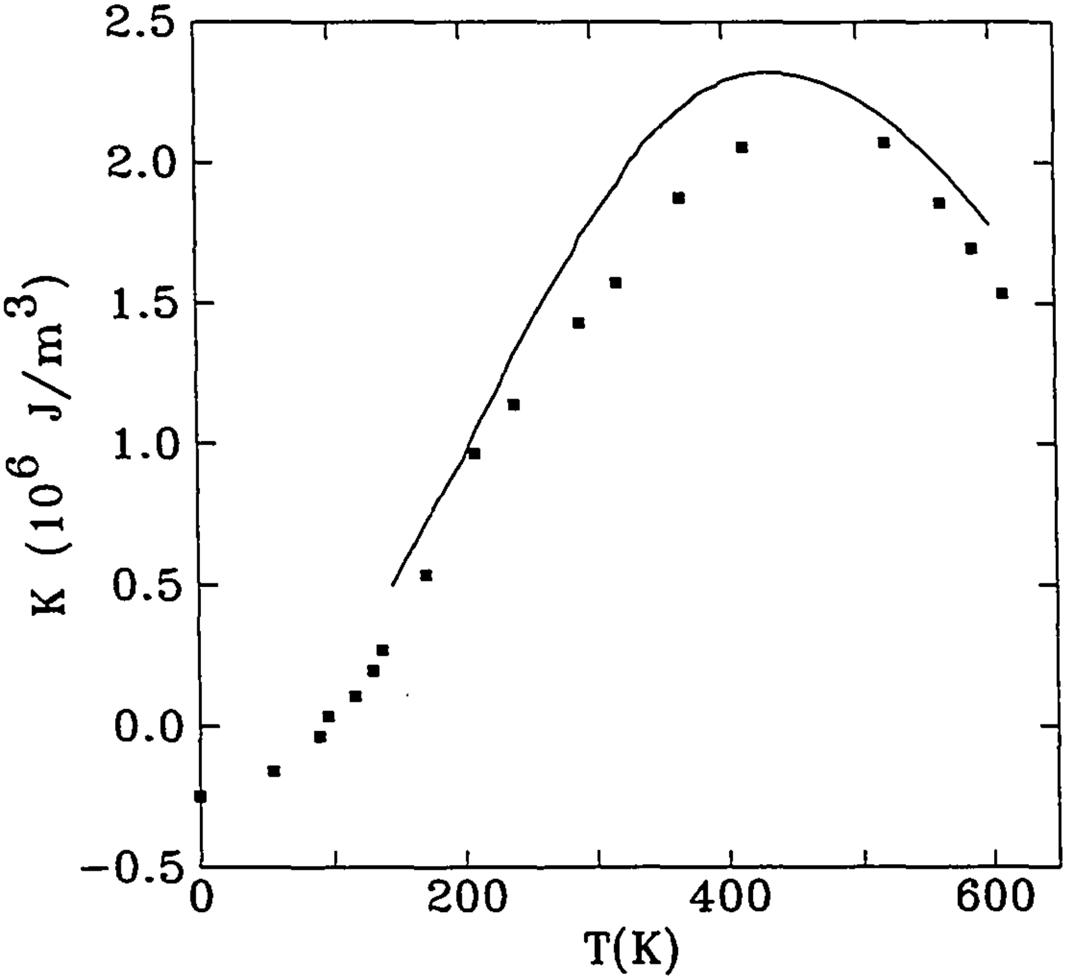

Figure 7.6: Anisotropy constant $K=K_1+2K_2+3K_3$ of LTP is plotted as solid line, compared with reported data of $K_1+K_2+K_3$ of the squares (Stutius, Chen and Sandin, 1973; Chen and Stutius, 1974)

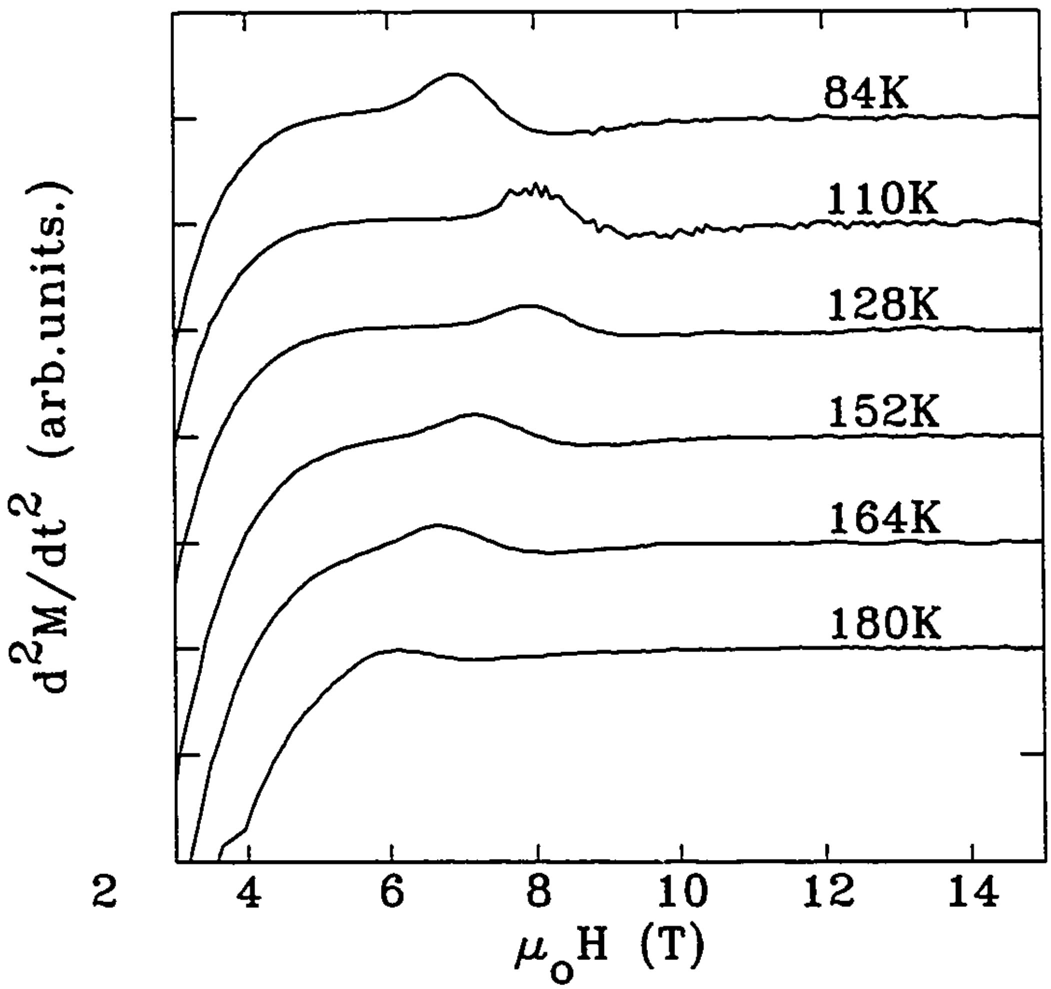

Figure 7.7: Second derivatives, d^2M/dt^2, at various temperatures versus magnetic field, showing the signals originating from the spin reversal of the HC phase.

Below 200 K, an anomalous extremum was observed in the d^2M/dt^2 curves, as shown in Fig.7.7. The temperature dependence of the related critical field, H_f, is plotted also in Fig.7.5. This anomalous extremum is not associated with the anisotropy field. This is shown by the fact that it coexists with the kinks due to H_a over the temperature range 145 to 200 K and is also much higher in value, (see Fig. 7.5). Due to the limitation of instrument, the two kind of signals were detected in separate measurements (see Sec. 6.3). The shape of the extremum is also different from the kinks due to H_a, as may be seen by comparing Fig.7.4 with Fig.7.7. A possible explanation is that it may originate from a first order magnetization process. (Abbreviated as FOMP, it is the magnetization process due to a sudden rotation of magnetic moment between two equilibrium positions. The existence of more than one equilibrium positions in external field is due to certain combination of anisotropic constants of K_1, K_2 and K_3 (Asti and Bolzoni, 1985).) However, using the published data (Stutius, Chen and Sandin, 1973), the critical field of FOMP is estimated to be about 0.5 T, which is much lower than the observed H_f of between 5 and 8 T.

Notis et al.(1978; 1979) and Pirich et al.(1979; 1980) reported a metastable phase, HC, coexisting with LTP. This phase is crystallographically similar to the high temperature phase (HTP) $Mn_{1.08}Bi$, but has a much lower Curie temperature of 240 K. To explain the magnetic properties of the HC phase as ferrimagnetic, Pirich and his co-workers (1979) proposed the following model: Since there are large vacancies in the two equivalent Bi sites (see Fig.2.2), Mn atoms may reside in these interstitial sites. The moment of these interstitial Mn atoms are aligned antiparallel to that of the Mn ions on the main lattice sites. Thus, the HC phase is a defect crystallographic structure whose magnetic properties are dependent on interstitial site occupancy (Pirich, 1979). In the present work, the MnBi LTP is prepared by rapid solidification. The resulting specimen contains a small amount of Bi (< 5 wt. %), and it is possible that the extra Mn atoms occupy the interstitial sites to form the HC phase. The coercivity of HC reported by Notis and Pirich is about 10 T. When the field is applied along the c-axis, they obtain hysteresis loops of single domain behaviour; however, when the field is applied perpendicular to the c-axis, the magnetization drops from saturation to almost zero when field is decreased only to 5 T, which is far from a zero external field (Pirich, 1979). Our data can only be associated with this phenomenon, because our SPD measurement examines only the reversible rotation of spin from the remanent state to the saturated state, not the irreversible process from the opposite remanent state to the saturation. Indeed, the magnitude and temperature dependence of H_f is very similar to H_{c2} reported by Notis (1978). Notis suggested that this is the first order magnetization. However, such a large jump in magnetization near anisotropy field is impossible according to calculation (Asti and Bolzoni, 1980). This phenomenon may come from the complex interactions of magnetic spins between two sublattices, of spins with lattice (anisotropic), and of spins with external fields. It may be similar to spin-flopping phenomena of antiferromagnetic materials (Morrish, 1965). Because the interaction between spins at two different sublattices, the saturation magnetization along the c-axis should be different from that perpendicular to the c-axis. This has been observed by Notis (1979). Because of this, we call H_f the critical field of spin reversal. From Fig.7.5, the apparent ordering temperature (> 200 K) associated with H_f is close to the Curie temperature (240 K) of the HC phase; this provides another evidence for the presence of the HC phase. To obtain further evidence, a specimen was annealed at 570 K for 6 days, and then measured by the SPD method. Annealing should reduce the number of interstitial Mn ions, and hence the amount of HC phase; and in fact, only signals associated with the anisotropy field were observed in the d^2M/dt^2 curve of the annealed specimen, implying that the HC phase had indeed disappeared after such a thermal treatment. This result agrees with that observed by Pirich (1980).

Chapter 8

A domain wall pinning model to describe H_C

8.1 Domain, domain wall and coercivity

Domain theory was first suggested by Weiss (1906; 1907), and has been well developed (Kittel, 1949). A magnetic crystal may be divided to many domains, and each of them has its spontaneous magnetization orientated different to that of their neighbours. Bloch (1932) suggested that there is a transition region, a boundary layer with finite width, that separates the nearest domains. This layer is commonly referred to as a domain wall. In the case of MnBi, there is only one easy direction, so that the nearest domain have their magnetization in opposite direction: parallel or anti-parallel to c-axis. A wall separating these domains is called a 180° wall, for the magnetic moments on the two sides of the wall have 180° difference in their orientations. The moments between nearest lattice sites across the wall thickness, however, have only a small angular displacement. The small angular difference between nearest moments reduces the exchange energy needed for the reorientation of the magnetic moments, and still completes the 180° transition from one domain to the other (see Fig. 8.1). The increased exchange energy is proportional to the square of the angular displacement, and a coefficient A is usually used to denote the strength of the

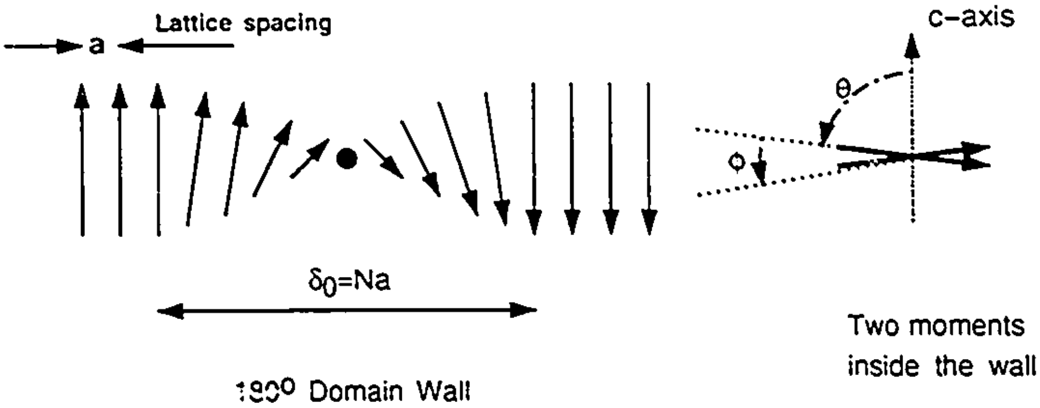

Figure 8.1: The reorientation of moments in side a domain wall, with the increased exchange energy $\sim JS^2(1 - cos\phi)$ and anisotropy energy $\sim K_1 sin^2\theta$.

exchange energy (Chikazumi, 1964). The total increment of exchange energy can be estimated as proportional to the sum of $(\pi/N)^2$, the square of the average angular displacement, over the N lattice distances across the wall width. Consequently, an increased thickness of a domain wall will reduce the exchange energy. On the other hand, an increased wall thickness puts more moments off the easy direction, and hence increases the anisotropy energy. As a result of minimizing energy, the 180° wall thickness δ_0, calculated to the first order of anisotropy energy as $\pi\sqrt{A/K_1}$ (Chikazumi, 1964), increases with the exchange constant A but decreases with anisotropy constant K_1; while domain wall energy of unit area, γ, calculated as $4\sqrt{AK_1}$, increases both with A and K_1.

The domain structure is also a consequence of energy minimization. The spontaneous magnetisation produces free magnetic poles on the surfaces of the material that lead to extra magnetostatic energy. A domain structure can either reduce the magnetic poles on the surface, or make opposite poles to appear closer to minimize the path of the magnetic flux. If the decrease in magnetostatic energy is greater than the domain wall energy needed, a domain structure will form.

Domain structure plays an important role in the magnetization process, and so affects the coercivity. If a particle is smaller than a certain critical size, it will not form domains because the magnetostatic energy is small compared with domain wall energy. This particle is called single domain particle. For this particle, the magnetization process is the coherent rotation of all the magnetic moments in the particle, and the coercivity, the field needed to overcome the anisotropy to rotate the moments in this case, is simply equal to the anisotropy field (Stoner, S. and Wohlfarth, 1948)

$$H_c = H_a - NM_s \tag{8.1}$$

where the last term is the demagnetization field with N determined by the shape of the particle. For a particle that contains domain structure, the magnetization process involves domain wall nucleation and propagation. Contrary to the case in single domain particles, these processes are non-collective: only a small fraction of the moments (the moments inside domain walls) is involved in rotation at any one time. As a result, H_c may be much smaller than H_a and thermal activation will play a significant role in the magnetization. Consequently, the H_c is strongly affected by the homogeneity of a material. A domain wall tends to stay wherever there is a defect, such as a grain boundary of a impurity, within or around which the exchange and/or anisotropy energy are smaller than the matrix. The domain wall that find a position around defects and lower its energy is called being pinned by the defects. Theory taking this into account to explain H_c is called a domain wall pinning theory.

An empirical formula is often used to express the coercive field (Givord *et al.*, 1990)

$$H_c = \alpha H_a - N_{eff} M_s \tag{8.2}$$

Compared with Eqn. 8.1, the α represents the departure from collective rotation if it is smaller than one, and N_{eff} takes into account not only the particle shape, but also thermal activation and the local heterogeneous magnetization state. Fig. 8.2 compares the H_c with the H_a of LTP. The H_c changes much faster than the H_a does near 400 K such that Eqn. 8.2 can not describe the relation between H_a and

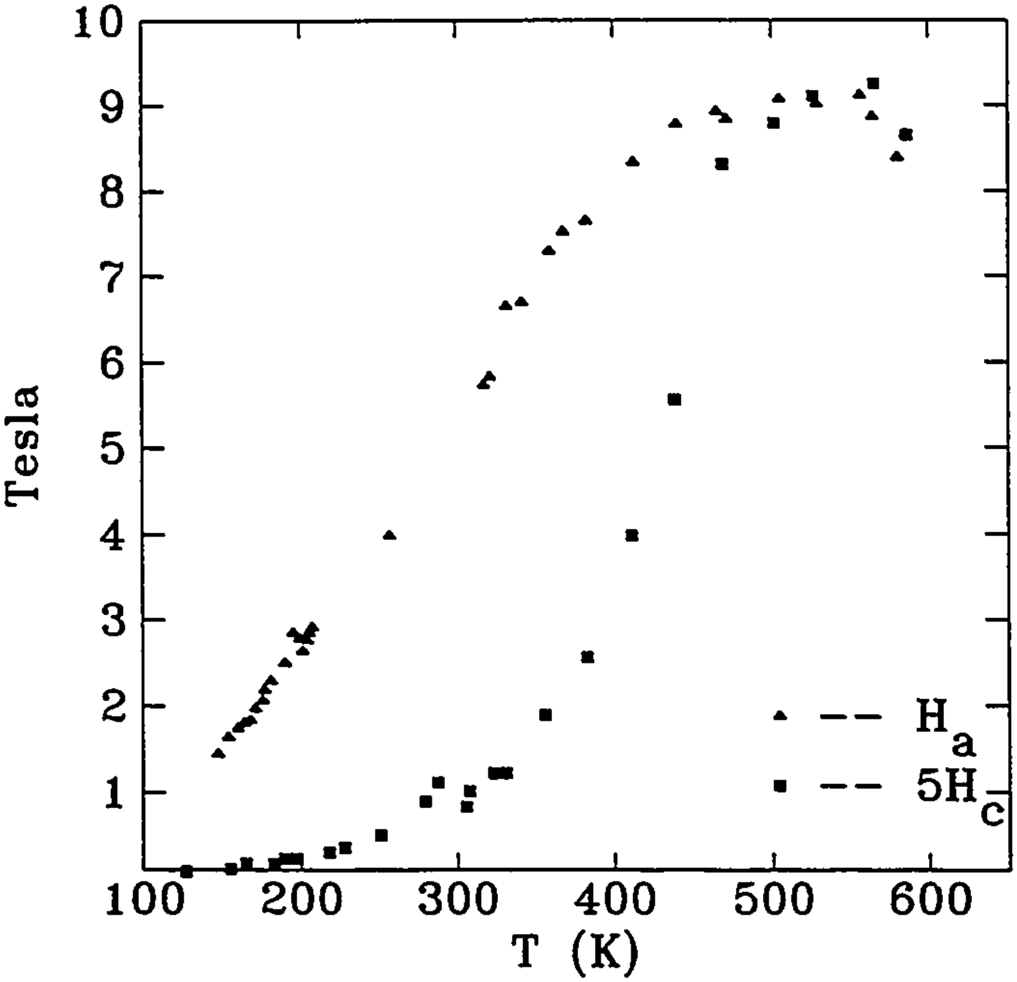

Figure 8.2: The coercivity, H_c, is enlarged five times to compare with the anisotropy field, H_a

H_c. However, combining Hilzinger and Kronmüller's model of wall bowing in two dimensions, (1977a; 1977) with Gaunt's consideration of thermal activation (1984; 1983), produces a hybrid model which fits the data satisfactorily.

8.2 Hilzinger's scaling theory

Hilzinger (1977a) developed a scaling theory that produces a variety of expressions of coercivity corresponding to different pinning mechanisms (Hilzinger and Kronmüller , 1977; Gaunt, 1984). We only focus our discussion to the statistical theory (Hilzinger and Kronmüller , 1977) of a domain wall with anisotropic flexibility.

Consider a flexible 180° domain wall with z-axis in easy direction and y-axis normal to the domain wall (see Fig. 8.3). The shape of the domain wall is described by the coordinator y as a function of x and z, i.e. the surface of the wall satisfies $y(x, z)$. The partial derivatives of $y(x, z)$ are denoted as y_x and y_z. The magnetizations of the two domains, separated by the wall, are $\mathbf{M_1}$ and $\mathbf{M_2}$ respectively, with magnitude of M_s and with opposite directions. The domain wall is vaulted and shifted to a new equilibrium position under an external field H, and has an energy increment W expressed as a functional of domain wall shape $y(x, z)$

$$\begin{aligned} W[y(x,z)] = \int\int \; dxdz \quad & \{(\gamma/2)[(y_x)^2 + (y_z)^2] \\ + \quad & 2M_s^2(y_z) \int\int \frac{\partial y(x_1, z_1)/\partial z_1}{|\mathbf{r} - \mathbf{r_1}|} dx_1 dz_1 \\ + \quad & \sum_i \delta(x - x_i)\delta(z - z_i)\Psi[(y_i - y(x,z))/\delta_0] \\ - \quad & (\mathbf{M_1} - \mathbf{M_2}) \cdot \mathbf{H} y\} \end{aligned} \tag{8.3}$$

The first term is the surface energy where γ denotes the specific energy of a domain wall; the second term results from stray field - the interaction of the magnetic charge produced by the wall curvature along the c-axis; the third term is the sum of interaction energies $\Psi(d)$ of defects located at (x_i, y_i), where d is the defect-wall distance scaled by the wall thickness δ_0; the last term is due to the magnetization in the external field H. The variation of the energy with respect to $y(x, z)$ will give the equation

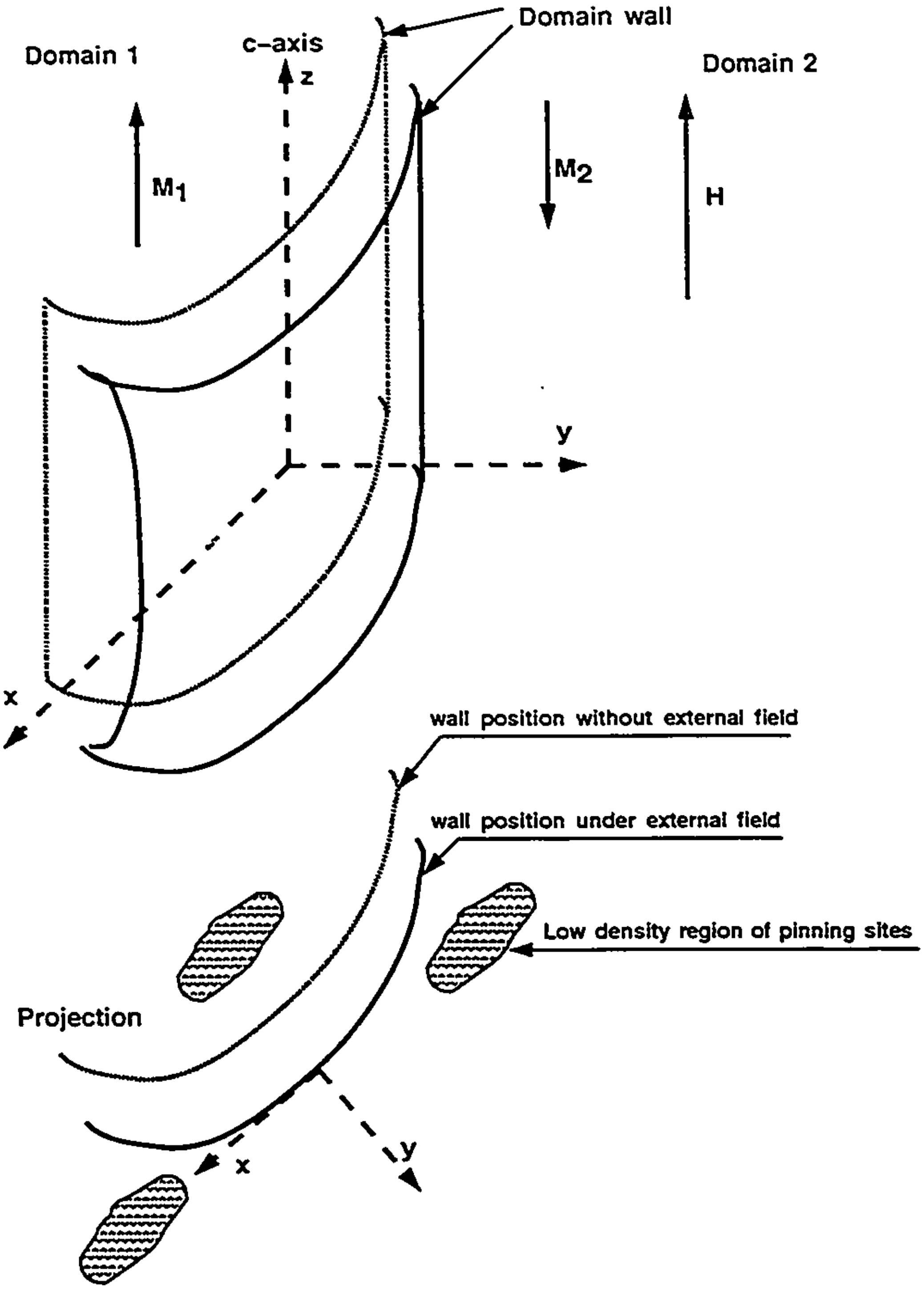

Figure 8.3: A schematic diagram of a domain wall pinned due to the density fluctuation of defects.

for the equilibrium wall shape $y(x,z)$:

$$\begin{aligned} y_{xx} &+ y_{zz} + (4M_s^2/\gamma)\frac{\partial}{\partial z}\int\int \frac{\partial y(x_1,z_1)/\partial z_1}{|\mathbf{r}-\mathbf{r}_1|}dx_1dz_1 \\ &- (f_0/\gamma)\sum_i \delta(x-x_i)\delta(z-z_i)\Phi[(y_i - y(x,z))/\delta_0] \\ &+ 2M_sH/\gamma = 0 \end{aligned} \tag{8.4}$$

where y_{xx} and y_{zz} are the partial derivatives in the second order of $y(x,z)$, and f_0 is a measure of the pinning force by a defect. When the field H is too large, there will be no solution $y(x,z)$ that still satisfies Eqn. 8.4, for the domain wall will keep moving under the external field till it vanishes at the boundary. At a critical point, the equilibrium shape $y(x,z)$, a solution of Eqn. 8.4, marginally exists and produces a lagest minimum energy W of Eqn. 8.3. The critical field at this point is the coercivity H_c. For this point, Hilzinger assumed the following expression for the driving force $2H_cM_s/\gamma$ in Eqn. 8.4

$$H_cM_s/\gamma = constant \cdot \rho^\alpha (f_0/\gamma)^\beta \delta_0^\varepsilon (M_s^2/\gamma)^\omega \tag{8.5}$$

where H_c is the coercivity, ρ the density of defects, and α, β, ε, ω are exponents to be determined by scaling considerations.

The scaling procedure is first to scale the space (e.g., $y' = 2y$) of Eqn. 8.4, then to find out the corresponding change of each parameter in Eqn. 8.4 that keeps the equation unchanged, and to insert the changed parameters into Eqn. 8.5 to get the scaling equations. However, the scaling of Eqn. 8.4 is impossible without approximation. For anisotropic domain that is easy to vault along x-direction but difficult along z-diretion, the following approximations are used: the curvature along x-axis is much larger than along z-axis, so that $y_{xx} \gg y_{zz}$; $|\mathbf{r}-\mathbf{r}_1|$ scale as z for the stray field and geometry considerations. Thus, if y is scaled by a factor of 2, the parameters change as $\rho \to \rho/2$, $f_0/\gamma \to 2f_0/\gamma$, $\delta_0 \to 2\delta_0$, $H_cM_s/\gamma \to 2H_cM_s/\gamma$, and $M_s^2/\gamma \to M_s^2/\gamma$. Eqn. 8.5 then, gives

$$2 = (1/2)^\alpha (2)^\beta (2)^\varepsilon (1)^\omega \tag{8.6}$$

so that

$$1 = -\alpha + \beta + \varepsilon \tag{8.7}$$

Similarly, scaling in the z-direction yields

$$0 = -\alpha + \beta + 2\omega \tag{8.8}$$

and in x-direction

$$2 = \alpha + \beta + 3\omega \tag{8.9}$$

In addition, to the scaling relations derived from this procedure, an additional relation is obtained from statistical reasons. For a large number of defects, their interaction on one side of a domain wall is almost cancelled by that from the other side, so the pinning force is produced by the fluctuation of the spacial distribution of the defect. If the density of defects, ρ, is doubled, the fluctuation, and so the strength of the force f_0, increases only by a factor of $\sqrt{2}$. This gives the relation

$$\beta = 2\alpha \tag{8.10}$$

Solution of these relations is

$$\alpha = 4/3,\ \beta = 8/3,\ \varepsilon = -1/3\ and\ \omega = -2/3 \tag{8.11}$$

The coercivity in Eqn. 8.5 is then expressed as

$$H_c = const \cdot \frac{\rho^{4/3} f^{8/3} \delta_0^{1/3}}{M_s \gamma^{5/3}} (8\pi M_s^2 \delta_0/\gamma)^{-2/3} \tag{8.12}$$

8.3 Gaunt's thermal activation of domain walls

Gaunt approaches Eqns.8.3 and 8.4 from a different way. He showed that, with some approximations, Eqn.8.4 can have two solutions for a given H: one corresponds to the minimum energy of Equ.8.3, another corresponds to the maximum energy. The wall begins to break off at the maximum energy state. If thermal activation can make up the energy difference of the two states, then the H is the coercivity.

Assuming (Gaunt and Mylvaganam, 1979) (a) the stray field is negligible; (b) the interaction energy of the sum over defects (the third term in Eqn. 8.3) can be approximated as

$$F[(y + b) - (y^3 + b^3)/3b^2] \tag{8.13}$$

where F and b are constants; (c) $y(x,z)$, the domain wall shape, is of cylindrical symmetry. Eqn. 8.3 becomes

$$W(y) = \int 2\pi r\, dr\, \{\gamma(y')^2/2 + F[(y+b) - (y^3+b^3)/3b^2] - 2yM_sH\} \tag{8.14}$$

and Eqn. 8.4 becomes

$$y'' + \frac{y'}{r} + \frac{F}{\gamma}[1 - (y/b)^2] + 2M_sH/\gamma = 0 \tag{8.15}$$

One obvious solution of Eqn. 8.15 is

$$y_\pm = \pm b\sqrt{1 - 2M_sH/F} \tag{8.16}$$

The negative solution, y_-, is more stable than y_+, as can be seen by substituting them back to Eqn. 8.3. The physical meaning of y_- is that a plane wall has an equilibrium position at $-b$ in the absence of external field, and has a new equilibrium position at y_- in the external field. The energy E needed for the wall to form a blister (a portion of the wall that bows out) is expressed by Gaunt as the energy $W(y)$ of a vaulted wall $y(x,z)$ minus $W(y_-)$, that of wall in equilibrium

$$E = \int 2\pi r\, dr\, [\gamma(y')^2/2 + (F - 2M_sH)(y - y_-) - F(y^3 - y_-^3)/3b^2] \tag{8.17}$$

Using the substitutions

$$\begin{aligned} Y &= y/|y_-| \\ R &= \frac{r}{b}\sqrt{F|y_-|/\gamma} \end{aligned} \tag{8.18}$$

E is expressed as

$$E = \gamma b^2(1 - 2M_sH/F)\int 2\pi R dR[\frac{2}{3} + Z - \frac{Z^3}{3} + (Z')^2/2] \tag{8.19}$$

The dimensionless integral was calculated numerically by Gaunt as 31, so that

$$E = 31\gamma b^2(1 - 2M_sH/F) \tag{8.20}$$

The time, τ, required for unpinning of the wall by thermal activation is related to the energy E as

$$\tau^{-1} = Cexp(-E/kT) \tag{8.21}$$

where C is a frequency constant taken as 10^{11} Hz (Gaunt, 1976). For the measurement in the pulsed magnetic field, data is sampled every 28 μs. Taking this sampling time as τ yields $E = 15$ kT. Inserting this value into Eqn. 8.20 gives coercivity

$$H_c = \frac{F}{2M_s}(1 - \frac{15kT}{31\gamma b^2}) \tag{8.22}$$

8.4 A hybrid model applied to MnBi

It has been observed that in samples of LTP, the domains form straight strip patterns when the observation plane is parallel to the c-axis of the LTP crystal, but form rick-rack pattern when the plane is vertical to the c-axis (Sher, Shtol'ts and Margolina, 1960; Roberts and Bean, 1954; Honda, Konishi and Kusuda, 1972). This domain structure implies an anisotropy in flexibility of the domain wall, and hence suggests that Eqn. 8.12 is applicable. Furthermore, deduced from the same energy consideration Eqn. 8.3, Eqns. 8.12 and 8.22 are compatible (Gaunt, 1984) and Eqn. 8.22 should reduce to Eqn. 8.12 when the temperature is small. Thus, we can replace $F/2M_s$ in Eqn. 8.22 with the expression of Eqn. 8.12 to form a hybrid model

$$H_c = const \cdot \frac{\rho^{4/3} f^{8/3} \delta_0^{1/3}}{M_s \gamma^{5/3}} (8\pi M_s^2 \delta_0/\gamma)^{-2/3} (1 - \frac{15kT}{31\gamma b^2}) \tag{8.23}$$

This model combines the thermal activation factor $(1 - \frac{15kT}{31\gamma b^2})$ from a particular approximation to Eqn. 8.12 from the general scaling theory.

To apply the hybrid model to describe the temperature behaviour of H_c, the temperature dependence of every factor in Eqn. 8.23 must be known. This will be achieved by finding their relationship with M_s and H_a whose temperature dependences have already been measured.

The defect density ρ is unchanged with temperature, and so can be combined in to constant. The specific energy of a domain wall is expressed as $\gamma = 4\sqrt{AK}$ (Chikazumi, 1964). The anisotropy constant, K, is calculated by Eqn. 7.2 as $K = H_a M_s/2$, and exchange energy is expressed (Stoner, S. and Wohlfarth, 1948) as $A = \alpha M_s^2$, where α

is a constant. Thus, the domain wall energy is

$$\gamma = 4\sqrt{\alpha/2}M_s\sqrt{M_sH_a} \tag{8.24}$$

The thickness of a domain wall is (Chikazumi, 1964)

$$\begin{aligned}\delta_0 &= \pi\sqrt{A/K} \\ &= \pi\sqrt{2\alpha}\sqrt{M_s/H_a}\end{aligned} \tag{8.25}$$

The interaction range, b, can be estimated as follows: From the definition of Eqn. 8.13, the pinning force reaches a maximum when $y = 0$ and is zero at $y = \pm b$, the minimum and maximum energy positions. Therefore, assuming $y = -b$ to be equivalent to a pinning site at the centre of a domain wall and $y = b$ equivalent to the pinning site at the edge of the wall, than b is equal to a quarter of the wall thickness

$$\begin{aligned}b &= \delta_0/4 \\ &= \frac{\pi}{4}\sqrt{2\alpha}\sqrt{M_s/H_a}\end{aligned} \tag{8.26}$$

Finally, the measure of pinning force, f, of a defect is to be estimated. The average energy per unit volume of the domain wall is proportional to γ/δ_0. Therefore, when a pinning defect with volume V is embedded inside a wall, the domain wall energy is reduced by an amount proportional to $V\gamma/\delta_0$. Since the interaction range between the pin and a wall is proportional to δ_0, the work done by the external force in unpinning the domain wall is of order of $f\delta_0$, which is equal to the energy lowered by the pinning site. We therefore have the relation

$$f = C\frac{\gamma}{\delta^2} \tag{8.27}$$

where C is a parameter to be fitted. This relation gives the temperature dependence of the maximum pinning force, which is similar to other detailed pinning models (Hilzinger, 1977b; Paul, 1977; Chen and Gaunt, 1990a; Chen and Gaunt, 1990b) Since the change of V with temperature is negligible comparing with the changes of γ and δ_0, Eqn. 8.27 is a valid approximation when the defect is not magnetic or the temperature dependence of its properties is correlated with those of the matrix. With all the relations of the factors with M_s and H_a founded, Eqn. 8.23 can be rewritten as

$$H_c = C_1 H_a (H_a/M_s)^{2\frac{2}{3}}(1 - C_2\sqrt{\frac{H_a}{M_s}\frac{kT}{M_s^2}}) \tag{8.28}$$

where C_1 and C_2 are constants that contain ρ, α and other numbers. So Eqn. 8.28 is a two parameter fit to H_c and the result is very satisfactory, as shown in Fig. 7.3. The good fit strongly suggests that only one pinning mechanism accounts for the coercivity over the whole temperature range. The thermal activation factor is found to be about 66.3% at 600 K, showing that thermal activation has reduced the coercivity by 1/3 at that temperature.

From the fitted C_2, the thickness and specific energy of the domain wall are calculated and are shown in Fig. 8.4. δ_0 drops monotonously from 151 Å at 140K to 45 Å at 600 K. The thin wall at high temperature is responsible for the decrease in M_s and increase in H_a. γ varies between 8.9 and 16.4 erg/cm^2 with a maximum value at 370 K. At 300 K, $\gamma = 15.7$ erg/cm^2, consistent with the value of 15 ± 1 erg/cm^2 reported by Málek (1958) and Dekker (1976).

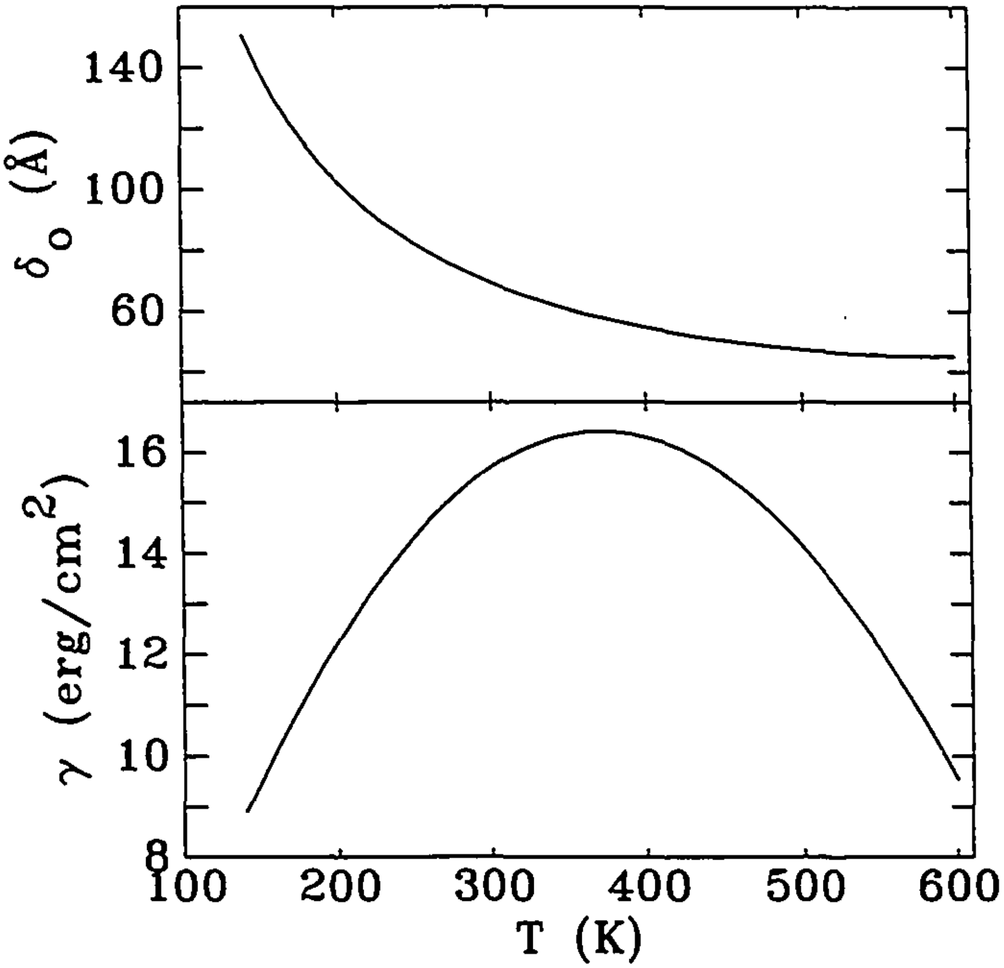

Figure 8.4: The domain wall energy $\gamma = 4\sqrt{AK}$ and the wall thickness $\delta_0 = \pi\sqrt{A/K}$ fitted by the hybrid pinning model using experiment values for M_s and H_a.

Chapter 9

Conclusion

Different phases of MnBi have been obtained by rapid solidification followed by controlled heat treatments. Quenched from the melt to room temperature, MnBi can be made into the amorphous state, despite the lack of a deep eutectic point in the Mn-Bi phase diagram. The depressed phase transformations during rapid solidification may play an important role in the glass formation of MnBi.

At 440 K, the amorphous MnBi crystallizes into a multi-phase state that contains principally Bi, Mn_3Bi, and NP. The crystallization is a diffusion controlled nucleation and growth process with an activation energy of 1.7 ev, and an Avrami exponent between 1.5 and 2.5, releasing an enthalpy of about 5.7 kJ/mol. The crystallized phases show no ferromagnetic or ferrimagnetic order down to 100 K.

At 540 K, the crystallized phases react to form a single phase LTP, with only about $5^{wt}\%$ of unreacted pure Bi. The unbalanced Mn atoms form a small amount of HC phase. The HC phase exhibits a critical field that is 6.7 T at 81 K, and rises to a maximum of 8 T at 120 K, then drops to 5.4 T at 193 K. The LTP is ferromagnetic. Its saturation magnetization at 0 K, extrapolated from the data measured between 82 and 589 K, is 742 kA/m, equivalent to 3.9 μ_B per Mn atom. Its anisotropy field is 1.5 T at 147 K, reaches a maximum value of 9.1 T at 560 K, then drops to 8.7 T at 590 K. The coercivity is zero at 82 K and 1.9 T at 570 K, and its temperature dependence can be well described by a hybrid model of domain wall pinning. The fit to the hybrid model produces the thickness of the domain wall of 151 Å at 140 K that drops to 45 Å at 600 K, and produces the domain wall energy of 8.9 erg/cm^2 at 140 K that reaches maximum value of 16.4 erg/cm^2 at 370 K then drops to 9.5 at 600 K.

At 640 K, the LTP transforms to HTP. The HTP is also ferromagnetic, with a Curie point at 450 K. The LTP-HTP transformation involve two processes: composition transition that takes 10 seconds of time at 630 K, which absorbs 2.4 kJ/mol enthalpy; magneto-structure transition is governed, on the contrary, by temperature but not by time–it spans about 40 K of temperature region and has also 40 K of thermal hysteresis.

The most significant successes of the research are summarized below.

There are two instrumental accomplishments in this research:

- A high temperature x-ray furnace was constructed. It enabled structures to be characterized at different temperatures, and contribute in the present work to the study of phase transformations. The temperature inhomogeneity over the sample is smaller than ±2 K up to 900 K, and the control system stablizes the temperature within ±1 K below 544 K and ±3 K around 900 K.
- The pulsed magnet was upgraded. The rebuilt temperature control system and pick-up coil, together with the improved data acquisition system, enabled the 22 T pulsed field to be used for measuring hysteresis loops and anisotropy fields from 80 to 870 K. The most important accomplishment is the combination of pulsed field with SPD technique that measures the anisotropy field directly.

The most significant new experimental achievements in this research are:

- Bulk amorphous MnBi is prepared by melt-spinning for the first time. Suitable conditions such as the speed of the copper wheel, the nozzle diameter of the quartz crucible, and gas pressure of the Ar atmosphere were determined that produce amorphous MnBi of good quality. This is the first time bulk amorphous MnBi have been made, and the present work is based on this achievement.

- MnBi single phase is formed in bulk. The LTP of MnBi made by this methods contains only $\sim 5^{wt}\%$ Bi. One importance of the achievement is the discovery that the rapid solidification can be a new technique for alloying where segregation is the main problem. The melt-spinning is now not only the technique to produce amorphous and other metastable phases, but also an efficient way to produce a stable phase that is not easy to get by other means.
- It is discovered that the LTP-HTP transformation undergoes two separate transformation processes. The composition transition detected by DSC is not synchronistic with the magneto-structure transition detected by TGA. The composition transition lasts only 10 seconds regardless of the heating rate, while magneto-structure transition lasts 15 seconds at 200 K/min of heating rate and 2130 seconds at 1 K/min.
- The anisotropy field of the LTP of MnBi is directly measured for the first time using the SPD technique. The anisotropy field is about 6 T at room temperature and increases with temperature, reaching 9.1 T at 560 K.

This research also suggested two models to describe the experimental results:

- A mechanism for the glass formation of MnBi is suggested. Unlike most metallic glasses that are formed around a deep eutectic point, the MnBi has a liquidus higher than the average melting point of Mn and Bi. After thorough analysis and complementary experiments, a multi-process picture is suggested for the kinetics of forming amorphous MnBi: it is not the liquidus temperature, but the temperature of lowest phase transformation in the liquid-solid coexistent region, whose ratio to the glass temperature satisfies Davies' (1976) criteria for glass formation by quenching from the melt.
- The temperature dependence of the coercivity has been satisfactorily described by a hybrid model of domain wall pinning that account on the intrinsic properties M_s and H_a and the thermal activation.

The following research ideas are suggested for further studies. Neutron diffraction studies on amorphous MnBi may supply further information about the possible phase separation; to study the formation of the LTP under high pressure, that shifts the melting point of Bi, may give further understanding how the melting of Bi affects the reaction; to study the the LTP-HTP transformation under stress may determine the relationship between composition transition and magneto-structural transition. Systematic studies of impurity additions to MnBi in an effort to further enhance magneto-optic and hard magnetic properties should be carried out.

References

Adachi, K. 1961. *J. Phys. Soc. Japan*, **16**, 2187.

Adam, G. D. and Standley, K. J. 1953. *Proc. Phys. Soc. (London) A*, **66A**, 823.

Adams, E. 1953. *Rev. Mod. Phys.*, **25**, 306.

Albert, P. A. and Carr Jr., W. J. 1961. *J. Appl. Phys.*, **32**, 201S.

Allain, Y., de Gunzbourg, J., Krebs, J. P., and Miedan-Gros, A. 1968. *Sci. Inst.*, **39**, 1360.

Andresen, A. F., Engebretsen, J. E., and Refsnes, J. 1972. *Acta Chem. Scand.*, **26**, 175.

Andresen, A. F., Halg, W., Fischer, P., and Stoll, E. 1967. *Acta chem. Scand.*, **21**, 1543.

Asti, G. and Bolzoni, F. 1980. *J. Mag. Mag. Mat.*, **20**, 29.

Asti, G. and Bolzoni, F. 1985. *J. Appl. Phys.*, **58**, 1924.

Asti, G. and Rinaldi, S. 1972. *Phys. Rev. Lett*, **28**, 1584.

Asti, G. and Rinaldi, S. 1974. *J. Appl. Phys.*, **45**, 3600.

Avrami, M. 1939. *J. Chem. Phys.*, **7**, 1103.

Avrami, M. 1940. *J. Chem. Phys.*, **8**, 212.

Avrami, M. 1941. *J. Chem. Phys.*, **9**, 177.

Bean, C. P. and Rodbell, D. S. 1962. *Phys. Rev.*, **126**, 104.

Behrndt, K. H. 1970. *J. vac. sci. tech.*, **7**, 385.

Bloch, F. 1932. *Z. Physik*, **74**, 295.

Buschow, K. H. J. 1981. *J. Appl. Phys.*, **52**, 3319.

Cahn, R. W. 1991. In Cahn, R. W., Haasen, P., Krameri, E. J., and Zarzycki, J., editors, *Materials Sience and Technology*, volume 9, page 493. VCH Publishers Inc.

Callaway, J. 1976. *Quantum Theory of the Solid State.* Academic Press Inc.

Capellman, H. 1986. *Metallic Magnetism.* Springer-Verlag.

Chen, D. 1971. *J. Appl. Phys.*, **42**, 3625.

Chen, L. C. and Spaepen, F. 1991. *J. Appl. Phys.*, 69, 679.

Chen, T. 1974. *J. Appl. Phys.*, 45, 2358.

Chen, T. and Stutius, W. 1974. *IEEE Mag. Trans.*, 10, 581.

Chen, X. 1990. Ph.D thesis, University of Manitoba, Winnipeg.

Chen, X. and Gaunt, P. 1990a. *J. Appl. Phys.*, 67, 2540.

Chen, X. and Gaunt, P. 1990b. *J. Appl. Phys.*, 67, 4592.

Chen, X., Liao, L. X., Altounian, Z., Ryan, D. H., and Strõm-Olsen, J. O. 1992. *J. Mag. Mag. Mat.*, 109, 271.

Chikazumi, S. 1964. *Physics of Magnetism.* John Wiley & Sons Inc., New York • London • Sydney.

Chou, C. P. P. and Turnbull, D. 1975. *J. Non-Crys. Solid*, 17, 169.

Christian, J. W. 1965. *The Theory of Transformations in Metals and Alloys.* Pergamon Press Ltd.

Coehoorn, R. and de Groot, R. A. 1985. *J. Phys. F: Met. Phys.*, 15, 2135.

Davies, H. A. 1976. *Phy. Chem. Glass.*, 17, 159.

Dekker, P. 1976. *J. Magn. Magn. Mat.*, 2, 32.

Donnald, I. W. and Davies, H. A. 1978. *J. Non-Crys. Sol.*, 30, 77.

From, M. 1989. Ph.D Thesis, McGill University, Montreal.

Fujime, S. 1966. *J. Appl. phys.*, 5, 9.

Furst and Halla 1938. *Z. Phys. Chemie*, 40, 283.

Gaunt, P. 1976. *Phil. Mag.*, 34, 775.

Gaunt, P. 1983. *Phil. Mag. B*, 48, 261.

Gaunt, P. 1984. *Phil. Mag. B*, 50, L45.

Gaunt, P. and Mylvaganam, C. K. 1979. *Phil. Mag. B*, 39, 313.

Givord, D., Lu, Q., Rossignol, M. F., Tenaud, P., and Viadieu, T. 1990. *J. Mag. Mag. Mat.*, 83, 183.

Grossinger, R. 1982. *J. Phys. D: Appl. Phys.*, page 1545.

Grossinger, R., Krewenka, R., Kirchmayr, H. R., Naastepad, P., and Buschow, K. H. J. 1987. *J. Less-Common Met.*, **134**, L17.

Guillaud, C. 1943. Ph.D Thesis, University of Strasbourg, Strasbourg, France.

Guillaud, C. 1951a. *J. Phys. Rad*, **12**, 492.

Guillaud, C. 1951b. *J. Phys. Radium*, **12**, 143.

Guillaud, C. 1951c. *J. Phys. Rad*, **12**, 223.

Guinier, A. 1963. *X-Ray Diffraction.* W. H. Freeman and Company.

Hansen, M. 1958. *Consitution of Binary Alloys.* McGrw-Hill, New York.

Haudek, H. and Unger, W. K. 1971. *Phys. stat. sol. (a)*, **7**, 393.

Heikes, R. R. 1955. *Phys. Rev.*, **99**, 446.

Henderson, D. W. 1979. *J. Non-Crys. Solids.*, **30**, 301.

Hihara, T. and Koi, Y. 1970. *J. Phys. Soc. Japan*, **29**, 343.

Hilzinger, H. R. 1977a. *Phil. Mag.*, **36**, 225.

Hilzinger, H. R. 1977b. *Appl. Phys.*, **12**, 253.

Hilzinger, H. R. and Kronmüller, H. 1977. *Physica B&C*, **86**, 1365.

Honda, S., Konishi, S., and Kusuda, T. 1972. *Appl. Phys. Lett.*, **22**, 421.

Kissinger, H. E. 1957. *Anal. Chem.*, **29**, 1702.

Kittel, C. 1949. *Rev. Modern Phys.*, **21**, 541.

Köster, U. and Herold, U. 1981. In Güntherodt, H. J. and Beck, H., editors, *Glassy Metals I*, page 225. Springer-Verlag, Berlin.

Landau, L. D. and Lifshitz, E. M. 1980. *Statistical physics.* Pergamon Press Ltd.

Mao, M. and Altounian, Z. 1991. *Mater. Sci. Engin. A*, **149**, L5.

Massalski, T. B., Murry, J. L., Bennetti, L. H., and Baker, H. 1986. *Binary Alloy Phase Diagrams.* American Society for Metals.

Morrish, A. H. 1965. *The Physical Principles of Magnetism.* John Wiley & Sons Inc., New York • London • Sydney.

Málek, Z. and Kamberský, V. 1958. *Csech. J. Phys.*, **8**, 416.

Neufeldt, B. 1989. A pulsed magnet for high-field magnetization measurements. M.Sc. Thesis, McMill University, Montreal.

Noothoven Van Goor, J. M. and Zijlstra, H. 1968. *J. Appl. Phys.*, **39**, 5471.

Notis, M. R., Shah, D., Graham Jr., C. D., and Trout, S. R. 1978. *J. Appl. Phys.*, **49**, 2043.

Notis, M. R., Shah, D., Young, S., and Graham Jr., C. D. 1979. *IEEE Trans. Mag.*, **15**, 957.

Paul, D. I. 1977. *Phys. Lett.*, **64A**, 485.

Pearson, W. B. 1958. *A Handbook of Lattice Spacings and Structures of Metals and Alloys*. Pergamon Press.

Pirich, R. 1979. *IEEE Mag. Trans.*, **15**, 1154.

Pirich, R. G. 1980. *IEEE Mag. Trans.*, **MAG-16**, 1065.

Richter, H. 1969. *J. Vac. Sci. Tech.*, **6**, 855.

Roberts, B. W. 1956. *Phys. Rev.*, **104**, 607.

Roberts, B. W. and Bean, C. P. 1954. *Phys. Rev.*, **96**, 1494.

Seybolt, A. U., Hansen, H., Roberts, B. W., and Yurcisin, P. 1956. *J. Metals*, page 606.

Sher, Y. S., Shtol'ts, E. V., and Margolina, V. I. 1960. *Soviet Phys. JETP*, **11**, 33.

Siebe, P. 1919. *Z. Anorg. Chem.*, **108**, 161.

Stoner, E. C., S., F. R., and Wohlfarth, E. P. 1948. *Phil. Trans. Roy. Soc. A*, **240**, 599.

Stutius, W., Chen, T., and Sandin, T. R. 1973. Magnetic properties of MnBi single crystals. In *19th Conf. on Magnetism and Magnetic Materials*, page 1222, Boston. AIP Conf. Proc.

Stutius, W., White, R. M., Chen, T., and Stewart, G. R. 1975. *AIP Conf. Proc.*, **24**, 227.

Takagi, M. 1956. *J. Phys. Soci. Japan*, **11**, 396.

Takayama, S. 1976. *J. Mat. Sci*, **11**, 164.

Ueno, S. and waseda, Y. 1968. In *Rapidly solidified materials*, page 153, San Diego, Ca. USA. Proc. Intern. Conf.

Warren, B. E. 1969. *x-ray Diffraction.* Addison-Wesley Inc.

Waseda, Y. 1977. In Evans, R. and Greenwood, D. A., editors, *Liquid Metals*, page 230, Bristol and London. Third International Conference on Liquid Metals, Bristol 1976, Institute of Physics.

Wasedai, Y. and Tamaki, S. 1975. *Philo. Mag.*, page 273.

Weiss, P. 1906. *Compt. Rend.*, **143**, 1136.

Weiss, P. 1907. *J. Phys.*, **6**, 661.

Williams, H., Sherwood, R. C., Foster, F. G., and Kelley, E. M. 1957. *J. Appl. Phys.*, **28**, 1181.

Xu, G. S., Lakshmi, C. S., and Smith, R. W. 1989. *J. Mater. Sci. Lett.*, **8**, 1113.

Yoshida, K., Yamada, T., and Furukawa, Y. 1968. *Acta Metall.*, **34**, 969.

Zijlstra, H. 1967. *Experimental Methods in Magnetism.* North-Holland Publishing Company, Amsterdam.